

# Surface Acoustic Waves in Strain-Engineered Thin (K,Na) $\text{NbO}_3$ Films: From Basic Research to Application in Molecular Sensing

Sijia Liang

Schlüsseltechnologien / Key Technologies

Band / Volume 245

ISBN 978-3-95806-571-0





Forschungszentrum Jülich GmbH  
Institute of Biological Information Processing  
Bioelectronics (IBI-3)

# **Surface Acoustic Waves in Strain-Engineered Thin (K,Na)NbO<sub>3</sub> Films: From Basic Research to Application in Molecular Sensing**

Sijia Liang

Schriften des Forschungszentrums Jülich  
Reihe Schlüsseltechnologien / Key Technologies

Band / Volume 245

---

ISSN 1866-1807

ISBN 978-3-95806-571-0

Bibliografische Information der Deutschen Nationalbibliothek.  
Die Deutsche Nationalbibliothek verzeichnet diese Publikation in der  
Deutschen Nationalbibliografie; detaillierte Bibliografische Daten  
sind im Internet über <http://dnb.d-nb.de> abrufbar.

Herausgeber  
und Vertrieb:           Forschungszentrum Jülich GmbH  
                                  Zentralbibliothek, Verlag  
                                  52425 Jülich  
                                  Tel.: +49 2461 61-5368  
                                  Fax: +49 2461 61-6103  
                                  zb-publikation@fz-juelich.de  
                                  www.fz-juelich.de/zb

Umschlaggestaltung: Grafische Medien, Forschungszentrum Jülich GmbH

Druck:                    Grafische Medien, Forschungszentrum Jülich GmbH

Copyright:             Forschungszentrum Jülich 2021

Schriften des Forschungszentrums Jülich  
Reihe Schlüsseltechnologien / Key Technologies, Band / Volume 245

ISSN 1866-1807  
ISBN 978-3-95806-571-0

Vollständig frei verfügbar über das Publikationsportal des Forschungszentrums Jülich (JuSER)  
unter [www.fz-juelich.de/zb/openaccess](http://www.fz-juelich.de/zb/openaccess).



This is an Open Access publication distributed under the terms of the [Creative Commons Attribution License 4.0](https://creativecommons.org/licenses/by/4.0/),  
which permits unrestricted use, distribution, and reproduction in any medium, provided the original work is properly cited.

## Zusammenfassung

In dieser Arbeit zeigen wir, dass in Dünnschichtsystemen die Energie der akustischen Oberflächenwellen (SAW) im Vergleich zu kompakten Bulksystemen wesentlich stärker auf der Oberfläche konzentriert ist, wodurch diese Systeme äußerst empfindlich auf Störungen an der Oberfläche reagieren. Auf dieser Basis haben wir ein Dünnschicht-SAW-Sensorsystem mit extrem hoher Empfindlichkeit für Massenbelegung entwickelt. Aufgrund seiner hervorragenden piezoelektrischen Eigenschaften wurde  $K_xNa_{1-x}NbO_3$  (KNN) als Kandidat für das Dünnschichtsystem ausgewählt. Unter Verwendung epitaktischer Verspannung wurden die piezoelektrischen Eigenschaften angepasst, um das SAW-Signal und die Empfindlichkeit der Schicht zu verbessern. Abschließend wurde ein SAW-Sensor auf der Basis extrem dünner ( $\sim 30$  nm) KNN Filme entwickelt, mit dem die Abscheidung von Monolagen organischer Moleküle erfasst werden konnte.

Für die Abscheidung von epitaktischen KNN-Filmen wurden zwei Methoden verwendet - metallorganische chemische Gasphasenabscheidung (MOCVD) und gepulste Laserabscheidung (PLD). Eine Reihe unterschiedlicher Scandate ( $DyScO_3$  (DSO),  $TbScO_3$  (TSO),  $GdScO_3$  (GSO) und  $SmScO_3$  (SSO)) wurden als Substrate mit unterschiedlichen Gitterfehlpassungen in Bezug auf die KNN-Filme und daher unterschiedlichen Niveaus der Verspannung ausgewählt. Gemäß Röntgenanalyse (ins. reziproke Raumkartierung (RSM)) zeigen die MOCVD-präparierten KNN-Proben ein perfektes epitaktisches Wachstum, während die PLD-präparierten Proben zwar epitaktisch sind, aber eine beginnende plastische Relaxation zeigen. Als Folge dessen zeigen die MOCVD-Proben das typische konventionelle ferroelektrische Verhalten ohne merkliche Frequenzdispersion des ferroelektrischen Phasenübergangs, während die PLD-Proben ein lehrbuchartiges Relaxorverhalten mit einem frequenzdispersiven ferroelektrischen Phasenübergang zeigen. Es scheint, dass die höhere Teilchenenergie der PLD zu Inhomogenitäten der mikroskopischen Zusammensetzung führt, die die Bildung polarer Nanoregionen (PNR) nach sich zieht.

Aufgrund der kompressiven Verspannung werden die Phasenübergangstemperaturen der MOCVD- und PLD-Proben von  $T_C \approx 693$  K für unverspanntes KNN zu niedrigeren Temperaturen verschoben. Zunächst wird ein „quadratisches Modell“ angewendet, um die Dehnungsabhängigkeit der Phasenübergangstemperatur zu analysieren. Die Phasenübergangstemperaturen von MOCVD-Proben zeigen eine perfekte lineare Abhängigkeit von der Druckspannung, während die PLD-Proben keine klare Abhängigkeit zeigen. Um das Modell zu verbessern, wird ein „vertikales Gittermodell“ (VLM) vorgeschlagen, das auf dem Poisson-Effekt basiert. Im neuen Modell wird die Dehnung der Filme durch den vertikalen Gitterparameter des KNN-Films dargestellt. Die Phasenübergangstemperaturen von MOCVD- und PLD-Proben zeigen nun eine perfekte lineare Abhängigkeit vom vertikalen Gitterparameter mit leicht unterschiedlichen Steigungen für MOCVD und PLD. Dies bestätigt

das neue VLM Modells zur Beschreibung der Spannungsabhängigkeit der Phasenübergangstemperatur.

Die dielektrischen Eigenschaften der verspannten KNN-Filmen sind stark verbessert. Z.B. ergibt sich eine maximale Permittivität von  $\epsilon'_{max} \approx 13695$  bei  $\sim 330$  K und eine Raumtemperatur (RT) Permittivität von  $\epsilon'_{RT} \approx 5166$  für einen 27 nm dicken  $K_{0.7}Na_{0.3}NbO_3$ -Film auf TSO, hergestellt durch MOCVD, im Vergleich zu  $\epsilon'_{max} \approx 6400$  und  $\epsilon'_{RT} \approx 600$  für unverspanntes KNN. Weiterhin sind die dielektrischen Eigenschaften anisotrop, z.B. ist das Verhältnis der RT-Permittivität  $\epsilon'_{[1\bar{1}0]}/\epsilon'_{[001]} = 1.33$ .

Im nächsten Schritt wurden die SAW-Eigenschaften von MOCVD- und PLD-Proben untersucht. Die MOCVD-Proben zeigen starke SAW-Signale bei RT ( $\Delta S_{21}$  bis  $\sim 4$  dB), was sogar mit Bulk-SAW-Kandidaten vergleichbar ist. Darüber hinaus können höhere Harmonische (lediglich ungerader Ordnung) erzeugt werden. Die 3. Harmonische zeigt die größte Intensität. Im Gegensatz dazu sind die SAW in PLD-Proben kaum sichtbar. Diese Situation ändert sich jedoch erheblich mit dem Anlegen einer Gleichstromvorspannung. Die SAW-Intensität steigt von  $\sim 0,2$  dB für eine Vorspannung von Null auf  $\sim 4$  dB für eine Gleichstromvorspannung von 40 V/mm. Die DC-Vorspannung ermöglicht so eine neuartige elektronische Abstimmung des SAW-Signals. Dies neuartige Verhalten lässt sich durch das Verhalten der PNRs der PLD-Proben erklären.

Schließlich wurde ein Gasphasen-SAW-Sensor auf der Basis der verspannten KNN-Dünnschichten entwickelt. Der SAW-Sensor wurde erfolgreich zur in-situ Überwachung der molekularen Schichtabscheidung (MLD) eingesetzt. Eine extrem hohe Empfindlichkeit des Sensors konnte in diesen Experimenten nachgewiesen werden, sogar noch mit der Ordnung der SAW-Harmonischen zunimmt. Eine Empfindlichkeit von  $S_i \approx -22,3$  bis  $-116,7$  kHz/nm konnte abgeschätzt werden, was im Vergleich zur Empfindlichkeit von konventionellen Bulk-SAW-Sensoren eine um mindestens eine Größenordnung höhere Empfindlichkeit darstellt.

Unsere Arbeit demonstrieren die Möglichkeit, die Empfindlichkeit von SAW-Systemen durch Verwendung extrem dünner, verspannte und piezoelektrischer Schichten enorm zu verbessern. Die extrem hohe Empfindlichkeit, die in unserem Dünnschicht-SAW-System gezeigt wurde, impliziert potenzielle Anwendungen, die von der In-situ-Detektion der Monoschichtablagerung bis zur hochselektiven und sensitiven Erkennung biologischer Marker für die Krankheitsdiagnostik (z.B. POCT) reichen.

## Abstract

In this work we demonstrate that in thin film systems, the energy of surface acoustic waves (SAW) is more concentrated on the surface compared to bulk system, which makes this system extremely sensitive to any perturbation on the surface. On this basis we developed a thin film SAW system with extremely high sensitivity to any mass loading. Due to its outstanding piezoelectric properties,  $K_xNa_{1-x}NbO_3$  (KNN) was chosen as a candidate for the thin film system. Using epitaxial strain the piezoelectric properties were tailored in order to improve the SAW signal and sensitivity. Finally, a thin ( $\sim 30$  nm) film KNN based SAW sensor was developed which allows to detect monolayer deposition of organic molecules.

For the deposition of epitaxial KNN films, two methods—metal organic chemical vapor deposition (MOCVD) and pulsed laser deposition (PLD)—were used. A series of scandates,  $DyScO_3$  (DSO),  $TbScO_3$  (TSO),  $GdScO_3$  (GSO), and  $SmScO_3$  (SSO), were chosen as substrates with different lattice mismatch with respect to the KNN films and therefore different levels of compressive strain. According to X-ray analysis (reciprocal space mapping (RSM)), the MOCVD-prepared KNN samples show perfect epitaxial growth, whereas the PLD-prepared samples are epitaxy but show an onset of plastic relaxation. The MOCVD samples exhibit a typical conventional ferroelectric behavior with hardly any frequency dispersion of the ferroelectric phase transition. In contrast, the PLD samples show textbook-like relaxor behavior with a frequency dispersive ferroelectric phase transition. It seems that the higher particle energy of PLD leads to microscopic composition inhomogeneities which results in the formation of polar nanoregions (PNR).

Due to the compressive strain, the phase transition temperatures of MOCVD and PLD samples are shifted from  $T_C \approx 693$  K for unstrained KNN to lower temperatures. A “square model” is first applied to analyze the strain dependence of the phase transition temperature. The phase transition temperatures of MOCVD samples show a perfect linear dependence on compressive strain, whereas the PLD samples show no clear dependence. In order to improve the model, a “normal lattice model” (NLM) is proposed which is based on the Poisson effect. In the new model, the strain of the film is represented by the vertical lattice parameter of the KNN film. The phase transition temperatures of both MOCVD and PLD samples show a perfect linearity with slightly different slopes as function of vertical lattice parameter. This supports the use of the new model for the description of the strain dependence of the phase transition temperature.

The dielectric properties of strained KNN films are highly improved, e.g. a maximum permittivity of  $\epsilon'_{max} \approx 13695$  at  $\sim 330$  K and a room temperature (RT) permittivity of  $\epsilon'_{RT} \approx 5166$  are achieved for a 27 nm-thick  $K_{0.7}Na_{0.3}NbO_3$  film on TSO prepared by MOCVD compared to  $\epsilon'_{max} \approx 6400$  and  $\epsilon'_{RT} \approx 600$  for unstrained KNN. Furthermore, the dielectric properties are

anisotropic, e.g. the ratio of the permittivity measured along  $[1\bar{1}0]_{\text{TSO}}$  and  $[001]_{\text{TSO}}$  directions is  $\varepsilon'_{[1\bar{1}0]}/\varepsilon'_{[001]} = 1.33$  for the MOCVD film on TSO.

In the next step, the SAW properties of MOCVD and PLD samples were investigated. The MOCVD samples show strong SAW signals at RT ( $\Delta S_{2f}$  up to  $\sim 4$  dB) which is even comparable to bulk SAW candidates. Moreover, high orders of odd harmonics can be generated and the 3<sup>rd</sup> harmonic shows the largest intensity. In contrast, the SAW in PLD samples are hardly visible. However, this situation changes significantly with the application of a DC bias. The SAW intensity increases from  $\sim 0.2$  dB for zero bias to  $\sim 4$  dB for a DC bias of 40 V/mm. The DC bias allows an electronic tuning of the SAW signal. This explained by the relaxor-type behavior based on the PNRs of the PLD samples.

Finally, a gas-phase SAW sensor is developed based on KNN thin films. The SAW sensor has been successfully applied to in situ monitoring of molecular layer deposition (MLD). An extremely high sensitivity of the sensor has been demonstrated. This sensitivity even increases with the order of the SAW harmonic. A sensitivity of  $S_i \approx - 22.3$  to  $- 116.7$  KHz/nm is demonstrated. Compared to the sensitivity of SAW sensors based on bulk systems, the thin film SAW sensor system exhibits at least one order of magnitude higher sensitivity.

Our work provides a way of improving the sensitivity of SAW systems via applying thin films. The extremely high sensitivity demonstrated in our thin film SAW system implies potential applications ranging from in situ detection of monolayer deposition to highly selective and sensitive sensing of biological markers for disease diagnosis (e.g. point-of-care-testing (POCT)).

# Contents

Zusammenfassung .....	I
Abstract .....	III
1 Introduction .....	1
2 Theoretical background .....	4
2.1 Fundamentals of ferroelectrics .....	4
2.1.1 Dielectricity .....	5
2.1.2 Ferroelectricity .....	8
2.1.3 Ferroelectric phase transition .....	10
2.1.4 Piezoelectricity .....	11
2.2 Engineering of ferroelectricity .....	12
2.2.1 Doping .....	12
2.2.2 Strain .....	14
2.2.3 Relaxor .....	16
2.3 Surface acoustic waves .....	19
2.3.1 Surface acoustic wave modes .....	19
2.3.2 Generation and detection of surface acoustic waves .....	21
2.3.3 Surface acoustic waves sensors .....	25
2.4 Introduction to $K_xNa_{1-x}NbO_3$ .....	28
3 Sample preparation and experimental techniques .....	30
3.1 Sample preparation .....	30
3.1.1 Metal organic chemical vapor deposition .....	30
3.1.2 Pulsed laser deposition .....	31
3.1.3 Evaporation deposition .....	32
3.1.4 Molecular layer deposition .....	32
3.2 Film characterization .....	33
3.2.1 High resolution X-ray diffraction .....	34
3.2.2 Reciprocal space mapping .....	35
3.2.3 Atomic force microscopy .....	37
3.2.4 Time-of-flight secondary ion mass spectroscopy .....	38
3.3 Electrodes fabrication .....	40
3.4 Electronic characterization .....	42
3.4.1 Temperature control .....	43
3.4.2 Permittivity measurement .....	44
3.4.3 Surface acoustic wave measurement .....	46
3.4.4 Surface acoustic wave sensor .....	47
4 Strain engineering of the ferroelectric properties of $K_xNa_{1-x}NbO_3$ films .....	51
4.1 Structure, strain, and stoichiometry .....	51

4.2 Strain engineering of $T_C$ .....	56
4.3 Strained conventional and relaxor-type ferroelectrics .....	62
4.4 Summary .....	66
5 SAW properties in conventional ferroelectric (K,Na)NbO <sub>3</sub> .....	67
5.1 SAW properties at room temperature .....	67
5.2 Impact of strain on SAW properties.....	75
5.3 Temperature dependence of permittivity and SAW signal .....	78
5.4 Summary .....	81
6 Tunable SAW properties of relaxor-type ferroelectric (K,Na)NbO <sub>3</sub> .....	83
6.1 SAW properties without dc bias .....	83
6.2 DC bias tuning of the SAW.....	88
6.3 PNR-model for DC bias tuning .....	92
6.4 Summary .....	96
7 KNN thin film gas-phase SAW sensor .....	97
7.1 MLD sensor system .....	97
7.2 SAW sensor operation at elevated MLD temperature.....	106
7.3 Summary .....	110
8 Conclusion .....	111
References .....	114
Appendix .....	121
Sample list .....	121
E-beam lithography and lift-off recipe .....	123
Acknowledgement.....	125

## 1 Introduction

Due to their outstanding properties, surface acoustic wave (SAW) based devices are presently widely used in communications, signal processing, and transducer, actuator, and sensor techniques [1-6]. For example, the most common applications of SAWs are probably special filters in our smart phones, which make our daily life so comfortable. Maybe even more important are sensor applications which allow extremely sensitive detection of change in temperature, pressure, mechanical force and especially mass loading [7-10]. The latter is for example of interest for medical applications like the detection of bacteria or viruses. However, for the detection of many interesting biomarkers or pathogens even the sensitivity of existing SAW sensors is not good enough. The aim of this work is therefore to explore new way to improve the sensitivity of SAW sensor systems.

The working principle of SAW mass detector is based on the impact of the mass loading on the properties of the acoustic wave travelling at surface of the sensor. Since the SAW amplitude attenuates exponentially with depth into the material [11], the acoustic energy is concentrated at the surface and therefore sensitive to mechanical, chemical, optical or electrical perturbations of the surface.

First, one way to boost the sensitivity of a SAW sensor could be to confine the energy of the acoustic wave even more to the surface. Therefore, we decided to develop SAW sensor systems based on extremely thin piezoelectric films. Due to the thinness of these films, the acoustic energy of the propagating SAWs can be further concentrated on the surface, resulting in a highly increased energy density. Consequently, the SAWs generated in the thin films are more sensitive to surface perturbations and therefore possess an improved sensitivity.

Second, since most of the sensor systems are operated at or around room temperature (RT), materials with perfect piezoelectric properties around RT are required. The piezoelectric and thus SAW response is usually largest close to the phase transition temperature, which unfortunately is typically far away from RT. It means the material properties need to be tailored to meet the requirement of developing thin film SAW systems.

For this purpose we employ a strain engineering based on epitaxial growth to tailor the structure and resulting properties (e.g. piezoelectricity, ferroelectricity) of the thin films. This way we can either shift the phase transition temperature to a higher or lower temperature by applying an adequate tensile or compressive strain, respectively [12,13].

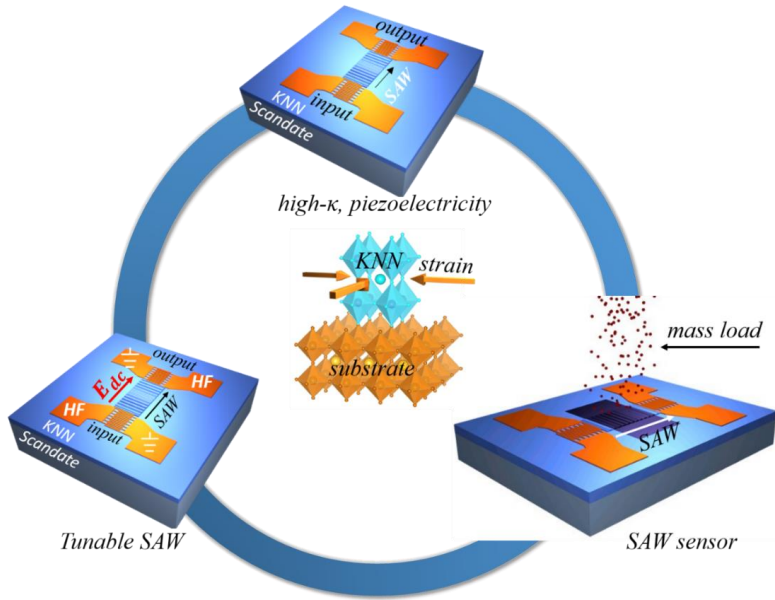


Figure 1.1. Schematics illustrate the basic ideas and main achievements of this work. SAW devices, tunable SAW devices, and SAW gas-phase sensors based on epitaxially strained KNN films are developed and demonstrated.

Thirdly, with  $K_xNa_{1-x}NbO_3$  (KNN) we found a promising lead-free thin film candidate with already excellent piezoelectric properties in unstrained bulk form [14]. With strain these properties (e.g. phase transition temperature) can be tailored (e.g. the phase transition can be shifted towards RT). Consequently, improved SAW performance might be expected in the strained thin films.

Finally, we aimed to merge these components and develop a demonstrator, i.e. a SAW sensor systems based on epitaxially strained KNN thin films with extremely high sensitivity (see Fig. 1.1).

As a result, we try to discuss the following questions in this thesis:

- (i) Can we achieve a better confinement of the Saw energy at the surface of the SAW device?
- (ii) Can we tailor the properties of the KNN thin films via epitaxial strain to achieve large SAW signal at RT?
- (iii) And how is the sensitivity of a resulting thin film SAW sensor affected by these methods?

To answer these questions, this thesis is structured as follows:

In chapter 2 the theoretical background and state of research is sketched. First, the fundamentals of ferroelectricity, including dielectric polarization, permittivity, ferroelectricity and piezoelectricity, are introduced. Subsequently, strategies for the engineering of

ferroelectricity, including doping, strain and relaxor-type ferroelectricity, are discussed. Then the fundamentals of surface acoustic waves, including their generation, detection, and applications, are introduced. Finally, the lead-free piezoelectric candidate (K,Na)NbO<sub>3</sub>, which represent the basic of this work, is introduced.

In [chapter 3](#) the sample preparation and characterization methods are described. First, the epitaxial growth techniques (MOCVD, PLD) are introduced and compared. Then the characterization methods are introduced comprising of HRXRD, RSM, AFM, and ToF-SIMS. Lithography, metallization, and lift-off techniques for the fabrication of micro electrodes are introduced. Finally, the permittivity and surface acoustic wave measurements as well as the surface acoustic wave sensor experiments are introduced and their working mechanisms are illustrated.

In [chapter 4](#) the properties of the epitaxially grown KNN films on various scandate substrates are compared. First, the structural characterization of MOCVD and PLD samples is presented. Then the impact of strain on the phase transition temperature of the thin films is investigated. Different models for the explanation of the shift of the phase transition with the strain are discussed. Then the structural and ferroelectric properties of MOCVD and PLD samples are compared demonstrating conventional (MOCVD) or relaxor-type (PLD) behavior. Finally, promising candidates for SAW sensor applications are selected.

In [chapter 5](#) the SAW properties of the MOCVD samples with conventional ferroelectric behavior are discussed. First, the frequency response of the SAW structures at RT is presented. Then the generation of SAW harmonics, the harmonic order dependence of SAW intensity and velocity are discussed. Then the anisotropy and impact of strain on SAW properties are investigated. Finally, the temperature dependence of SAW properties are studied.

In [chapter 6](#) the SAW properties of the PLD-prepared KNN samples with relaxor-type behavior are discussed. First, the relaxor-type ferroelectric properties of the PLD samples are explicitly characterized. Then we demonstrate that the SAW properties of the relaxor-type ferroelectrics can be tuned by a DC bias. A polar nanoregions (PNR) based model is proposed to explain the novel SAW behavior of these films, the tunable SAW signal.

In [chapter 7](#) we describe a first test of thin strained KNN films in a SAW sensor application. For this purpose we developed a setup consisting of carrier on a vacuum flanch, which allows to monitor organic molecules in the gas phase. This setup was tested in a deposition device designed for the gas phase deposition of organic molecular monolayers. After a brief description of the deposition setup, design, working mechanism and sensitivity of the SAW gas phase sensor are discussed in this chapter.

In [chapter 8](#) the results achieved in this thesis are summarized and an outlook for the further applications based on strained KNN film systems are presented.

## 2 Theoretical background

In this chapter the fundamentals of ferroelectricity, including dielectric polarization, permittivity, ferroelectricity and piezoelectricity, are introduced (chapter 2.1). Subsequently, strategies for the engineering of ferroelectricity, including doping, strain and relaxor-type ferroelectricity, are discussed (chapter 2.2). Then the fundamentals of surface acoustic waves, including their generation, detection, and applications, are described (chapter 2.3). Finally, the lead-free piezoelectric candidate (K,Na)NbO<sub>3</sub>, which represent the basic of this work, is introduced (chapter 2.4).

### 2.1 Fundamentals of ferroelectrics

In 1920, the ferroelectric effect was discovered by J. Valasek in potassium sodium tartrate tetrahydrate (NaKC<sub>4</sub>H<sub>4</sub>O<sub>6</sub>•4H<sub>2</sub>O)—known as “Rochelle salt” [15]. Ferroelectrics show similar hysteresis behavior as known from ferromagnetics, hence the name. Since then, the research of ferroelectrics has developed for the last 100 years. Nowadays, ferroelectric materials are widely used in various fields ranging from tunable ferroelectric capacitors, piezo-sensors, actuators and microelectromechanical systems (MEMS) [16-19] to ferroelectric random-access memory (FeRAM), multiferroics, ferroelectric tunnel junctions (FTJ), and energy harvesters [20-23], as shown in Fig. 2.1.

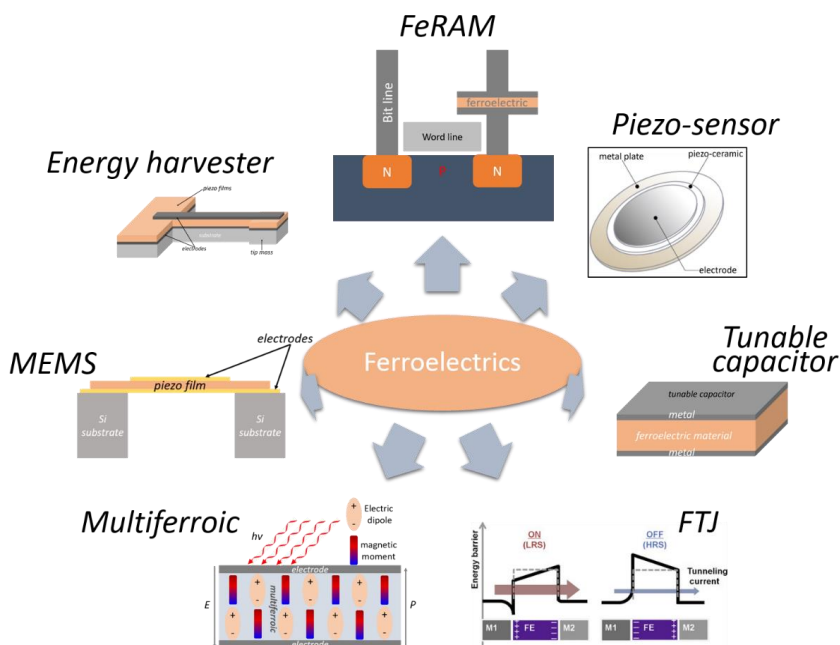


Figure 2.1: Various applications of ferroelectrics. Ranging from tunable ferroelectric capacitors, piezo-sensors, and microelectromechanical systems (MEMS) to multiferroics, energy harvesters, ferroelectric tunnel junctions (FTJ) and ferroelectric random-access memory (FeRAM). (Ideas for sketches adapted from ref. [16-23])

### 2.1.1 Dielectricity

Ferroelectric material represents a special type of dielectric material. A key feature of dielectrics is their ability to transmit the electric fields via induction, rather than conduction. Dielectrics will be electrically polarized if exposed to the electric field. If the applied exterior electric field is not very strong, the polarization  $P$  is considered to have a linear relationship with external electric field  $E$ :

$$P = \epsilon_0 \chi_e E = \epsilon_0 (\epsilon' - 1) E \quad (2.1)$$

where  $\epsilon_0$  is the permittivity of free space,  $\chi_e$  is the electric susceptibility,  $\epsilon'$  is the relative dielectric constant, which is the real component of the dielectric constant  $\epsilon$ :

$$\epsilon = \epsilon' + i\epsilon'' \quad (2.2)$$

where  $\epsilon''$  is the imaginary component of the dielectric constant, indicating the energy loss in the dielectrics. The loss tangent is then defined by:

$$\tan \delta = \frac{\epsilon''}{\epsilon'} \quad (2.3)$$

In general, there are four different mechanisms of polarization, i.e. electronic polarization, ionic polarization, polar orientational polarization, and space charge polarization (see Fig. 2.2).

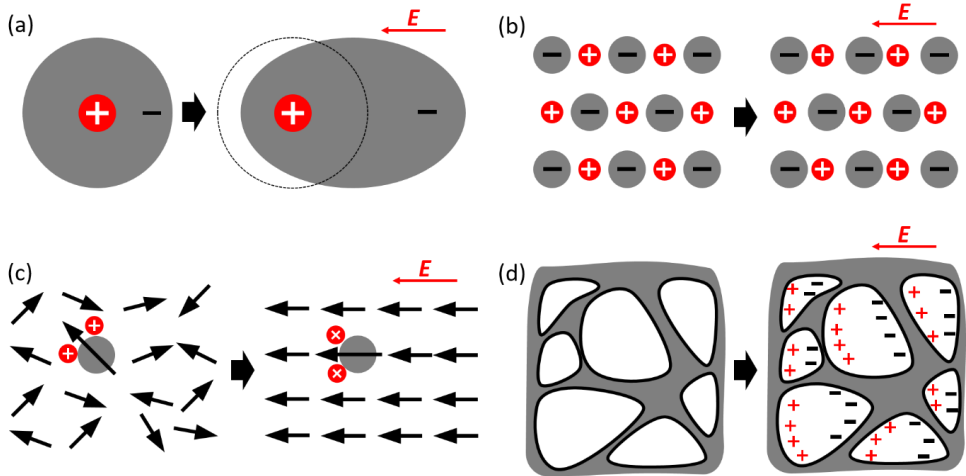


Figure 2.2. Schematics illustrate four types of polarization mechanisms: (a) electronic polarization, (b) ionic polarization, (c) polar orientational polarization, and (d) space charge polarization.

**Electronic polarization:** The ions (atoms) that form the dielectrics consist of positively charged nuclei and negatively charged electrons. In the absence of an electric field, the positively and negatively charged centers coincide. However, in the presence of an exterior electric field,

the negatively charged electron cloud will be shifted with respect to the positively charged nucleus, forming an electric dipole and resulting in an electronic polarization (see Fig. 2.2(a)). The resulting dipole has an electric dipole moment:

$$\mu = q \cdot r \quad (2.4)$$

where  $q$  is the charge and  $r$  is the relative displacement vector between the centers of positive and negative charges. In case of linear polarization, the induced dipole moment is proportional to the electric field intensity:

$$\mu = \alpha_e E_{loc} \quad (2.5)$$

where  $\alpha_e$  is the electronic polarizability and  $E_{loc}$  is the local electric field at the dipole, which can differ from the external electric field  $E$ . The electronic polarizability  $\alpha_e$  is given by:

$$\alpha_e = 4\pi\epsilon_0 R^3 \quad (2.6)$$

where  $R$  is the atomic radius. Since  $R$  is of order of  $10^{-10}$  m,  $\alpha_e$  is of the order of  $10^{-40}$  F·m<sup>2</sup>.

*Ionic polarization:* In analogy, a relative displacement of positive and negative ions occurs in ionic crystals upon expose to an electric (see Fig. 2.2(b)). The resulting ionic polarizability  $\alpha_i$  is given by:

$$\alpha_i = \frac{12\pi\epsilon_0 a^3}{A(n-1)} \quad (2.7)$$

where  $a$  is the unit cell constant,  $A$  is the Madelung constant,  $n$  is the electronic repulsion index (in case of ionic crystal,  $n = 7$  to  $11$ ). The ionic polarizability has a comparable order with electronic polarizability.

*Orientalional polarization:* Polar dielectrics, e.g. water, are composed of polar molecules. Polar molecules possess permanent electric dipole moments  $\mu_0$  due to the net separation of positive and negative charges. Because of thermal motion, these dipoles are disorderly aligned, resulting in a zero macroscopic polarization. However, in the presence of  $E$ , the dipoles will be orientated. Since the dipoles have the lowest potential energy when aligned along the direction of electric field, they tend to align along the electric field direction. As a result, a macroscopic polarization is yielded and a polar orientational polarization occurs (see Fig. 2.2(c)). The polar orientational polarizability  $\alpha_d$  is given by:

$$\alpha_d = \frac{\mu_0^2}{3kT} \quad (2.8)$$

where  $k$  is the Boltzmann constant. Normally, the polar orientational polarizability is much larger than the electronic polarizability (it is of the order of  $10^{-38}$  F·m<sup>2</sup>).

*Space charge polarization:* the space charge polarization is attributed to the existence of inhomogeneity and interfaces, e.g. grain boundary and phase boundary, in the dielectrics. Under an applied electric field, the chaotically distributed free charges will move and

accumulate at these defective spaces, leading to the space charge polarization (see Fig. 2.2(d)).

The different types of polarization can be distinguished by their frequency dependence. Generally, the formation of the electronic and ionic polarization takes only  $10^{-16}$  -  $10^{-14}$  s and  $10^{-13}$  -  $10^{-12}$  s, respectively. Consequently, under an applied ac field, the electronic polarization is able to occur even in the optical frequency regime, while the ionic polarization exists only for frequency lower than  $10^{13}$  Hz (corresponding to infrared frequency). In comparison, the formation of polar orientational and space charge polarization takes even longer times— $10^{-10}$  -  $10^{-2}$  s and  $10^0$  -  $10^3$  s, respectively. As a result, they only contribute in a relatively low frequency regime. The relationship between dielectric polarization mechanism and frequency is schematically shown in Fig. 2.3.

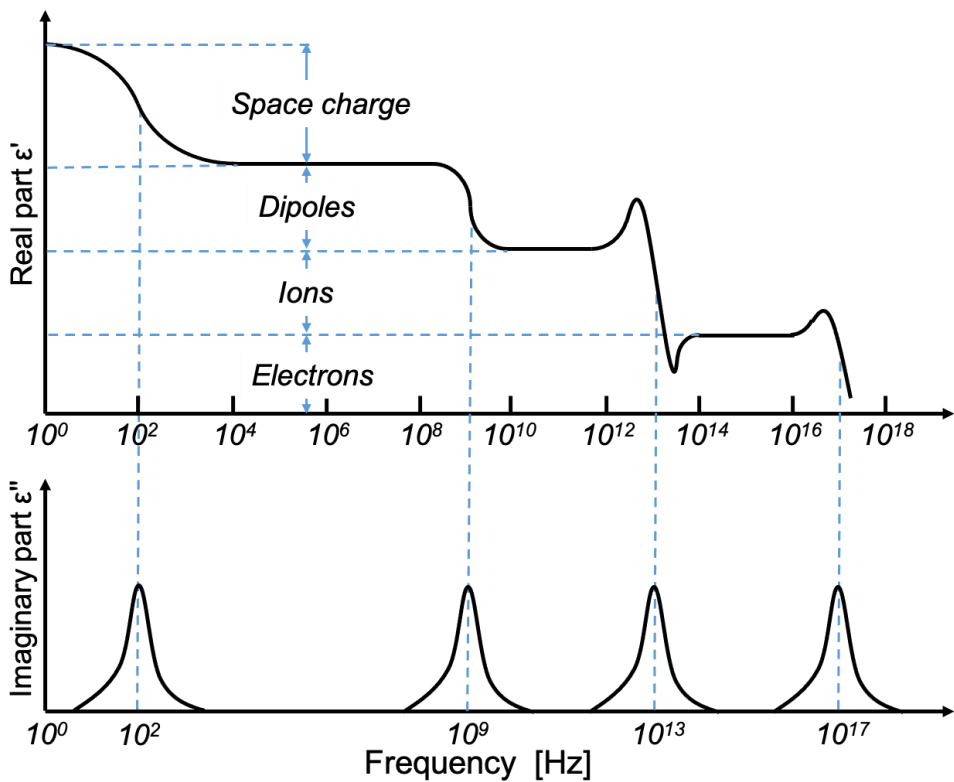


Figure 2.3. Frequency dependence of dielectric polarization mechanisms.

### 2.1.2 Ferroelectricity

Besides the above-mentioned four polarization mechanisms, ferroelectrics are characterized by a spontaneous polarization  $P_s$  which is present in the ferroelectric temperature range and can be switched by a sufficient large external field. The spontaneous polarization is caused by the nonsymmetry of the crystalline structure. Among the 32 crystallographic point groups, 11 are centrosymmetric and 21 are non-centrosymmetric. Except for 432 cubic class, 20 of these 21 non-centrosymmetric classes exhibit piezoelectricity. 10 of these 20 piezoelectric classes possess spontaneous polarization and exhibit pyroelectricity. If the spontaneous polarization is reversible under electric field, the material is ferroelectric. The structural division of dielectric, piezoelectric, pyroelectric, and ferroelectric crystals is sketched in Fig. 2.4.

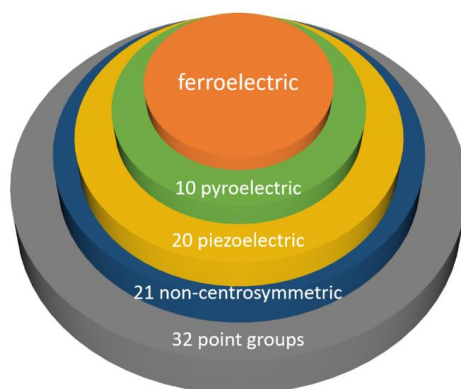


Figure 2.4. Relationship between crystallographic symmetry and piezoelectric, pyroelectric and ferroelectric.

The mechanism of spontaneous polarization varies for the different types of ferroelectrics. Here we take the displacive type ferroelectric  $\text{BaTiO}_3$  as an example to explain the origin of spontaneous polarization. The ferroelectricity of  $\text{BaTiO}_3$  was discovered in 1940s [24], and has attracted great interest for academic research and industrial applications due to its simple structure and excellent electronic properties.  $\text{BaTiO}_3$  is a typical  $\text{ABO}_3$  perovskite, where A- and B-site are  $\text{Ba}^{2+}$  and  $\text{Ti}^{4+}$ , respectively.  $\text{Ti}^{4+}$  is surrounded by 6 adjacent oxygens, forming a  $\text{TiO}_6$  octahedron (see Fig. 2.5). The spontaneous polarization of  $\text{BaTiO}_3$  exists at temperature below 393 K and disappears above Curie temperature  $T_C = 393\text{K}$ . At  $T > T_C$ , the  $\text{BaTiO}_3$  has a cubic unit cell (see Fig. 2.5(a)) since the thermal vibrational energy of  $\text{Ti}^{4+}$  is too large to allow a stable off-centered position. As a result, the  $\text{TiO}_6$  octahedron forms a symmetry center and 6 Ti-O electric dipole moments are equal and opposite, canceling each other ( $P_s = 0$ ). At temperature below  $T_C$ , the effect of the electric interaction between  $\text{Ti}^{4+}$  and  $\text{O}^{2-}$  is stronger than the thermal perturbation, resulting in the deviation of  $\text{Ti}^{4+}$  from the symmetry center. Therefore, the crystal structure is transformed to the tetragonal state (Fig. 2.5(b)), generating a permanent electric dipole moment along the [001] direction (i.e. spontaneous polarization).

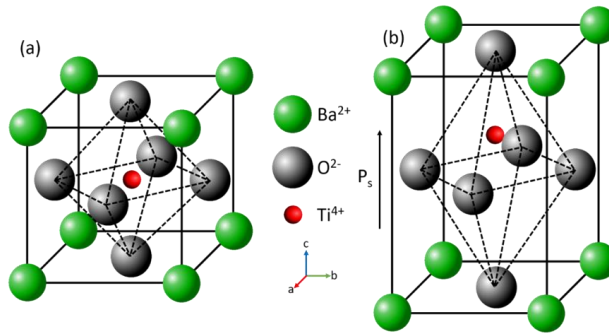


Figure 2.5. Structure of a  $\text{BaTiO}_3$  crystal in the (a) cubic state above the Curie temperature and (b) tetragonal state below the Curie temperature.

The unit cells in a certain small area typically have the same direction of  $P_s$  and, thus, form a ferroelectric domain. Domains are separated by domain walls. The  $P$ - $E$  hysteresis loop represents a macroscopic description of the domain motion. Fig. 2.6 shows a  $P$ - $E$  loop for domains with opposite directions of spontaneous polarization.

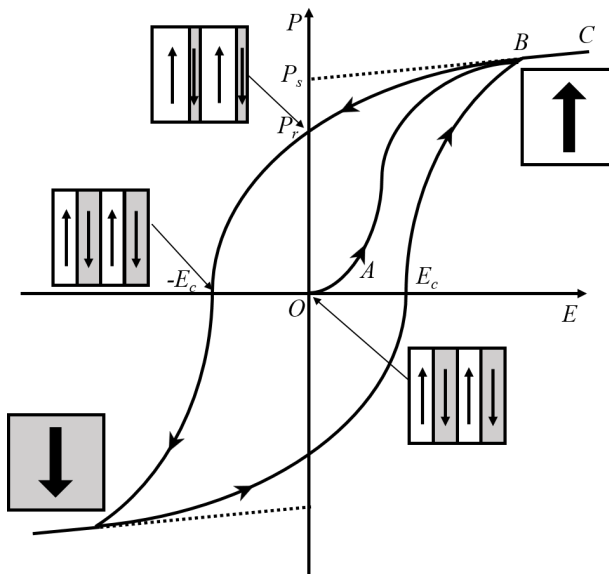


Figure 2.6. Typical  $P$ - $E$  hysteresis loop of ferroelectrics, assuming the domains possess two opposite directions of spontaneous polarization (up and down). In the absence of  $E$ , the initial macroscopic polarization  $P$  is zero (point  $O$ ). In the presence of  $E$ , domains coinciding with the direction of  $E$  extend, while those with opposite direction shrink (segment  $OA$ ). The polarization increases with  $E$ , and will saturate when all the domains align along the direction of  $E$  (point  $B$ ). Then  $P$  increases linearly as  $E$  (segment  $BC$ ). When  $E$  is gradually decreased to 0, most of the polarization persists, resulting in a remnant polarization  $P_r$ . The remnant polarization will disappear when  $E$  reaches  $-E_c$ , which is termed as coercive electric field. A further decrease of  $E$  inverts the polarization.

The ferroelectric domains tend to align along the direction of  $E$ . The motion of the domains is actually realized via the formation and development of new domains as well as the motion of domain walls. Before applying an electric field, the macroscopic polarization of the crystal,

$$P = \frac{\sum \mu}{V} \quad (2.9)$$

where  $\mu$  is the dipole moment and  $V$  is the volume, is zero (initial state point O in Fig. 2.6). When  $E$  is applied, domains coincide with the direction of  $E$  extend and those with opposite direction shrink. As a result, the polarization  $P$  increases with  $E$ , corresponding to section OA in Fig. 2.6. As  $E$  continues to increase, all the domains will align along the direction of  $E$ , leading to a saturated  $P$  (point B in Fig. 2.6). If  $E$  is further increased,  $P$  will increase linearly as  $E$  increases, just like the common dielectrics (see segment BC in Fig. 2.6). The extrapolation of BC to  $E = 0$  defines the spontaneous polarization  $P_s$ . When  $E$  decreases gradually to 0, most of the domains still stay at the polarization direction, resulting in a remnant polarization  $P_r$ . The polarization disappears at coercive field  $-E_c$ . Further decrease  $E$  and  $P$  will saturate again. When  $E$  starts to increase, a similar remnant and coercive  $P$ - $E$  behavior will be observed, forming a hysteresis loop.

### 2.1.3 Ferroelectric phase transition

Ferroelectrics undergo a phase transition from  $T > T_c$  dielectric to  $T < T_c$  ferroelectric phase. In many cases, further transitions from one to another ferroelectric can follow. Generally, upon cooling, the lattice symmetry decreases. A typical phase transition sequence is the one from cubic to tetragonal to orthorhombic to finally rhombohedral, as shown in Fig. 4.2 (a) [25].

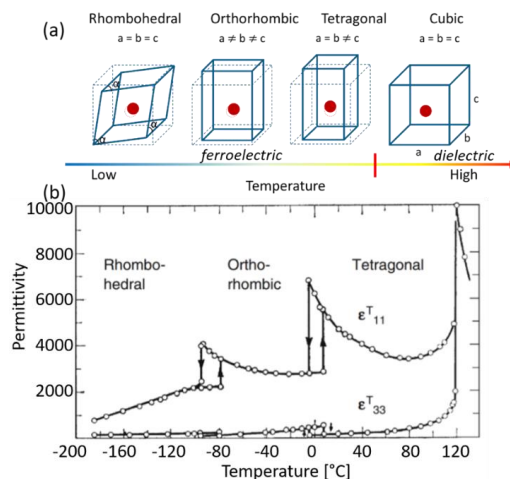


Figure 2.7. (a) Schematic illustration of the structural distortions of the perovskite  $\text{BaTiO}_3$  from cubic ( $T > T_c$ ) to tetragonal, orthorhombic, and finally rhombohedral structures below  $T_c$ . (Reproduced from ref. [25]) (b) Temperature dependence of the permittivity of a signal-domain  $\text{BaTiO}_3$  crystal (Reproduced from ref. [26]).

Fig. 2.7(b) illustrates the phase transitions of a signal-domain BaTiO<sub>3</sub> [26]. At temperatures above  $T_C = 120$  °C, BaTiO<sub>3</sub> has a cubic structure without spontaneous polarization. When cooled below  $T_C$ , BaTiO<sub>3</sub> undergoes a para-to-ferro phase transition, which is resulted from a lattice distortion from the cubic to a tetragonal structure. As a result, a spontaneous polarization along the axes of the  $\langle 001 \rangle_{pc}$  family is generated, where the subscript “pc” represents “pseudo-cubic”. Upon cooling, a ferro-to-ferro phase transition occurs at  $T_{O-T} \approx 0$  °C. This structure conversion from tetragonal to orthorhombic switches the direction of  $P_s$  to the  $\langle 110 \rangle_{pc}$  family. Eventually, a second ferro-to-ferro phase transition appears at around -90 °C, leading to a lattice distortion from the orthorhombic to a rhombohedral structure. Consequently, the direction of  $P_s$  is switched to the  $\langle 111 \rangle_{pc}$  family.

During the ferroelectric phase transitions, the properties of ferroelectrics change strongly, the T-dependence of the permittivity typically shows characteristic sharp peaks at the phase transition temperatures (Fig. 2.7(b)).

#### 2.1.4 Piezoelectricity

In 1880, piezoelectric effect was discovered by Pierre Curie and Jacques Curie in quartz crystals. When a mechanical stress is applied on a piezoelectric crystal, opposite charges of identical amount will be generated on both sides of the crystal, i.e. piezoelectric effect. In opposite, if an external electric field is applied on a piezoelectric crystal, a mechanical strain will be generated. This is termed as the converse piezoelectric effect. Piezoelectric and converse piezoelectric effects are equivalent, i.e. materials exhibiting the piezoelectric effect also possess the converse piezoelectric effect. They can be described by:

$$D_i = d_{ijk} \sigma_{jk}, \text{ and} \quad (2.10)$$

$$S_{ij} = d_{ijk} E_k \quad (2.11)$$

respectively, where  $D_i$  is the dielectric displacement vector,  $\sigma_{jk}$  is the stress tensor,  $S_{ij}$  is the strain,  $d_{ijk}$  is the piezoelectric coefficient, and the subscripts  $i, j$ , and  $k$  represent three axes.

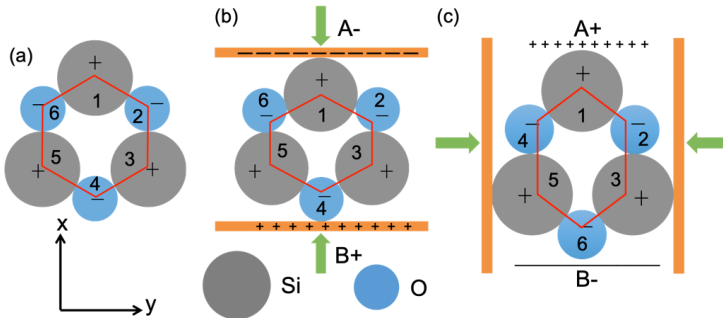


Figure 2.8. Schematic illustration of the origin of piezoelectricity in a quartz crystal showing a piezoelectric material (a) without application of mechanical stress, (b) with a x-axis compressive stress and (c) with a y-axis compressive stress.

It has been shown in [chapter 2.1.2](#) that among the 32 crystallographic point groups, only 20 non-centrosymmetric classes exhibit piezoelectricity. Here quartz crystal is taken as an example to interpret the origin of piezoelectricity in crystals. The chemical formula of quartz is  $\text{SiO}_2$ , and has no center of symmetry. For the convenience of interpretation, Si and O atoms are numbered in [Fig. 2.8](#). Without application of stress, the positive and negative charges centers coincide, i.e. no surface charge accumulation (see [Fig. 2.8\(a\)](#)). When a compressive strain is applied along the x axis, Si atom 1 is squeezed in between O atoms 2 and 6, while O atom 4 is squeezed in between Si atoms 3 and 5. Consequently, surface A is negatively charged, while surface B becomes positively charged (see [Fig. 2.8\(b\)](#)). This type of piezoelectric effect is called longitudinal piezoelectric effect. In case of a y-axis stress, O atoms 2 and 6, as well as Si atoms 3 and 5 will move simultaneously with the same displacement, therefore, no charge will appear on left and right surface. However, Si atom 1 and O atom 4 will be pushed outwards, resulting in a positively charged surface A and negatively charged surface B (see [Fig. 2.8\(c\)](#)). In contrast to the longitudinal piezoelectric effect, this type of piezoelectric effect is called transverse piezoelectric effect. When the quartz crystal is stretched or compressed along the z axis, no bound charges will appear at the surface.

## 2.2 Engineering of ferroelectricity

Typically the best ferroelectric properties, e.g. large permittivity, piezoelectricity and tunability, can be achieved at the para-to-ferro or ferro-to-ferro phase transition temperature. Unfortunately, these temperatures generally deviate from room temperature (RT) [\[26-29\]](#), which represents the operation  $T$  of most electronics. The most commonly used methods to modify the phase transition temperature of ferroelectrics are doping of the material with adequate elements, mechanical strain or the transformation to a so-called relaxor-type ferroelectric.

### 2.2.1 Doping

Doping with higher-charged or lower-charged cations can tune the lattice structure via distortion, tilting, or rotation, which automatically leads to a modification of the ferroelectric properties [\[30-34\]](#).

In the  $\text{K}_x\text{Na}_{1-x}\text{NbO}_3$  system which is the system used for this work, Li, Ta, Sb, and Mn are the most commonly used elements to shift the phase transition temperature [\[35\]](#). A doping with Li will lead to an increase of  $T_C$  with a rate of 8 to 12 °C / mol% and a decrease of  $T_{O-T}$  with a rate of 22 to 35 °C / mol% [\[36-39\]](#). Elements like Sb and Ta are often used to substitute the B-site of  $\text{ABO}_3$ -type perovskites. A doping of Sb will result in a decrease of 22 °C / mol% to  $T_C$  and 12 °C / mol% to  $T_{O-T}$  in  $(\text{K}_{0.48}\text{Na}_{0.52})(\text{Nb}_{1-x}\text{Sb}_x)\text{O}_3$  ceramics [\[40\]](#). It should be noted that Sb is toxic, which limits its application. The doping with Ta decreases  $T_C$  and  $T_{O-T}$  with a rate of 5 to 7 °C / mol% and 3 to 5 °C / mol%, respectively, in  $(\text{K},\text{Na})(\text{Nb}_{1-x}\text{Ta}_x)\text{O}_3$  systems [\[41-43\]](#). Furthermore,  $\text{MnO}_2$  can also markedly decrease  $T_{O-T}$  in  $\text{K}_x\text{Na}_{1-x}\text{NbO}_3$  system [\[44\]](#).

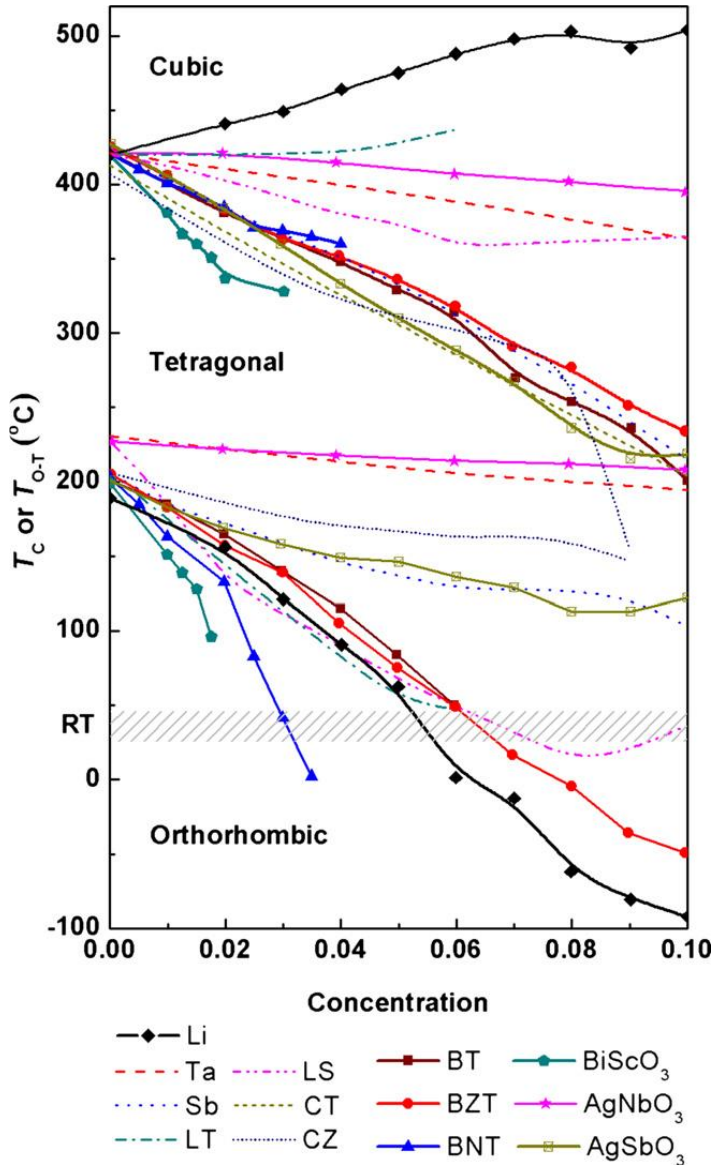


Figure 2.9. Doping effects on the phase transition temperatures of  $\text{K}_x\text{Na}_{1-x}\text{NbO}_3$  ceramics (reproduced from ref. [29]).

The impact of different substitutions on the phase transition temperature of  $\text{K}_x\text{Na}_{1-x}\text{NbO}_3$  ceramics is summarized in Fig. 2.9. Note that various co-doping strategies, e.g. Li-, Ta- and Sb-co-doping, have been investigated recently to further tune the phase transition temperature of  $\text{K}_x\text{Na}_{1-x}\text{NbO}_3$  ceramics and therefore their piezoelectric and ferroelectric properties.

### 2.2.2 Strain

In case of epitaxial strain, the lattice misfit  $\beta$  and the misfit-induced in-plane biaxial strain  $\epsilon_s$  are defined by:

$$\beta = \frac{a_0 - a_{sub}}{a_{sub}} \quad (2.12)$$

$$\epsilon_s = \frac{a - a_0}{a_0} \quad (2.13)$$

where  $a_0$  and  $a$  are the lattice parameters of unstrained and strained films, respectively. And  $a_{sub}$  is the substrate lattice parameter. A positive  $\epsilon_s$  indicates a tensile in-plane strain, whereas a negative  $\epsilon_s$  indicates a compressive in-plane strain (see Fig. 2.10). Due to the Poisson effect, the in-plane strain will be compensated by an opposite out-of-plane strain.

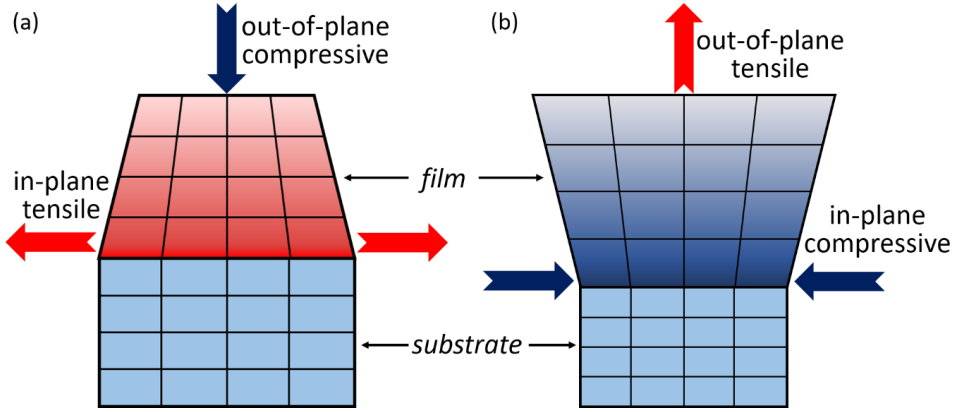


Fig. 2.10. (a) tensile and (b) compressive in-plane strain in epitaxial films. The in-plane strain is compensated by an opposite out-of-plane strain due to the Poisson effect.

The lattice misfit-induced strain will (i) either introduce defects (vacancies, dislocations, or cracks) or (ii) distort the lattice structure so that the electronic properties of ferroelectric will be modified. Pertsev et al [12, 13] first proposed that the epitaxial strain can induce the shift of  $T_C$  for epitaxially grown SrTiO<sub>3</sub> thin films.

Based on a thermodynamic analysis and single-domain assumption, Pertsev et al [13,45] proposed that the shift of  $T_C$  for a SrTiO<sub>3</sub> thin film under a tensile strain is given by:

$$\Delta T_C = 2\epsilon_0 C \frac{Q_{11} + Q_{12}}{s_{11} + s_{12}} \epsilon \quad (2.14)$$

where  $C$  is the Curie-Weiss constant,  $Q_{ij}$  the electrostrictive coefficients and  $s_{ij}$  the elastic compliances.

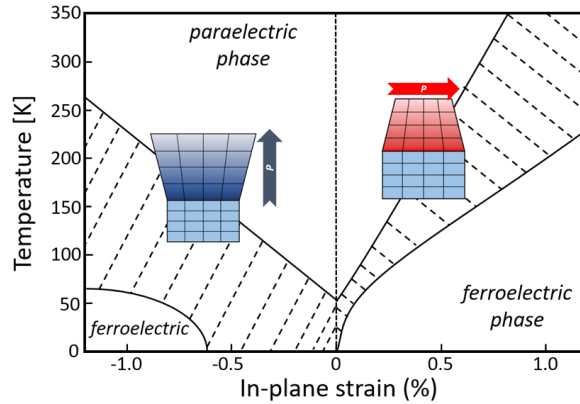


Figure 2.11. Theoretical calculation of the shift of  $T_C$  along the enhanced polarization direction (see arrows in the insets) for  $\text{SrTiO}_3$ . The region marked by black dashed lines represents the expected range of the phase transition temperature, depending on the material constants obtained from the literatures. (Adapted from ref. [45])

The theoretical prediction of  $\Delta T_C$  in  $\text{SrTiO}_3$  system is shown in Fig. 2.11. The  $T_C$  along the tensile-strain direction is always enhanced. The broad distribution of  $\Delta T_C$  (dashed area) is due to the various reported material parameters. The theoretical expectation has been verified by the experimental researches [46].

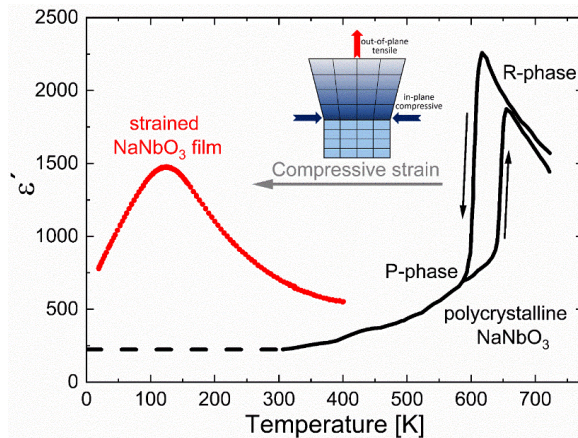


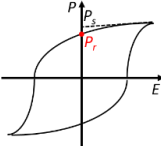
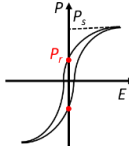
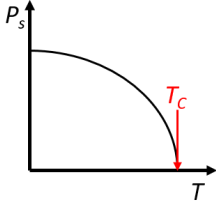
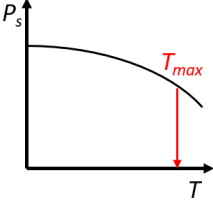
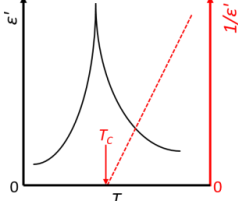
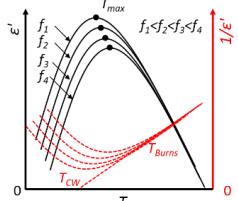
Figure 2.12.  $T$ -dependence of permittivity of unstrained bulk  $\text{NaNbO}_3$  (black line) and compressively strained  $\text{NaNbO}_3$  film (red line). The phase transition of polycrystalline  $\text{NaNbO}_3$  from R-phase antiferroelectric state to P-phase antiferroelectric state at  $\sim 620 - 660$  K is shifted to  $\sim 125$  K. (Adapted from ref. [50])

Cai et al [47-50] later demonstrated a decrease of  $T_C$  in compressively strained  $\text{NaNbO}_3$  thin films (see Fig. 2.12). Their work provided the possibility of tuning the phase transition to a lower temperature via epitaxial strain.

### 2.2.3 Relaxor

Relaxors were first discovered in the BaTiO<sub>3</sub>-BaSnO<sub>3</sub> system in 1954 [51]. The phase transitions of relaxors possess the features of frequency dispersion and electric field dependence, making it convenient to tune their ferroelectricity. Therefore, the introduction of the relaxor is also widely used for the engineering of ferroelectricity.

Table 2.1. Comparison of relaxor-type ferroelectrics and conventional ferroelectrics.

Item	Conventional ferroelectric	Relaxor-type ferroelectric
<i>P-E</i> hysteresis loop	 <ul style="list-style-type: none"> <li>• Typical <i>P-E</i> loop</li> <li>• Strong <math>P_r</math></li> </ul>	 <ul style="list-style-type: none"> <li>• Slim <i>P-E</i> loop</li> <li>• Weak <math>P_r</math></li> </ul>
<i>T</i> -dependence of <i>P</i>	 <ul style="list-style-type: none"> <li>• <i>P</i> decays dramatically with <i>T</i></li> <li>• <i>P</i> drops down to zero above <math>T_C</math></li> </ul>	 <ul style="list-style-type: none"> <li>• <i>P</i> decreases smoothly with <i>T</i></li> <li>• Non-zero <i>P</i> above <math>T_{max}</math></li> </ul>
<i>Phase transition</i>	 <ul style="list-style-type: none"> <li>• Structural phase transition</li> <li>• Sharp and narrow peak</li> <li>• No frequency dispersion</li> <li>• Curie-Weiss law for <math>T &gt; T_C</math></li> </ul>	 <ul style="list-style-type: none"> <li>• Transition of PNR mobility</li> <li>• Broad peak</li> <li>• Frequency dispersive</li> <li>• Curie-Weiss law for <math>T &gt; T_{Burns}</math></li> </ul>

Typically, relaxor properties can be introduced to epitaxial thin films, especially under the presence of plastic strain relaxation [52]. The compositional inhomogeneity in nano-scale contributes to the formation of so-called polar nanoregions (PNR), which are micro- or nano-regions with uniform dipoles. The relaxor ferroelectrics exhibit paraelectric properties at high temperature with the absence of PNRs, which is similar to the paraelectric properties of conventional ferroelectrics. Upon cooling, the relaxors will be turned into an ergodic relaxor state with the presence of randomly distributed PNRs. The PNRs can be re-orientated under E-field, which makes it possible to tailor the ferroelectric and surface acoustic wave properties of the relaxors (see chapter 6).

For better understanding, the main differences between relaxor and conventional ferroelectrics are summarized in table 2.1.

Generally, the differences between relaxors and conventional ferroelectrics are concentrated on three aspects:

- (i) *P-E hysteresis loop*. The PNRs of relaxors tend to distribute randomly with the absence of electric field due to their thermal motion. Consequently, relaxors show a slim *P-E* hysteresis loop with a weak remnant polarization  $P_r$  at zero electric field. In case of conventional ferroelectrics, the spontaneous polarization persists at  $E = 0$ , therefore it shows a strong  $P_r$  and a typical *P-E* loop.
- (ii) *T-dependence of polarization*. Since the PNRs persist above the temperature of maximum permittivity  $T_{max}$ , relaxors show a non-zero polarization above  $T_{max}$ . In contrast, the polarization in conventional ferroelectrics drops dramatically with temperature and reaches zero at  $T_C$ , indicating the disappearance of spontaneous polarization above  $T_C$ .
- (iii) *Phase transition*. Unlike the structural phase transition of conventional ferroelectrics, the phase transition of relaxors implies a decrease of the mobility of PNRs. Consequently, the relaxors normally show a broad and frequency dispersive phase transition in the vicinity of  $T_{max}$ .  $T_{max}$  increases with frequency. Moreover, the Curie-weiss law doesn't apply at  $T < T_{Burns}$ . In contrast, the conventional ferroelectrics show a sharp and narrow phase transition with no frequency dispersion. The permittivity-versus-temperature relation follows nicely the Curie-Weiss law at  $T > T_C$ .

Researchers proposed a series of models to describe the relaxor behavior. Smolenskii et al [53] proposed an inhomogeneous micro-region model which is well accepted to explain the broad transition at the Curie temperature. Cross [54] further improved the model by analogizing local polar micro-regions to spin cluster in superparamagnets, i.e. he developed a "superparaelectric model". Recently, models like dipole glass model [55,56], breathing mode model [57], and random-field model [58,59] are proposed to explain the relaxor state at low

temperature. The difference of these models is essentially focused on the question whether the relaxor state at low temperature is

- (i) a glass state with randomly distributed PNRs that similar to dipolar glasses or
- (ii) a ferroelectric state with the domains broke up into nano scale due to the quenched random electric fields.

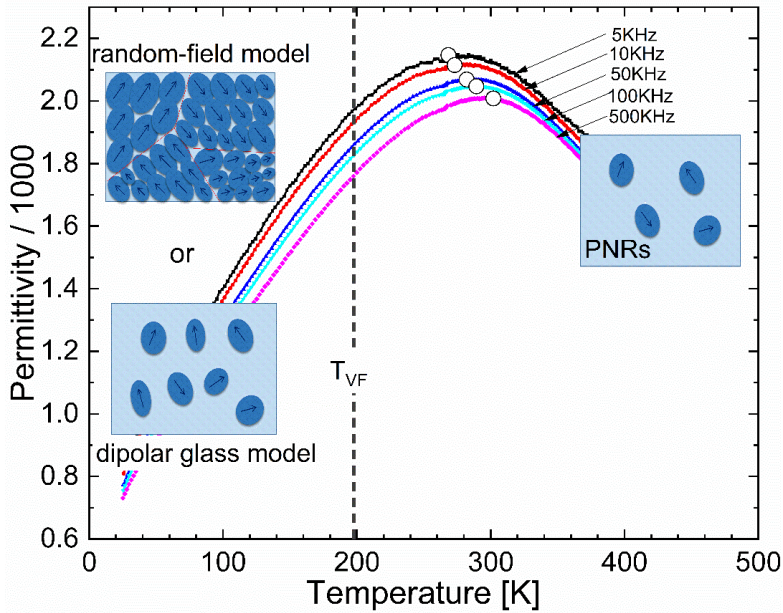


Figure 2.13. Comparison of dipolar glass model and random-field model that describe the evolution of PNRs in an epitaxially strained (K,Na)NbO<sub>3</sub> film. The insets show the different relaxor states at different temperatures. (Adapted from ref. [50])

The evolution of PNRs in an epitaxially strained (K,Na)NbO<sub>3</sub> film is described by two different models in Fig. 2.13. At temperatures  $T_{max} < T < T_{Burns}$ , PNRs are randomly distributed in the matrix. As temperature decreases, the dipolar glass model indicates that a dipolar glass state is formed below the static freezing temperature  $T_{VF} \approx 200$  K, below which PNRs become immobile. In contrast, the random-field model suggests that at  $T_{VF}$  a ferroelectric ordered domain breaks up into nano scale domains which is attributed to the quenched random electric fields.

## 2.3 Surface acoustic waves

Surface acoustic waves (SAW) were first investigated by Lord Rayleigh in 1885 [60]. SAWs represent acoustic waves propagating along the surface (or interface) of materials. The amplitude of a SAW has the maximum value  $A$  at the surface, and it attenuates exponentially with depth into the material. The penetration depth  $d$  of the SAW, which is defined by the attenuation of the amplitude to a value  $A/e$ , depends on wavelength  $\lambda$  which is typically in the  $\mu\text{m}$  range. Therefore, most of the acoustic energy is concentrated near the surface, making the SAW sensitive to surface perturbations like mechanical deformation, physical absorption, or chemical reaction, and thus facilitating sensors applications. Moreover, when coupled with a fluid, the acoustically induced force or pressure can cause steady acoustic streaming that can efficiently drive the liquid or manipulate the particles, enabling a broad range of actuator applications such as liquid mixing, jetting, nebulization, particle manipulation, patterning or sorting [61]. The major applications of SAWs are shown in Fig. 2.14.

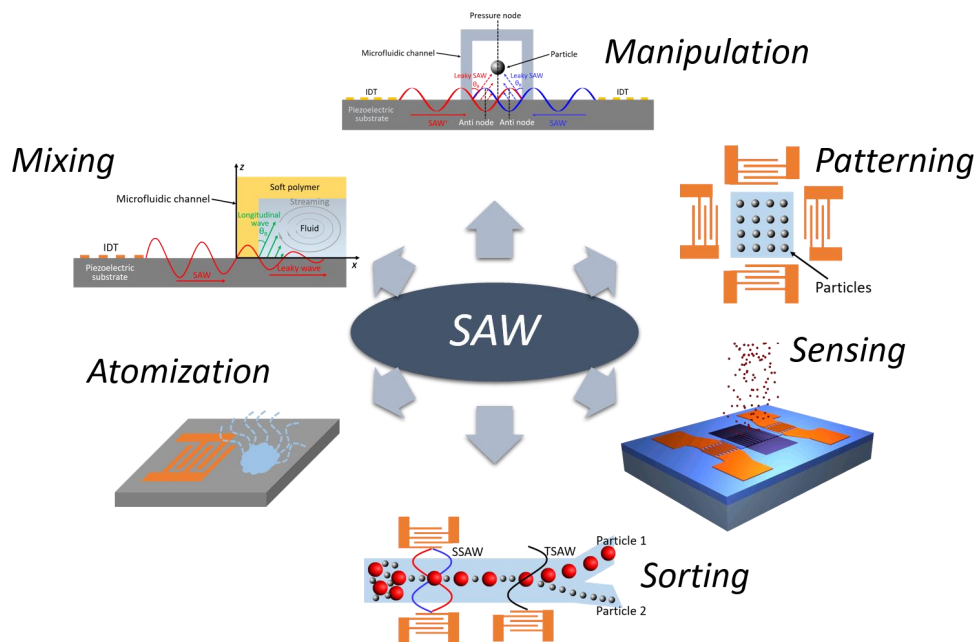


Figure 2.14. Major applications of surface acoustic waves, including liquid mixing and atomization, particle manipulation, patterning, and sorting as well as sensing.

### 2.3.1 Surface acoustic wave modes

Based on the different vibration modes and generation systems (layered or bulk), surface acoustic waves generally can be classified as Rayleigh mode SAW, shear horizontal mode SAW (SH-SAW), Love mode SAW, and Sezawa mode SAW [62]. Fig. 2.15 shows the major modes of SAWs and their vibration schematics.

In the Rayleigh mode, particles on the surface vibrate elliptically, i.e. the Rayleigh wave possesses two vibration components, one normal to the surface, the other parallel to the propagation direction (see Fig. 2.15(a)). The amplitude of Rayleigh waves, which is normally sub-nano meter to a couple of nanometers, decays exponentially with the depth into the substrate. In general, Rayleigh waves can only penetrate one wavelength deep into the propagation media. As a result, most energy of the Rayleigh wave is confined at the surface, which makes it very sensitive to surface perturbations, providing an advantage over bulk acoustic wave (BAW) in case of sensor applications. The Rayleigh waves can operate at fundamental mode or higher orders of harmonics. Especially in thin film systems, the high orders of harmonics can be generated to further improve the operation frequency of the SAWs, which will be discussed in Chapter 5.

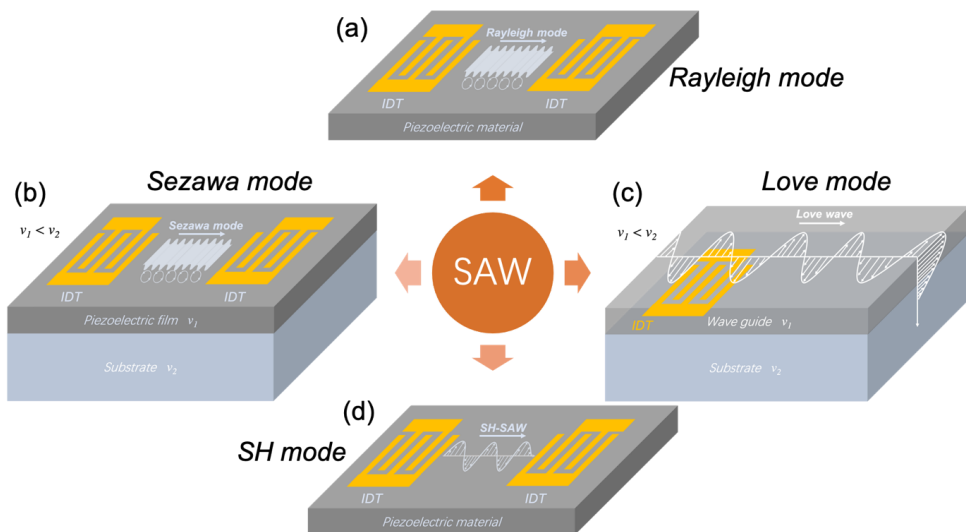


Figure 2.15. Major modes of surface acoustic waves: (a) Rayleigh mode SAW (b) Sezawa mode SAW (c) Love mode SAW and (d) shear-horizontal mode SAW (SH-SAW).

Sezawa waves represent high modes of Rayleigh waves, which are typically generated in “slow-on-fast” layered systems. This means that, in order to generate a Sezawa wave, the acoustic wave velocity in the piezoelectric top layer (for instance a film) should be smaller than that in the non-piezoelectric bottom layer (for instance a substrate) (see Fig. 2.15(b)). Normally the Sezawa wave propagates faster than the corresponding Rayleigh wave, yielding a higher operation frequency, which offers an advantage over fundamental Rayleigh SAWs when applied as a sensor. The effective thickness of the layered system  $t_e = hk$ , where  $h$  is the film thickness and  $k = 2\pi / \lambda$  is the wave vector, determines the generation of Sezawa waves. In general, if  $hk \ll 1$ , the generation of Sezawa waves becomes very difficult, instead, the high orders of Rayleigh waves are generated in the film [63-65].

In the Shear horizontal (SH) mode, particles on the surface vibrate in-plane and perpendicularly to propagation direction (see Fig. 2.15(d)). Since there is no out-of-plane vibration component, SH-SAWs hardly dissipate any energy into a liquid on the surface, which giving this mode an advantage over Rayleigh mode SAWs in liquid sensing applications [66]. For actuation applications, the displacement component normal to the surface is required.

Finally, Love waves are typically generated in layered systems. Generally, in order to generate Love waves, a top layer with a much lower acoustic velocity is deposited on the SH-SAW device as a wave guide (see Fig. 2.15(c)). Consequently, the acoustic energy is mostly trapped in the guiding layer, providing high energy density and thus a high sensitivity. Due to their high sensitivity and the absence of surface-normal displacement components, Love waves are widely used in liquid sensing applications [67].

Generally, compared to BAWs, SAWs have the advantages of a high sensitivity, a possible miniaturization, compactness and integration, and a low-energy cost. These are the reasons why SAWs have attracted extensive interest in academy and industry.

### 2.3.2 Generation and detection of surface acoustic waves

Based on R. M. White and F. W. Voltmer’s work in 1965 [68], SAWs can directly be generated and detected by spatially periodic electrodes, i.e. interdigital transducers (IDT), which can be positioned directly on the surface of a piezoelectric material (see Fig. 2.16).

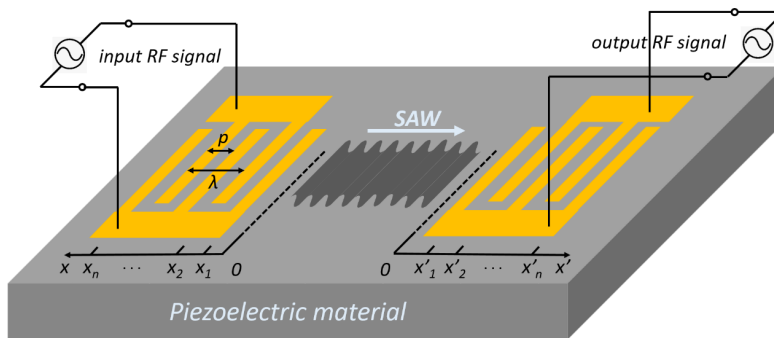


Figure 2.16. Schematic of SAW generation and detection with IDTs on a piezoelectric material.

Input and output IDTs can be used as generator and receiver of SAWs. A periodic electric field is produced when an ac voltage is applied to the input transducer, resulting in a periodic strain field due to the inverse piezoelectric effect. As a consequence, a traveling SAW is generated that propagates bidirectionally with sub-nanometer surface displacement normal or/and parallel to the surface.

The strongest response of the transducer can be achieved if the SAW wavelength  $\lambda$  is equal to the interdigital period  $2p$ , where  $p$  is the electrode pitch, see Fig. 2.16. It corresponds to the fundamental mode of the SAW at the center frequency:

$$f_0 = \frac{v}{2p} \quad (2.15)$$

where  $v$  is the SAW phase velocity in the piezoelectric media. Table 2.2 gives typical phase velocities of SAWs in commonly used piezoelectric materials [69-73].

Table 2.2: Properties, including parameters of the SAW velocity  $v$ , the temperature coefficient of frequency (TCF), the electromechanical coupling coefficient  $K^2$ , and the permittivity  $\epsilon'$ , of commonly used piezoelectric materials for SAW applications.

Material	$v$ (m/s)	TCF (ppm/K)	$K^2$ (%)	$\epsilon'$
YZ LiNbO <sub>3</sub> [69]	3488	-94	4.5	46
128°YX LiNbO <sub>3</sub> [69]	3979	-75.4	5.4	55
XY20°LiNbO <sub>3</sub> [69]	3727	-65	1.6	74
XY120°LiNbO <sub>3</sub> [69]	3403	-75.7	4.1	52
ST-X Quartz [70]	3159.3	0	0.11	3.7
Y-Z LiTaO <sub>3</sub> [70]	3230	35	0.74	-
X-112°Y LiTaO <sub>3</sub> [70]	3301	18	0.64	52
La <sub>3</sub> Ga <sub>5</sub> SiO <sub>14</sub> [71]	2765	7	0.51	-
(001)-<110> GaAs [70]	2864	35	0.07	12.9
ZnO [70]	2645	15	1.8	10
(0001) AlN [70]	5607	19	0.30	8.5
PZT:Nb [72]	2102	-	54	1242
(Na <sub>0.5</sub> K <sub>0.5</sub> )NbO <sub>3</sub> -SrTiO <sub>3</sub> [73]	3120	-345	36.1	888

A *delta-function model* has been proposed by D. Morgan et al to evaluate the transducer response [74]. In this model, every electrode is regarded as a wave source and electrodes reflections are considered to be negligible. Under these assumptions, each electrode can launch a SAW with phase velocity  $v$  and wavenumber  $k = \omega/v$ , where  $\omega = 2\pi f$ . In a linear

system, the SAW at any position can be termed as a superposition of SAWs generated by each electrode. The following discussion partially follows the discussion in ref. [74].

The electrical potential  $\phi_s$  associated with the wave generated by the  $n^{\text{th}}$  electrode is:

$$\phi_{sn}(x, \omega) = VE(\omega)\hat{P}_n \exp[ik(x - x_n)] \quad (2.16)$$

where  $V$  is the input voltage,  $\hat{P}_n$  is defined as the polarity of electrode  $n$  with  $\hat{P}_n=1$  for the live electrodes and  $\hat{P}_n = 0$  for the grounded electrodes,  $E(\omega)$  is an element factor which allows for physical processes. Assuming a linear system, the total wave amplitude can be obtained by summing the contribution of each electrode. Defining  $\phi_s(\omega)$  as the summation potential of  $N$  fingers at  $x = 0$  (see Fig. 2.16) we obtain:

$$\phi_s(\omega) = \sum_{n=1}^N \phi_{sn}(0, \omega) = VE(\omega) \sum_{n=1}^N \hat{P}_n \exp(-ikx_n) \quad (2.17)$$

For simplicity, an array factor  $A(\omega)$  is introduced:

$$A(\omega) = \sum_{n=1}^N \hat{P}_n \exp(-ikx_n) \quad (2.18)$$

Combining eq. 2.17 and eq. 2.18, we obtain  $\phi_s/V = E(\omega)A(\omega)$ .

In a uniform IDT, as shown in Fig. 2.16, the coordinates of electrode centers are  $x_n = np$ , with  $\hat{P}_n = 0, 1, 0, 1, \dots$ . Then  $A(\omega)$  becomes a sum of  $N_p = N/2$  terms:

$$A(\omega) = \sum_{n=1}^{N_p} \exp(-2inkp) = \frac{\sin N_p kp}{\sin kp} \exp[-i(N_p + 1)kp] \quad (2.19)$$

Eq. 2.19 gives a series of maxima at  $kp = n\pi$ , i.e. at  $f_n = nf_0$ .

The amplitude difference between fundamental and harmonics is not reflected in  $A(\omega)$  since the element factor  $E(\omega)$  effect has to be considered [75,76].

In the fundamental mode,  $kp \rightarrow \pi$ . Defining  $\theta = kp - \pi = \pi(f - f_0)/f_0$ , then  $\theta \rightarrow 0$  and  $\sin(kp) = \sin(-\theta) \rightarrow -\theta$ , and the magnitude of the array factor can be approximated by:

$$|A(\omega)| \approx N_p \left| \frac{\sin(N_p \theta)}{N_p \theta} \right| \quad (2.20)$$

Assuming that the element factor  $E(\omega)$  is constant, then the frequency response of  $A(\omega)$  represents the frequency response of the transducer, which is shown in Fig. 2.17. The strongest response occurs at the center frequency  $f_0$  and attenuates as the operation frequency deviates from the center frequency. The zeros next to the fundamental center frequency  $f_0$  occur at:

$$f - f_0 = \pm \frac{f_0}{N_p} = \pm B \quad (2.21)$$

where  $B=f_0/N_p$  is defined as the transducer bandwidth.

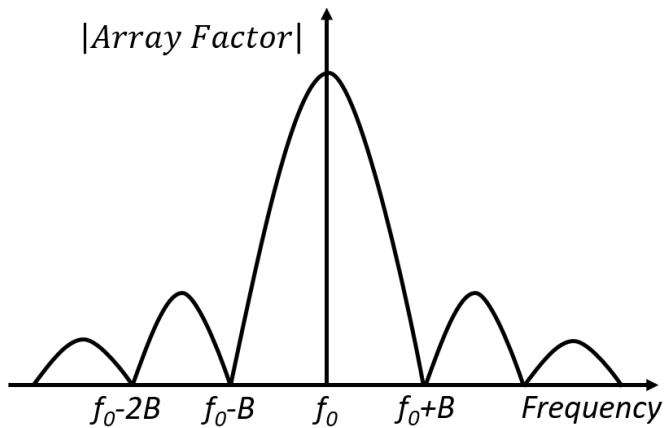


Figure 2.17. Frequency response of array factor  $A(\omega)$  in the region of the fundamental response. The bandwidth  $B=f_0/N_p$  is marked in the figure.

In practice, the SAW system shown in Fig. 2.16 is regarded as a two-port network, the SAW is normally detected by measuring the frequency spectrum of the insertion loss  $IL(\text{dB})=10 \log_{10}(P_{in}/P_{out})$ , where  $P_{in}$  is the input power,  $P_{out}$  is the power received at the output port. The frequency spectrum of insertion loss shows a characteristic  $\sin(X)/X$  behavior, as shown in Fig. 2.18. The SAW information such as bandwidth  $B$ , center frequency  $f_0$ , and phase velocity  $v$  can be extracted from the frequency spectrum and will be discussed in chapter 5.

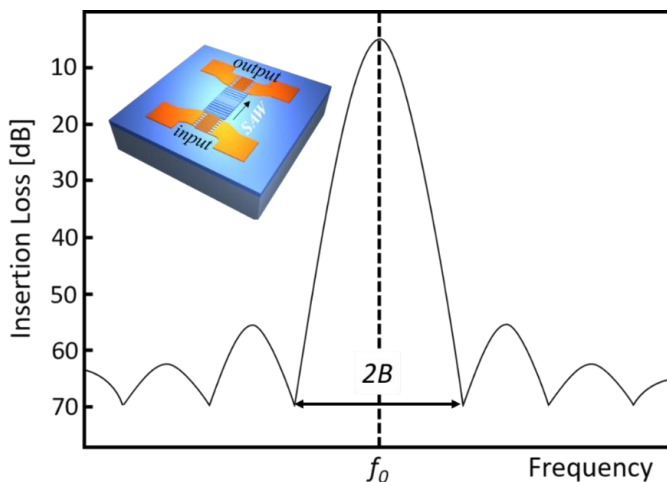


Figure 2.18. Frequency response of insertion loss in a two-port SAW system. The inset shows the layout of a two-port SAW system.

### 2.3.3 Surface acoustic waves sensors

SAW sensors have been extensively developed, which is attributed to their high sensitivity to surface perturbations such as mass loading, chemical absorption, electrical and magnetic interaction, mechanical deformation and more [77-79]. Nowadays SAW sensors are used for sensing temperature, humidity, gas concentration, acceleration, viscosity, pH value, conductivity, electric and magnetic field [80-83]. Combined with specific sensing layers, SAW sensors are even used as biosensors to detect absorbed biomolecules, pathogens, cells, or viruses [84-86]. Furthermore, SAW sensors possess comprehensive advantages of high sensitivity, integration, versatility, miniaturization, low-power consumption, and low cost over other commonly used sensing technologies like BAW sensors, optical sensors, or field effect transistor (FET) sensors [87].

In general, the operation of SAW sensors is realized via measuring the velocity changes of the SAWs, which results from either mechanical or electrical coupling between the SAWs and surface modifications. The velocity change induces a change of center frequency, phase or wave amplitude, which can be recorded and quantitatively be analyzed by recording the frequency response of the IDTs.

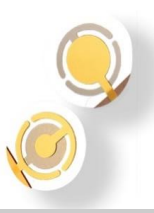
Considering a SAW gravimetric sensor based on a piezoelectric system, the shift of center frequency can be described by the Sauerbrey equation [88]:

$$\Delta f = -\frac{2\Delta m f_0^2}{A\sqrt{\rho\mu}} \quad (2.22)$$

where  $A$  is the piezoelectrically active surface area,  $\Delta m$  is the mass change on the surface area  $A$ ,  $\rho$  and  $\mu$  are density and shear modulus of the piezoelectric material, respectively. Note that eq. 2.22 is valid only if the following three conditions are fulfilled: (i) the loaded mass has to be rigid, (ii) the loaded mass has to be distributed homogeneously and (3) the perturbation of mass loading has to be small, i.e.  $\Delta f/f < 0.05$ .

Eq. 2.22 indicates that the sensitivity of SAW gravimetric sensors can be increased by operating the SAWs at higher frequencies or adjusting the material constants of the piezoelectric substrate. For comparison, resonant frequencies and sensitivities of typical BAW mode (e.g. thickness shear mode (TSM)) and SAW mode sensors are listed in tab. 2.3 [61].

Table 2.3: Comparison between BAW and SAW sensors. (Adapted from ref. [61])

Wave mode	Schematic	Resonant frequency	Sensitivity	Advantages	Drawbacks
<b>Thickness shear mode (TSM)</b>		$f_0 = \frac{v}{2h_0}$ $h_0, \text{ quartz thickness;}$ $v, \text{ acoustic velocity}$	Mass sensitivity: $S_t = -\frac{2f_0}{\rho v} = -\frac{1}{\rho h_0}$ $\rho, \text{ density of quartz}$	<ul style="list-style-type: none"> <li>• Low cost</li> <li>• High Q factor</li> <li>• Mature technology</li> <li>• Easy operation</li> </ul>	<ul style="list-style-type: none"> <li>• Low sensitivity</li> <li>• Difficult to scale down</li> </ul>
<b>Rayleigh mode SAW</b>		$f_0 = \frac{v}{\lambda} = \frac{v}{4d}$ $\lambda, \text{ wavelength;}$ $d, \text{ finger width of IDT}$	Mass sensitivity: $\Delta f = -c_s \frac{\Delta m f_0^2}{A}$ $c_s, \text{ constant of}$ $\text{sensing system}$	<ul style="list-style-type: none"> <li>• Low energy consumption</li> <li>• Low cost</li> <li>• High sensitivity</li> <li>• Wireless control</li> </ul>	<ul style="list-style-type: none"> <li>• High attenuation in liquid environment</li> </ul>
<b>SH-SAW</b>		$f_0 = \frac{v}{\lambda} = \frac{v}{4d}$ $d, \text{ finger width of IDT}$	Mass sensitivity: $\Delta f = -c_s \frac{\Delta m f_0^2}{A}$	<ul style="list-style-type: none"> <li>• Proper for liquid sensing</li> <li>• Wireless control</li> <li>• Low cost</li> <li>• Low energy consumption</li> </ul>	<ul style="list-style-type: none"> <li>• Unwanted spurious modes</li> <li>• Energy lost to bulk wave</li> <li>• Crystal orientation dependence</li> </ul>
<b>Love mode</b>		$f_0 = \frac{v}{\lambda} = \frac{v}{4d}$		<ul style="list-style-type: none"> <li>• Proper for liquid sensing</li> <li>• High sensitivity</li> </ul>	<ul style="list-style-type: none"> <li>• Guiding layer dependence</li> <li>• Complex preparation</li> </ul>

In TSM, which represents a widely applied BAW mode, the resonant frequency  $f_0 = v/2h_0$  is inversely proportional to the thickness  $h_0$  of the piezoelectric material. Limited by the thickness reduction, the TSM sensor can only operate at low resonant frequency of typically kHz to several MHz. Consequently, the use of TSM as gravimetric sensors has a limited sensitivity.

Compared to BAW sensors, SAW sensors exhibit an improved sensitivity and a lower detection limit, which is attributed to their higher operating frequencies. In Rayleigh mode, the fundamental center frequency  $f_0 = v/4d$ , where  $d$  is the finger width. It means the smaller the finger width the higher the operation frequency. Normally the finger width is determined by the lithography and lift-off technique (see chapter 3). By using electron-beam lithography, the dimension of fingers could even be in the nanoscale range, resulting in a resonant frequency up to several GHz to tens of GHz. Eq. 2.22 indicates that  $\Delta f \propto f_0^2$ , which means that a much higher sensitivity can be achieved at higher operating frequencies. Moreover, taking the generation of higher orders of SAW harmonics into consideration, the sensitivity can be further improved (see discussion in chapter 5).

SH-SAW devices are normally used for liquid sensing applications. Since they have no surface-normal displacements, and thus, avoid substantial dissipation of acoustic energy into the liquid. By covering a thin waveguide layer, the SH-SAW can be converted to a Love-mode SAW. In a Love-mode SAW sensor, the acoustic energy will be mostly trapped in the waveguide, yielding an even higher energy density that contributes to the improvement of the sensitivity.

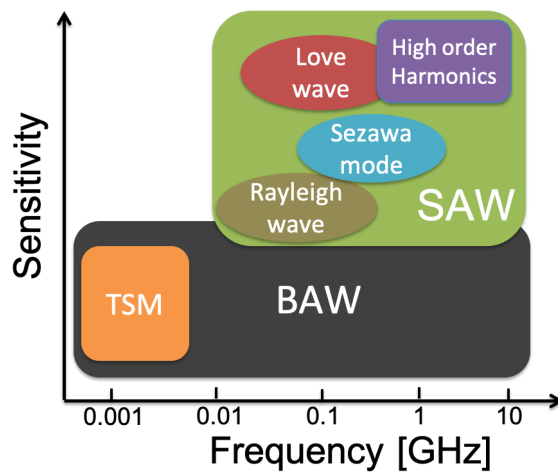


Figure 2.19. Qualitative comparison of sensitivity as a function of operation frequency for typical BAW and SAW modes. (Adapted from ref. [61])

The sensitivities of various acoustic modes as a function of their operation frequencies are qualitatively illustrated in Fig. 2.19 [61].

## 2.4 Introduction to $K_xNa_{1-x}NbO_3$

PZT ceramics are the most commonly used piezoelectric materials these days owing to their high  $T_C$  and large electromechanical coupling coefficient. They show giant piezoelectric response at the so called morphotropic phase boundary (MPB), a typical example is the composition  $PbZr_{0.52}Ti_{0.48}O_3$  [89-91]. The increased piezoelectric response at the MPB is attributed to the co-existence of the tetragonal phase and rhombohedral phase that increases the number of possible domain states at this boundary. PZT-based materials are widely used in ultrasonic transducers, sensors, and actuators. However, PZT-based materials contain the element Pb, which is restricted to use, for instance, in the European Union [92] due to its toxic effects on human health and environment.

One solution would be the use of lead-free alternatives with piezoelectric properties comparable with PZT-based material. One promising lead-free alternative is  $K_xNa_{1-x}NbO_3$ . Already in bulk form, the versatile and outstanding properties have been demonstrated. Furthermore, theoretical predictions revealed the possibility to overcome the absence of such a MPB in many lead-free materials by using anisotropic lattice strain to achieve monoclinicity [93]. The monoclinic phase has an inherent flexibility for the orientation of the electrical polarization, which promises highly flexible domain wall motion and therefore a huge piezoelectric response. Additionally, the ongoing trend of device miniaturization and integration demands the growth of thin films with high crystal quality. Therefore, it is of great significance to develop  $K_xNa_{1-x}NbO_3$  thin film-based materials with excellent piezoelectric properties for applications such as SAW sensors and actuators.

$K_xNa_{1-x}NbO_3$  is a typical complex type of  $ABO_3$  perovskite oxide with  $Na^+$  or  $K^+$  cations occupying the A-site and  $Nb^{5+}$  occupying the B-site. For convenience, a pseudo-cubic lattice can be adopted to describe the crystallographic structure of  $K_xNa_{1-x}NbO_3$  [94,95]. Fig. 2.20(a) shows the pseudo-cubic unit cell of perovskite type  $(K,Na)NbO_3$  crystal at room temperature. In this notation, an orthorhombic unit cell can be represented by a tilted pseudo-cubic cell.

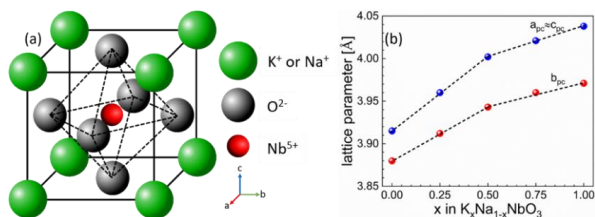


Figure 2.20. Pseudocubic unit cell of a perovskite type  $(K,Na)NbO_3$  crystal (a) and the pseudocubic lattice parameters  $a_{pc}$ ,  $b_{pc}$ , and  $c_{pc}$  as function of potassium content  $x$  (b) (data from ref. [96-100]).

The composition dependence of KNN lattice parameters ( $a_{pc}$ ,  $b_{pc}$ , and  $c_{pc}$ ) are shown in Fig. 2.20(b) [96-100]. For compositions  $x < 0.5$  and  $x > 0.5$ , the lattice parameters of  $K_xNa_{1-x}NbO_3$  can be approximated by a linear fitting of the lattice constants on potassium composition  $x$ .

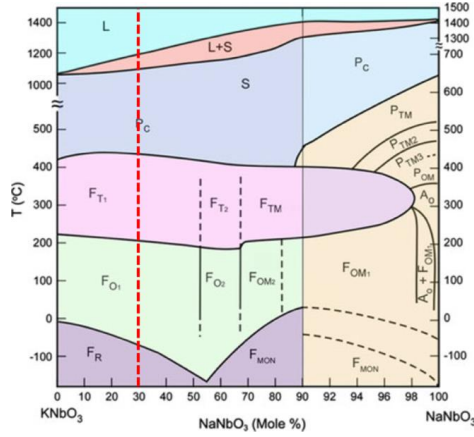


Figure 2.21. Phase diagram of  $K_xNa_{1-x}NbO_3$  system. The symbols L, S, P, A, and F represent liquid, solid, paraelectric, antiferroelectric, and ferroelectric, respectively. The subscripts C, T, O, R, TM, and MON represent cubic, tetragonal, orthorhombic, rhombohedral, pseudotetragonal, and monoclinic respectively. The red line marks the composition investigated in this work. (Reproduced from ref. [29]).

Fig. 2.21 displays the phase diagram of  $K_xNa_{1-x}NbO_3$  [29, 101]. It indicates that, for composition  $x < 50\%$ ,  $K_xNa_{1-x}NbO_3$  undergoes a series of complex phase transitions from high temperature to low temperature, which automatically complicate the system and make it unsuitable for strain engineering. However, for composition  $x > 50\%$ ,  $K_xNa_{1-x}NbO_3$  undergoes only few phase transitions. One of them is the phase transition from  $T > T_C$  cubic to  $T < T_C$  tetragonal ferroelectric phase, the second one is the one from tetragonal ferroelectric to orthorhombic ferroelectric phase. The more concise phase transition behavior of this regime is one of the reasons why we chose potassium sodium niobate samples with a composition of 70% potassium, i.e.  $K_{0.7}Na_{0.3}NbO_3$  for this work.

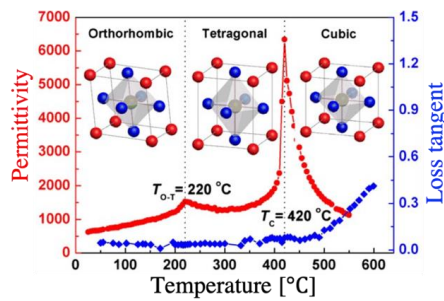


Figure 2.22. T-dependence of permittivity and  $\tan \delta$  of  $K_{0.5}Na_{0.5}NbO_3$  ceramics. The insets show the respective crystal structures of the various phases (reproduced from ref. [29]).

Fig. 2.22 indicates that the transitions occur at  $T_C = 693$  K and  $T_{O-T} = 493$  K for  $K_{0.5}Na_{0.5}NbO_3$  ceramic. Obviously, the highest dielectric constant of  $\epsilon' \approx 6500$  is acquired at the para-to-ferro phase transition temperature.

## 3 Sample preparation and experimental techniques

### 3.1 Sample preparation

The epitaxial  $K_xNa_{1-x}NbO_3$  thin films used in this work were provided by Leibniz Institute for Crystal Growth (IKZ) in Berlin. There, the films were prepared either by metal organic chemical vapor deposition (MOCVD) or pulsed laser deposition (PLD). To investigate the ferroelectric and SAW properties, I designed and fabricated metallic electrodes on these samples via E-beam lithography, lift-off and evaporation deposition techniques, using the cleanroom facilities of the Helmholtz Nanoelectronic Facility (HNF) of the Forschungszentrum Jülich (FZJ). Furthermore, to study the performance of SAW sensors, I deposited organic molecular layer on SAW sensors using an inhouse build molecular layer deposition (MLD) setup. All these 4 deposition techniques are briefly described in the following paragraphs.

#### 3.1.1 Metal organic chemical vapor deposition

MOCVD represents a typical method for preparing high quality epitaxial metal-organic films. It is based on the pyrolysis reaction between the targeted elements and the substrate. One of the main features of MOCVD is the use of organometallic precursors that contain the targeted elements. In contrast to physical deposition techniques, such as evaporation PLD or sputtering, MOCVD offers growth conditions closer to the thermodynamic equilibrium at increased partial oxygen pressure [102]. Consequently, it can provide high-quality thin films with low defect density as well as very smooth surfaces. This is one of the reasons why MOCVD is used in this work for the preparation of  $K_xNa_{1-x}NbO_3$  thin films of high crystalline quality on various scandate substrates, e.g.  $DyScO_3$ ,  $TbScO_3$ ,  $GdScO_3$ , and  $SmScO_3$ , grown by the Oxide & Fluoride group of the IKZ (Berlin) via Czochralski technique.

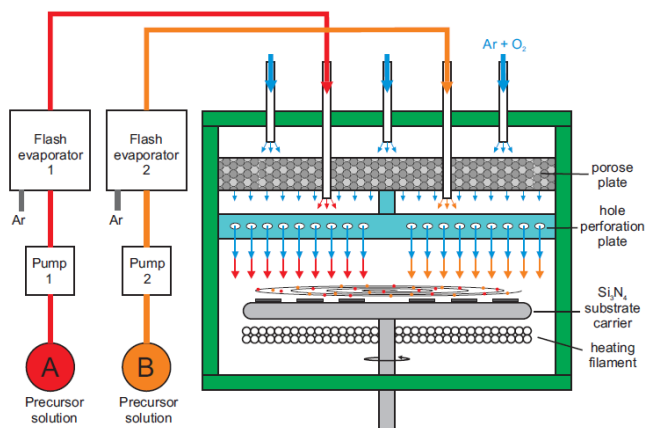


Figure 3.1: Sketch of the MOCVD setup at the IKZ.  $K_xNa_{1-x}NbO_3$  thin films of high crystalline quality were prepared by the IKZ using this method. (Reproduced from ref. [103])

Fig. 3.1 shows a sketch of a MOCVD equipment.  $K(thd)$  and  $Na(thd)$  ( $(thd) = 2,2,6,6$ -tetramethyl-3,5-heptanedione) are applied as precursors of the elements K and Na, respectively, and  $Nb(EtO)_5$  ( $(EtO)_5 =$  penta-ethoxide) is used as the precursor of Nb. All precursors are dissolved in dry toluene before filling them into their reservoirs. During preparation, the precursor solutions (liquid state) are separately delivered by peristaltic pumps to individual flash evaporators for vaporizing. The inert gas Ar is employed to carry the vaporized precursors through heated tubes to the reaction chamber. The MOCVD samples with a typical thickness of 27 to 31 nm were deposited by IKZ in Berlin using the following parameters: substrate carrier rotation rate of 750 r/min to facilitate the mixture of the precursor gases, Ar, and oxygen, thereby improving the homogeneity of the thin films; pressure of 2.6 mbar;  $O_2/Ar$  ratio of 0.6; K/Na precursor ratio of 0.7 : 0.3; substrate carrier (silicon nitride) temperature of 973 K.

### 3.1.2 Pulsed laser deposition

Due to its flexibility, PLD is widely used for thin film preparation. It is used in this work as an alternative route to prepare  $K_xNa_{1-x}NbO_3$  thin films. The resulting films are typically less homogeneous and contain more defects compared to MOCVD films. In chapter 6 we will show that as a result of the inhomogeneity and defect density, the PLD films show a relaxor-type ferroelectric behavior, which offer interesting properties like tunable SAW signals.

Fig. 3.2 illustrates the working principle of PLD. Material of the target in the high vacuum chamber is vaporized by a focused pulsed laser beam, forming a luminous plasma plume. In order to achieve an optimized phase transition, the chamber is floated with oxygen and the substrate is heated to a given temperature. Attributed to the inhomogeneous flux, angular distribution of plume energy and a relatively larger particle energy compared to MOCVD, it is more likely to prepare thin films with local compositional fluctuation via PLD.

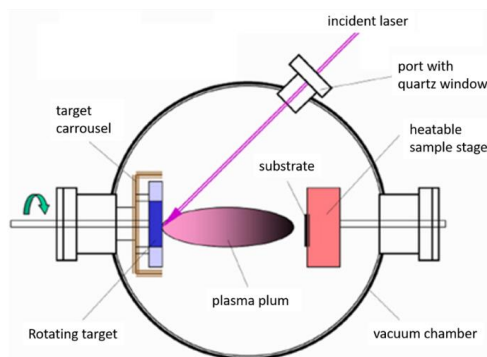


Fig. 3.2: Sketch of a PLD equipment at the IKZ. PLD samples with local compositional fluctuation were prepared by the IKZ using this method. (Reproduced from ref. [97])

We studied  $K_{0.7}Na_{0.3}NbO_3$  films with local compositional fluctuation which were provided by the IKZ in Berlin. There, the films were deposited via PLD onto various (110)-oriented single crystalline scandate substrates using the following deposition parameters: laser energy of  $2.0 \text{ J/cm}^2$ ; frequency 5 Hz; substrate temperature  $600 \text{ }^\circ\text{C}$ ;  $O_2$  pressure 0.3 mbar.

### 3.1.3 Evaporation deposition

To investigate the ferroelectric and SAW properties, I deposited metallic electrodes on the samples via evaporation deposition. The HNF provided the facility and the staffs of the HNF provided technical supports for evaporation deposition. Fig. 3.3 shows a picture of evaporation deposition equipment. During deposition the target material (metal) is heated to a given temperature in a vacuum chamber. Subsequently metal evaporates and travels to the sample surface and then condenses into a film. Electrodes were composed of Pt or Ti/Pt. Furthermore, Cr layers were used for the lithography step (see chapter 3.3).

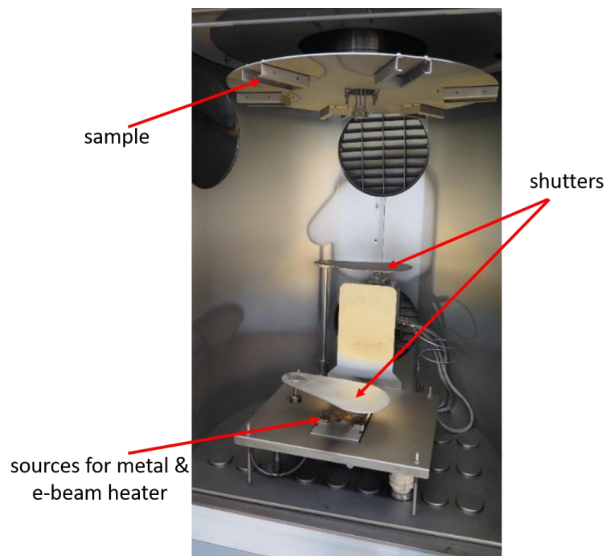


Figure 3.3: Picture of the evaporation deposition equipment in the Helmholtz Nanoelectronic Facility (HNF) of the Forschungszentrum Jülich (FZJ).

### 3.1.4 Molecular layer deposition

In this work,  $K_xNa_{1-x}NbO_3$  thin films are in the end used in SAW sensors. In order to demonstrate their use as a gas sensor or a molecular detector, I deposited organic molecules on the SAW sensor via a homemade MLD setup to monitor the molecular deposition process. This setup is shown in Fig. 3.4. The test samples and the SAW sensor are placed in the MLD chamber which can be evacuated ( $10^{-5}$  mbar) prior to the deposition. Different molecular

sources are connected via valves to the MLD chamber. Moreover, a microwave is attached which allows to generate ozone which is used to clean and activate the sample and the sensor or even remove organic layers which have been deposited on sample and/or sensor in a previous process. Finally, an optical heater (LED, 0 to 90 W) is mounted which allows to manipulate the deposition temperature from RT up to 120 °C.

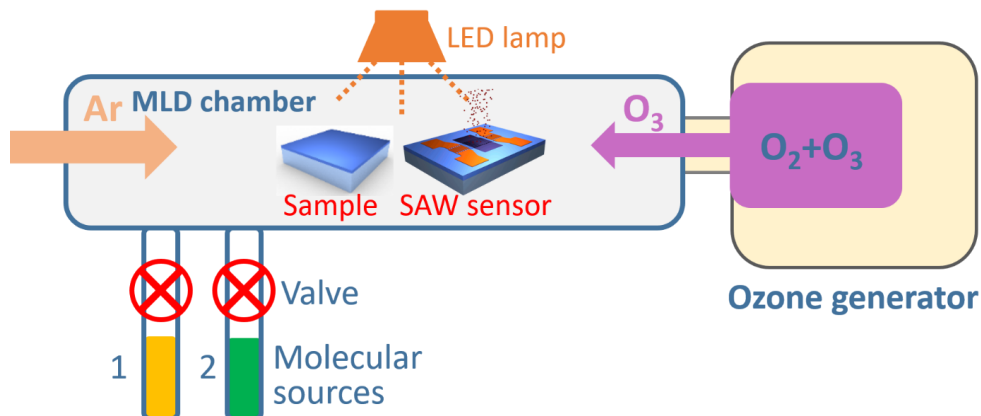


Figure 3.4. Schematic of the molecular layer deposition (MLD) setup. The SAW sensor is integrated into the MLD setup to monitor the process of molecular deposition.

During deposition, firstly, the MLD chamber is floated with 100 sccm pure oxygen (99.9%), yielding a pressure of around 1 mbar. Then, a microwave is used to convert oxygen into ozone to clean (removal of organic residue or previous layer) and activate the sample surface. After that, the oxygen is switched off and Ar is switched on (0 to 100 sccm) to provide the desired process pressure and atmosphere for the molecular deposition. Finally, the valve of the molecular source is opened for deposition. The Ar pressure defines among others the vapor pressure and, thus, deposition rate of the molecules.

In this thesis, the deposition of two different molecules—(3-aminopropyl)-triethoxysilane (APTES) and (3-glycidioxypropyl)-trimethoxysilane (GLYMO)—are monitored via in situ detection with our novel thin film KNN SAW sensors. APTES and GLYMO are typically deposited in an Ar atmosphere with a pressure of 0.8 mbar and 0.1 mbar, respectively, using a deposition time of 10 min (APTES) and 1 hour (GLYMO). A monolayer thickness of approximate 0.7 nm and 0.3 nm are expected for APTES and GLYMO, respectively [104].

### 3.2 Film characterization

After sample preparation, structure, stoichiometry, morphology, and thickness of the films are characterized. The corresponding techniques, such as high resolution X-ray diffraction

(HR-XRD), atomic force microscopy (AFM), reciprocal space mapping (RSM), and time-of-flight secondary ion mass spectroscopy (ToF-SIMS) are introduced in this chapter.

### 3.2.1 High resolution X-ray diffraction

X-rays are electromagnetic waves with wavelength of 0.01 to 10 nm, which can be diffracted by the material. By measuring the intensities and angles of diffracted beams, XRD can be used to analyze the material's structure. Most scattered X-rays interfere in a destructive manner, constructive interference only occurs if the incident X-ray fulfills Bragg's law (see Fig. 3.5(a)):

$$n\lambda = 2d_{hkl}\sin\theta \quad (3.1)$$

where  $n$  is an integer,  $\lambda$  the X-ray wavelength,  $\theta$  the incident angle, and  $d_{hkl}$  is the interplanar distance of  $(hkl)$  crystal planes.

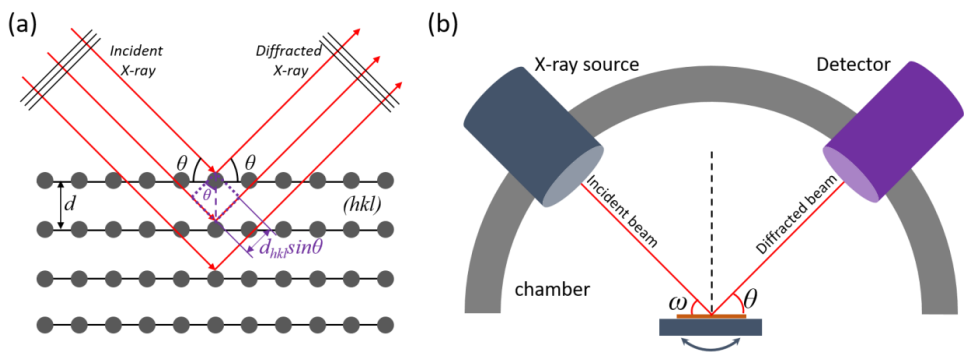


Figure 3.5. (a) Sketch of the Bragg diffraction. (b) Sketch of an XRD Bragg-Brentano scan. (Adapted from ref. [25])

The Bragg-Brentano scan is the most commonly used method for XRD measurements. The geometry is shown in Fig. 3.5(b), indicating that the angles of incident and detected X-ray beams are identical, i.e.  $\omega = \theta$ . The intensity is recorded by the detector as function of the angle. By analyzing these XRD data (e.g. Nelson-Riley fit), parameters like the lattice constants or film thickness  $t$  can be determined.

Using a Goebel mirror in combination with a GeO22ACC monochromator, a well collimated and monochromatic radiation can be achieved for the so called high resolution X-ray diffraction which allows for an accuracy of  $\Delta d/d \approx 10^{-4}$ . The high resolution XRD technique allows extremely accurate analysis of crystalline structure, stain effect and relaxation effect in thin epitaxial film. This is one of the reasons why it is used in this work.

Moreover, in analogy to the intensity modulation in single-slit diffraction experiment, Laue oscillations arise around the Bragg reflection for films with smooth surface and small interface

roughness [105]. They allow for an evaluation of film thickness with an accuracy of  $\pm 1$  nm according to:

$$t = \frac{\lambda \cdot \sin(\theta)}{\Delta\omega \cdot \sin(2\theta)} \quad (3.2)$$

where  $\Delta\omega = \frac{\Delta 2\theta}{2}$ , is the oscillation period. Fig. 3.6 shows an example of HR-XRD measurement for a 30 nm  $K_{0.7}Na_{0.3}NbO_3$  film on (110)  $TbScO_3$ , showing one major reflex of the substrate ((110)  $TbScO_3$ ) and film ((110)<sub>pc</sub> KNN), and a series of Laue oscillations with angular spacing  $\Delta 2\theta$ .

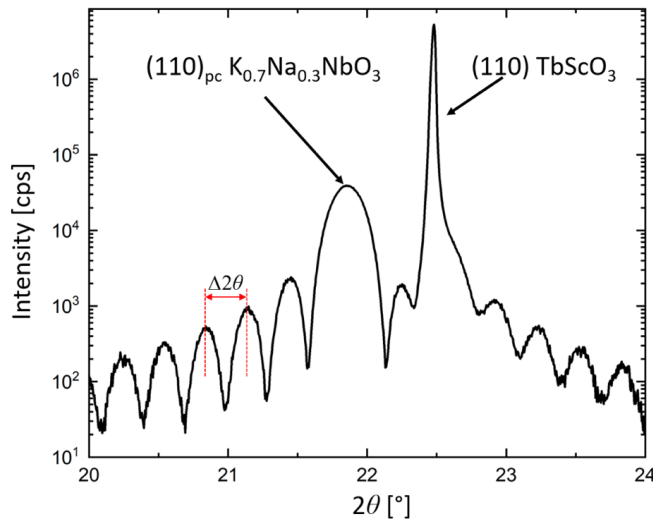


Figure 3.6. High resolution XRD Bragg-Brentano scan of a 30 nm  $K_{0.7}Na_{0.3}NbO_3$  film on (110)  $TbScO_3$ . The major two peaks are ascribed to (110)<sub>pc</sub>  $K_{0.7}Na_{0.3}NbO_3$  and (110)  $TbScO_3$ , and reveal the [110] lattice parameter of substrate and film, respectively. The intensity oscillation period,  $\Delta 2\theta$  marked by the double-headed arrow reveals the film thickness.

### 3.2.2 Reciprocal space mapping

RSM is basically an extended XRD technique in which an extended angular range of  $\omega$  and  $\theta$  in the vicinity of characteristic Bragg diffractions are scanned, yielding a 2-dimensional map of Bragg diffractions that provides structural information of film and substrate.

Fig. 3.7 illustrates the working principle of RSM. For better understanding, the Ewald sphere is introduced to analysis the reciprocal space. Considering X-ray beams with wave vector  $k$ , wavelength  $\lambda$ , and an incident angle  $\omega$ , an Ewald sphere with the radius of  $2\pi/\lambda$  is introduced. The intersection angle of the detector and incident beam is fixed to  $2\theta$ . Consequently, the parallel and normal components of the scattering vector  $q = k' - k$  can be described as:

$$q_{\parallel} = \frac{2\pi}{\lambda} [\cos(2\theta - \omega) - \cos(\omega)] \quad (3.3)$$

and

$$q_{\perp} = \frac{2\pi}{\lambda} [\sin(2\theta - \omega) + \sin(\omega)] \quad (3.4)$$

Two scan modes, i.e.  $\omega$  and  $\omega-2\theta$  scan, are combined to scan the reciprocal space in two orthogonal directions, yielding a 2-dimensional distribution of diffraction intensity, i.e. RSM. In case of  $\omega$  scan, the detector is fixed and the sample is free to rotate, resulting in a constant length but variable direction of  $\mathbf{q}$  vector. In case of  $\omega-2\theta$  scan, the detector and sample are rotated simultaneously with an angular ratio of 2 : 1, leading to a fixed direction but variable length of  $\mathbf{q}$  vector.

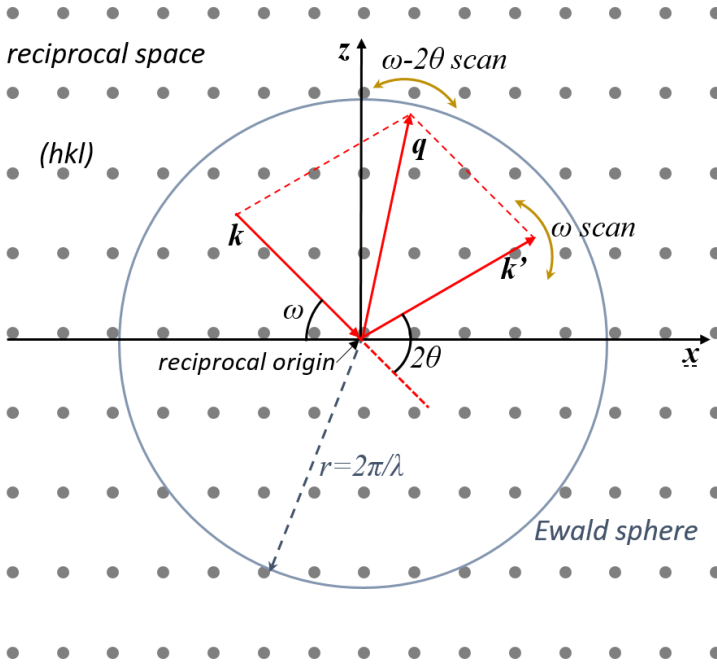


Figure 3.7. Mechanism of the RSM measurement. A 2-dimensional Ewald sphere with a radius of  $2\pi/\lambda$  is applied to describe the reciprocal space (adapted from ref. [106]).

Fig. 3.8 shows a RSM result, the coincidence of  $q_{\parallel}$  of  $(444)_{\text{o}}$  TbScO<sub>3</sub> and  $(402)_{\text{pc}}$  K<sub>0.7</sub>Na<sub>0.3</sub>NbO<sub>3</sub> indicates the epitaxial growth, whereas the broadness and its distortion in the direction of unstrained KNN (white dots in Fig. 3.8) indicate a clear relaxation of the strained KNN film. A detailed discussion of the RSM experiments is given in chapter 4 and chapter 6.

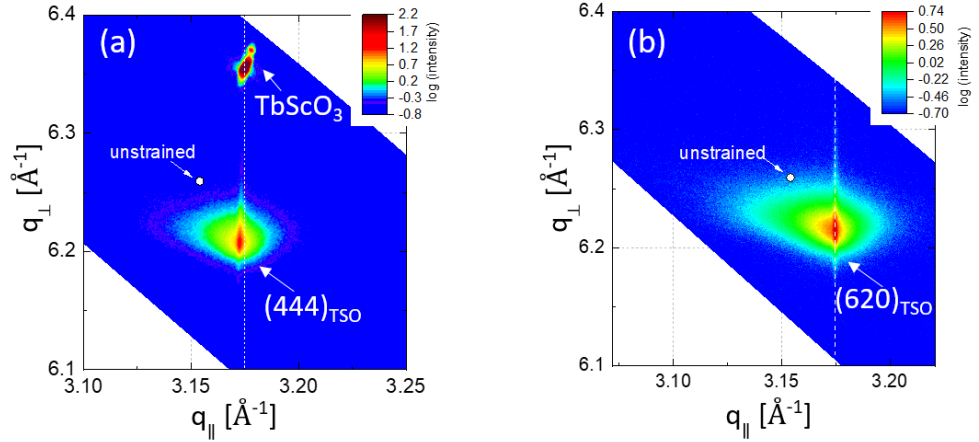


Fig. 3.8: High resolution x-ray diffraction RSM in the vicinity of the  $(444)_{\text{TSO}}$  (a) and  $(620)_{\text{TSO}}$  (b) for a 27 nm thick  $K_{0.7}\text{Na}_{0.3}\text{NbO}_3$  film. The white dots mark the expected position of unstrained film. (Measurement D. Pfützenreuter, IKZ Berlin)

### 3.2.3 Atomic force microscopy

Atomic force microscopy (AFM) analyses were applied to characterize the morphology and, thus, quality of the prepared films. The working principle of AFM is illustrated in Fig. 3.9 (a). The key component of AFM is a cantilever with a sharp tip at its free end, which can scan over the sample surface. When the tip approaches the sample surface, the tip-sample interaction forces, e.g. van der Waals force, atomic binding force, electrostatic force, magnetic force, or Casimir force, result in a deflection of the cantilever. Generally, the deflection of the cantilever can be detected by the photodiode that collect the laser beam reflected by the cantilever. The most commonly used working modes of AFM include contact mode and non-contact mode. The tip is “dragged” across the surface in contact mode to measure the morphology by detecting the deflection of the cantilever. Since the tip directly contacts the sample surface, the tip and sample are easy to be damaged in this mode after several times of measurement. Therefore, the contact mode is normally only used if the overall tip-sample force is repulsive. The non-contact mode typically doesn’t damage the tip and the sample because the tip doesn’t touch the sample surface but oscillates at its resonant frequency (or slightly higher) just above the surface. The force between the tip and sample will change the resonant frequency and amplitude, a feedback system is applied to adjust the average tip-to-sample distance to keep the resonant frequency or amplitude constant. The morphology of the sample is constructed by recording the tip-to-sample distance at each position.

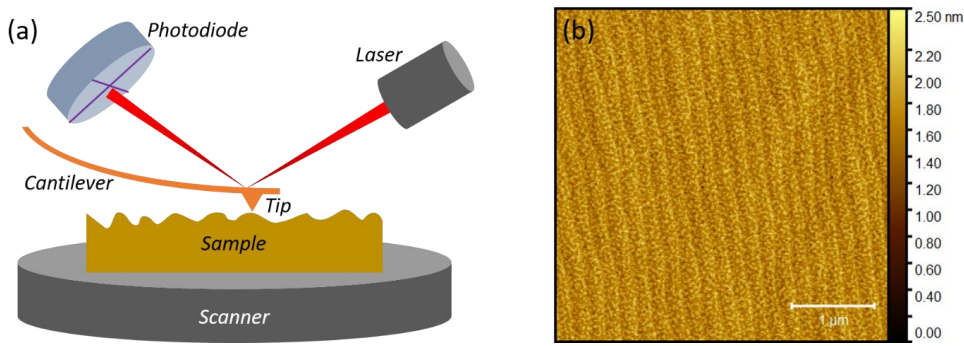


Figure 3.9. (a) Typical configuration of an AFM setup and (b) example of the morphology of a 29 nm thick  $K_{0.7}Na_{0.3}NbO_3$  film on  $GdScO_3$  substrate measured by AFM.

Compared to optical microscopy and scanning electron microscopy, AFM has advantages of:

- (i) high resolution down to fractions of nanometer, which is 3 order of magnitude lower than the optical diffraction limit.
- (ii) doesn't need any special treatment to the sample because the AFM can characterize both conductive and nonconductive samples.
- (iii) can work at the atmosphere environment, which is suitable for samples that can't survive under vacuum like bio-objects or others.

The AFM measurements were performed by the IKZ in Berlin and then I did the data analysis and interpretation. The result of an AFM measurement is shown in Fig. 3.9 (b). It shows a PLD sample of 29 nm KNN film on GSO substrate possess a smooth surface with a root mean square (RMS) roughness of 0.2 nm.

### 3.2.4 Time-of-flight secondary ion mass spectroscopy

ToF-SIMS is applied in this work to confirm the composition of the prepared KNN films. The working principles of ToF-SIMS is illustrated in Fig. 3.10(a). A focused incident ion beam (e.g.  $Ar^+$ ,  $Xe^+$  and  $O^-$ ) is used as primary ion source to sputter the sample surface. The atoms or atomic clusters, as well as positive and negative ions that absorb the energy of the primary ion beam will be ejected from the surface. These ejected secondary ions will be collected and analyzed by a mass spectrometer to provide the information of surface composition, depth profile, isotope etc.

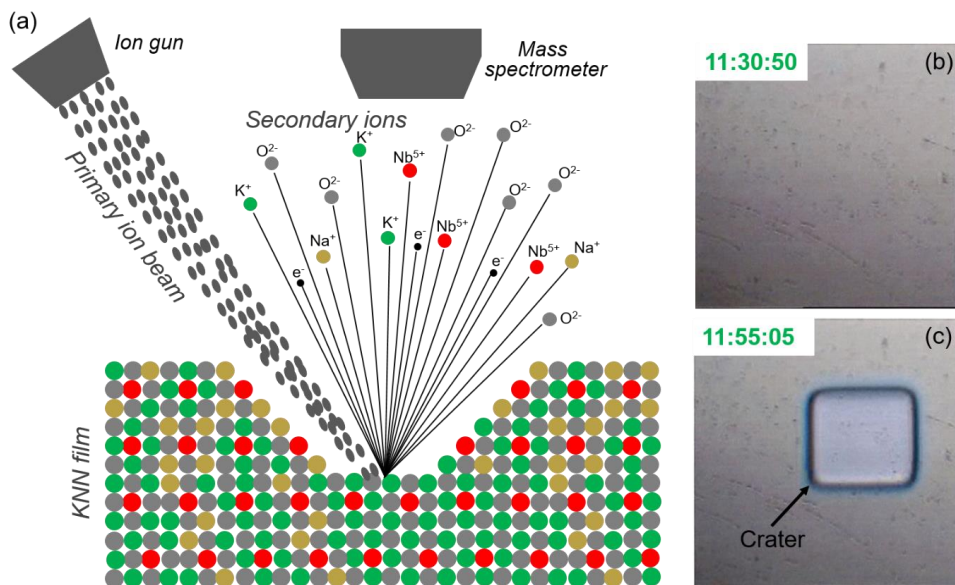


Figure 3.10: (a) Working principles of the ToF-SIMS measurement and surface morphology of a 150 nm-thick  $K_{0.7}Na_{0.3}NbO_3$  film grown on Si: (b) before ToF-SIMS measurement and (c) after 20 min ToF-SIMS measurement. The green numbers refer to the time of the experiment and the arrow shows the position of the crater resulted from the removing of the material.

There are two working modes for ToF-SIMS measurement: (i) “dynamic mode” (D-SIMS), and (ii) “static mode”(S-SIMS). The difference is the density of the ion beam. For the “D-SIMS” mode the ion beam density is relatively smaller and the detected area is larger, it is normally used for surface composition analysis. For the “S-SIMS” mode a relatively larger ion beam allows to focus on a relatively smaller area for depth profile analysis.

Fig. 3.10 (b) and (c) show the morphology change of a 150 nm thick  $K_{0.5}Na_{0.5}NbO_3$  layer on Si after 20 min ToF-SIMS measurement (“D-SIMS” mode) showing a  $300 \times 300 \mu m^2$  crater resulted from the removing of the material.

In order to analysis the composition of KNN films, a series of  $K_xNa_{1-x}NbO_3$  thin film systems with known composition of  $x = 0.1, 0.3, \text{ and } 0.5$  are used for ToF-SIMS measurements to calibrate the mass spectrum. The depth profiles of 3 elements (Na, K, Nb) of these films are shown in Fig. 3.11.

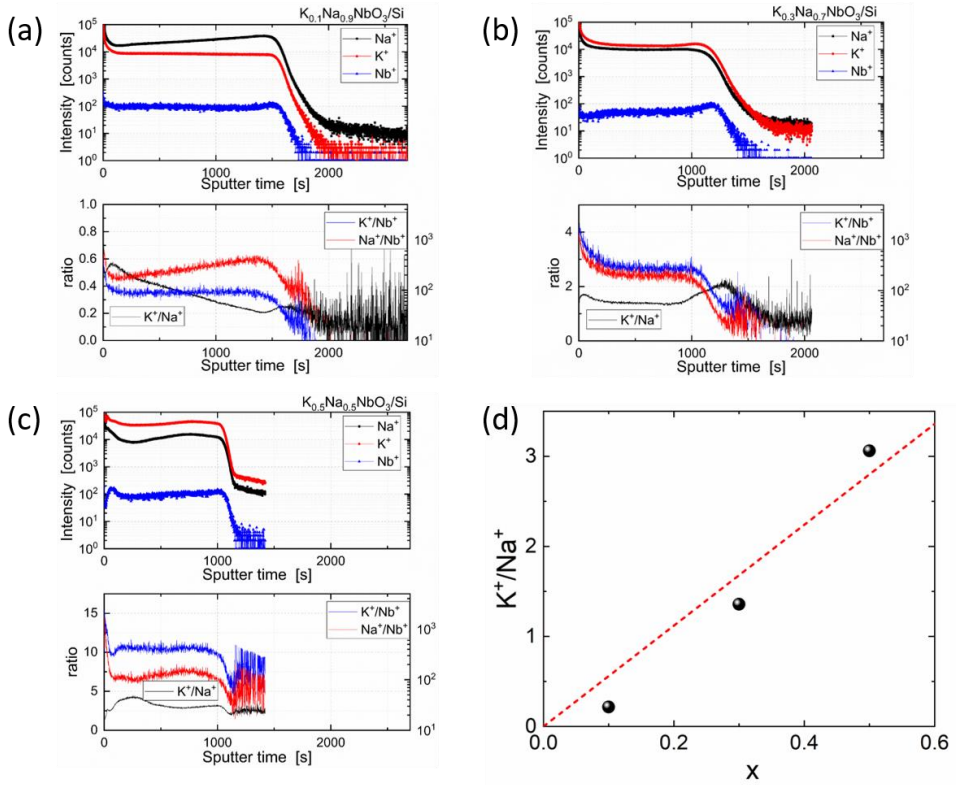


Figure 3.11. Depth profiles of  $K_xNa_{1-x}NbO_3$  films: (a)  $x = 0.1$ , (b)  $x = 0.3$ , and (c)  $x = 0.5$  obtained via ToF-SIMS ("S-SIMS" with ion beam energy 30 keV, ion current 2600 pA on a  $41 \times 41 \mu m$  area). The resulting linear dependence of intensity ratio  $K^+/Na^+$  on potassium composition is shown in (d). (Measurement: U. Breuer, Forschungszentrum Jülich)

A linear fit of the  $K^+/Na^+$  signal ratio as function of the composition  $x$  (see Fig. 3.11(d)) is used as a calibration for the determination of the composition of the KNN films.

### 3.3 Electrodes fabrication

For the electronic characterization and measurements, different types of metallic electrodes had to be prepared on the thin film. These electrode structures include:

- (i) interdigital capacitor structures for permittivity measurements (interdigitated electrodes (IDE)),
- (ii) interdigital transducers for SAW measurement (interdigitated transducers (IDT)),
- (iii) Pt temperature sensor for local temperature detection, and
- (iv) resistance heater for temperature control.

For convenience all electrodes are prepared simultaneously and from the same material combination, i.e. 45 nm Pt on 5 nm Ti adhesion layer. All electrodes and temperature sensors were designed and fabricated using the facilities of the HNF of the FZJ for E-beam lithography and lift-off. The recipe for the lithography and lift-off is based on standard procedures developed in the HNF over the past years which have been adopted and improved for our systems by former colleagues [25,50] and myself. I especially used a larger E-beam power for the writing and added a plasma cleaning step to remove the remnant PMMA, which have a significant impact on the performance of our SAW devices. The specific recipe for all steps is sketched in [table 3.1](#) and described in detail in the [appendix](#).

Table 3.1. Summary of E-beam lithography and lift-off recipe, the sketches show cross section (left) and top view (right).

Step	Process	Description	Cross Section Sketch	Top View Sketch
1	Cleaning	<ul style="list-style-type: none"> <li>Aceton, UB, 5 min</li> <li>Isopropanol, UB, 5 min</li> <li>Drying by N<sub>2</sub> gun</li> </ul>		
2	PMMA coating	<ul style="list-style-type: none"> <li>4000 rpm</li> <li>1 min</li> </ul>		
3	Baking	<ul style="list-style-type: none"> <li>140 °C</li> <li>30 min</li> </ul>		
4	Cr deposition	<ul style="list-style-type: none"> <li>10 nm</li> </ul>		
5	E-beam lithography	<ul style="list-style-type: none"> <li>300 μC/cm<sup>2</sup> or</li> <li>600 μC/cm<sup>2</sup></li> </ul>		
6	Cr etching	<ul style="list-style-type: none"> <li>12 s etching</li> <li>Rinsing and drying</li> </ul>		
7	Development	<ul style="list-style-type: none"> <li>AR-600-55, 2 min</li> <li>Isopropanol, 1 min</li> <li>Drying</li> </ul>		
8	O <sub>2</sub> plasma treatment	<ul style="list-style-type: none"> <li>200 sccm O<sub>2</sub> flow</li> <li>300 W for 5 min</li> </ul>		
9	Electrodes deposition	<ul style="list-style-type: none"> <li>5 nm Ti</li> <li>45 nm Pt</li> </ul>		
10	Lift-off	<ul style="list-style-type: none"> <li>Aceton, 5 min</li> <li>Isopropanol, 1 min</li> <li>Drying</li> </ul>		

Fig. 3.12 shows a sketch of a sample with various integrated electrode structures for the measurements of SAW, permittivity, and local temperature.

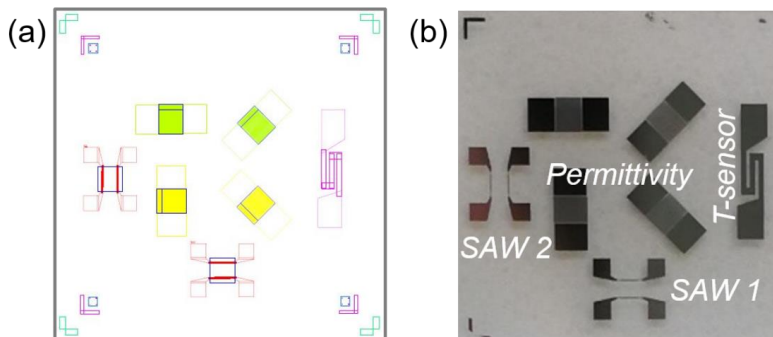


Figure 3.12. (a) AutoCAD design, (b) resulting sample after e-beam lithography and lift-off showing a sample with interdigital electrodes (IDE) for permittivity measurement, interdigital transducer (IDT) for SAW measurement, and temperature sensor for temperature monitoring. Electrode structures along different directions are designed to investigate the anisotropic properties of the thin film.

### 3.4 Electronic characterization

The resulting samples with various types of electrode structures (IDEs, IDT, and T-sensor) are mounted on the corresponding sample holders for different types of measurements ranging from cryogenic permittivity or SAW experiments to SAW sensor test. The sample holders with sample are then connected with the corresponding external devices for different electronic characterizations, as shown in Fig. 3.13.

Fig. 3.14 shows the measurement configuration based on a cryostat (CF1200), which is used in this thesis for T-dependent measurements. The sample is fixed on a “stick” that connected to external electronic measurement devices and inserted into the inner chamber of the cryostat. Cooling and heating of the sample are realized via liquid Helium and a homemade resistive heater, respectively, this enabling stable temperatures from 4 to 500 K. A LCR meter (Sourcetronic ST2826A or ST2826) is connected to measure permittivity of the film, high frequency signal generators (Hewlett Packard E4422B, 250 kHz to 4.0 GHz, or Keithley 2820, 400 MHz to 6.0 GHz) are used to provide high frequency (HF) signals for the SAW generation and spectrum analyzers (Anritsu MS2661C, 9 kHz to 3 GHz, or Keithley 2920, 400 MHz to 6 GHz) are used to record the SAW signal. All devices are controlled via a computer using Labview, which was programmed in cooperation with Prof. Roger Wördenweber.

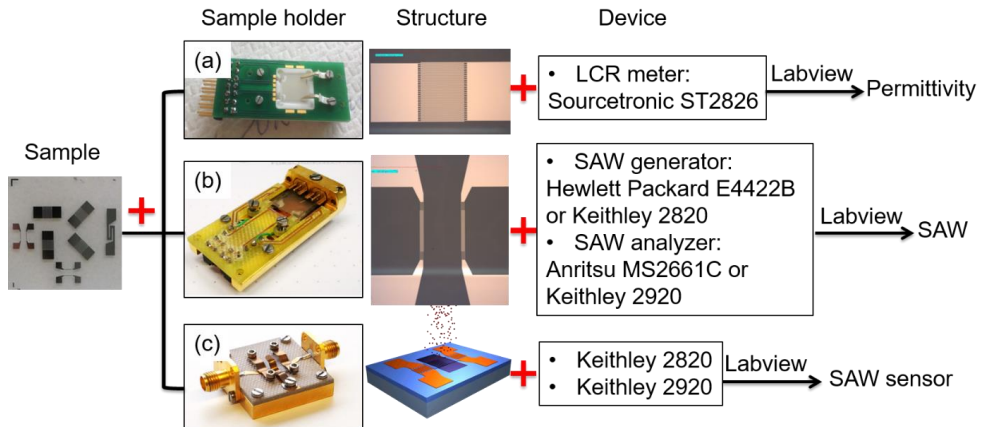


Figure 3.13. Sketch of the experimental devices for the measurements of permittivity, SAW and SAW sensor. For each type of characterization, a corresponding sample holder is designed to connect the sample with the external devices.

### 3.4.1 Temperature control

The temperature dependence of thin film properties is of great interest for electronic characterization. Therefore, the temperature has to be well controlled during the measurement. In this thesis, most of the temperature control is realized in a flow cryostat. Fig. 3.14 (a) shows an image of the cryostat setup. The sample is mounted onto the sample holder (see Fig. 3.14(c)), and then the sample holder is placed onto the sample stick (see Fig. 3.14(b)) for inserting the sample into the cryostat chamber.

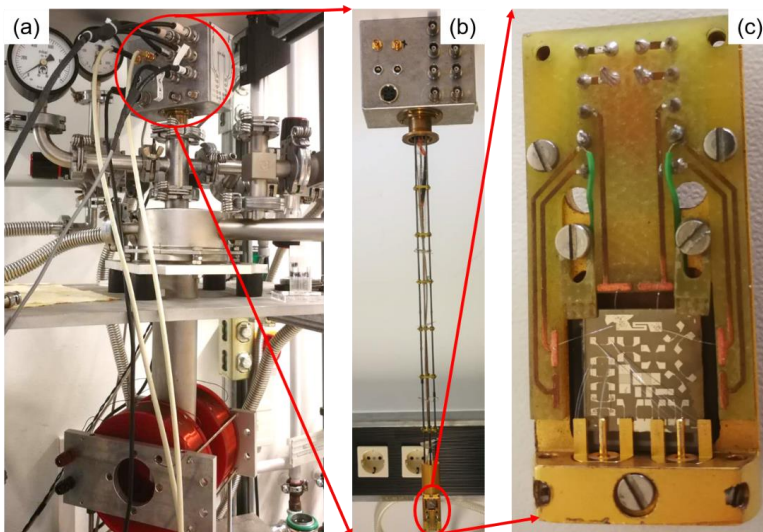


Figure 3.14. Images of the cryostat setup (a) an overview, (b) the sample stick that is inserted in the cryostat, (c) the permittivity sample holder that is plugged onto the sample stick.

The cooling down of the system is realized via liquid helium. The helium gas flow can be manually controlled to continuously cool the sample down. The heating of sample is realized via a self-made planar resistive heater, which is deposited by sputtering on the backside of a sapphire crystal. The input power of the heater and therefore the heating speed is controlled by a Lake Shore temperature controller. During the temperature control process, the temperature of the cryostat is recorded by an AuFe/Chromel thermocouple, whereas the local temperature of the sample is measured by an integrated Pt-temperature sensor, which is evaporated on the surface of the sample and calibrated by the cryostat temperature sensor.

The temperature control system can provide stable temperatures ranging from 4 K to 500 K, which meets the demands of our temperature-dependence measurements like permittivity and SAW.

### 3.4.2 Permittivity measurement

Fig. 3.15(a) shows a sketch of the designed IDEs for permittivity measurements. Here only a single pair of IDEs is shown. In practice, for anisotropy analysis, identical IDEs aligned along different directions are required. Fig. 3.15(b) shows an optical microscopy picture of the prepared IDE, which consists of 63 “fingers” with the width  $10\ \mu\text{m}$  and gap size  $5\ \mu\text{m}$ . The effective length of the fingers is  $700\ \mu\text{m}$ , the gap at the end of the fingers is extended to  $45\ \mu\text{m}$  to avoid the stray field, as shown in Fig. 3.15(c).

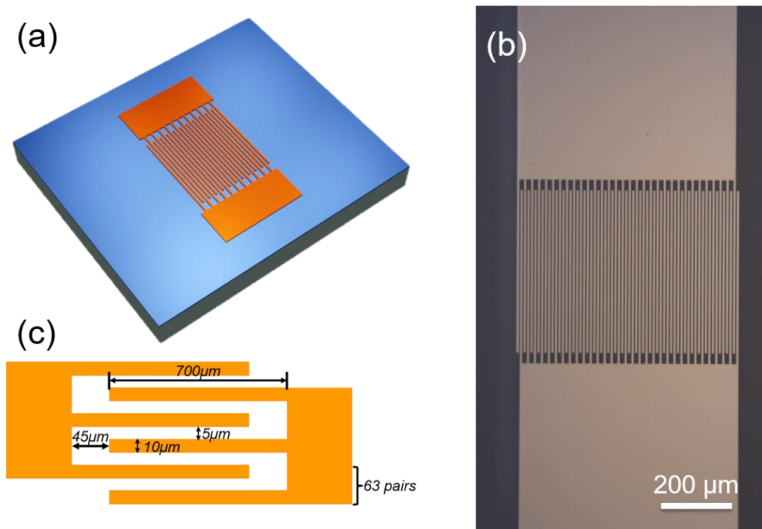


Figure 3.15. (a) Sketch of the design of the IDEs, (b) an optical microscopy picture of a prepared IDEs, (c) dimensions of the individual unit of the IDEs.

The IDE can be termed as a capacitor and the capacitance is determined by the permittivity of air, film and substrate. In practice, the capacitance of the IDE is measured by a LCR meter

(ST2826A) and the permittivity is then calculated from the capacitance by using the “partial capacitance model” [107-109].

The permittivity measurement is controlled and the data are recorded via a computer using LabVIEW program, which was programmed in cooperation with Prof. Roger Wördenweber. The typical interface is as shown in Fig. 3.16.

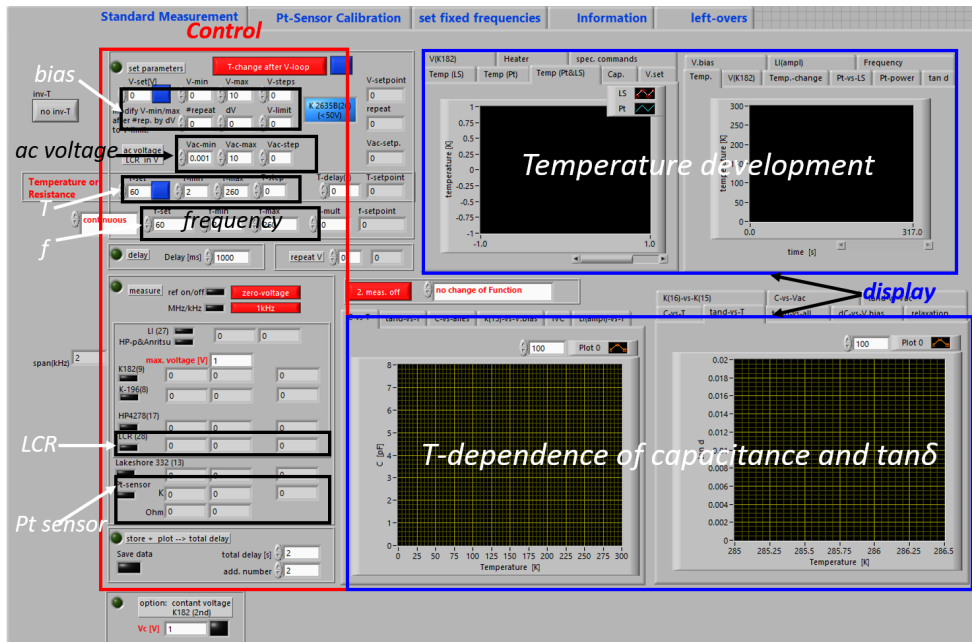


Fig. 3.16: Screenshot of the Labview control panel for the permittivity measurements. It basically consists of control (Temperature, ac voltage, frequency, bias etc.) and display (T-dependence of capacitance and loss, temperature development etc.) sections. The function of each section is marked in the figure.

The measured temperature, capacitance, and resulting permittivity is recorded, controlled, visualized and stored via the Labview program by the computer. Cooling and heating speed can also be manipulated by adjusting the parameters on the panel. This way continuous measurement over days (and nights) are possible.

### 3.4.3 Surface acoustic wave measurement

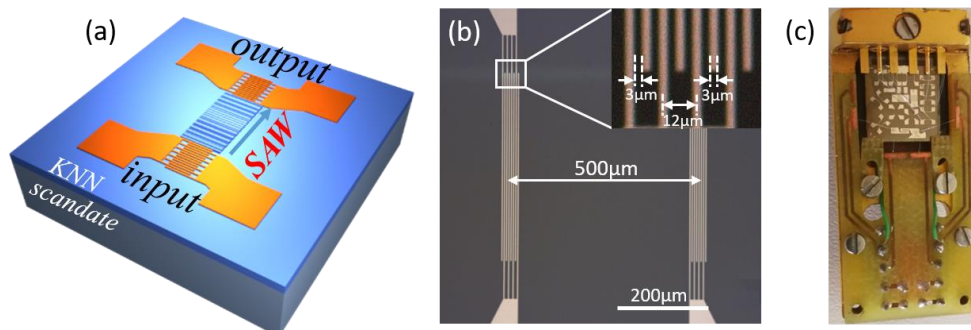


Figure 3.17. (a) Sketch of the design of IDTs on a thin KNN film surface, (b) dimensions of IDTs, and (c) sample carrier for SAW measurement.

Two identical IDTs are designed to generate (input) and detect (output) the SAW (see Fig. 3.17(a)), their operating mechanism has been introduced in chapter 2.3. Each IDT possess 4 pairs of fingers with 3  $\mu\text{m}$  width and gap size (see Fig. 3.17(b)), yielding a SAW wavelength of  $\lambda = 12 \mu\text{m}$  and effective length of 500  $\mu\text{m}$ . In most cases, the input-output distance (center-to-center) is  $L = 500 \mu\text{m}$  (see Fig. 3.17(b)). The sample is then mounted on the sample carrier for SAW characterization (see Fig. 3.17(c)). The input IDT is driven by an rf signal generator (HP E4422B or Keithley 2920A) in a frequency range from 50 MHz to 3 GHz with an input power of typically 0 dBm and a spectrum analyzer (Anritsu MS2661C or Keithley 2820A) is used to measure the SAW frequency response. The measurement process, including frequency range, scanning step, delay time, DC bias etc. is controlled by the LabVIEW program, as shown in Fig. 3.18.

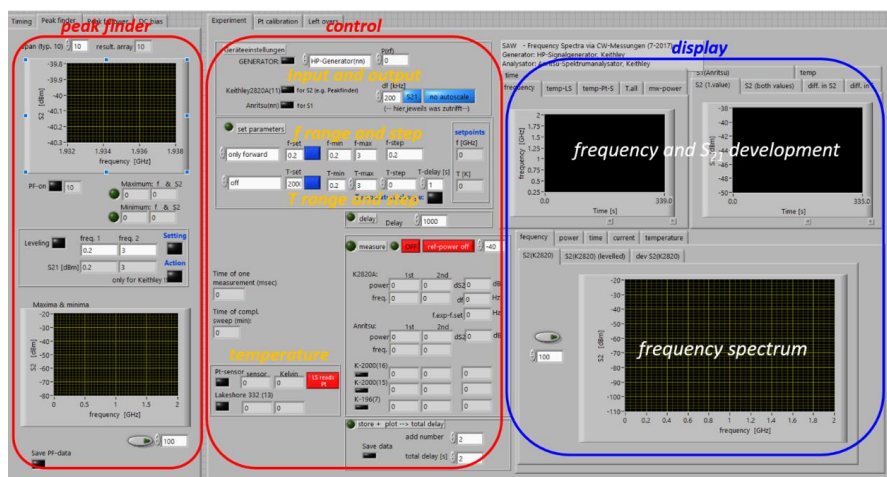


Figure 3.18. Screenshot of the control panel developed in Lab-view for the SAW measurements in this thesis.

The program allows to change all important parameters. Moreover, it is possible to monitor the measurement day and night. Additionally, temperature sensors and a heater can be used for cryogenic measurements. An implemented peak finder allows to automatically detect the interference peaks which are characteristic for the SAW signal and, thus, simplifies the SAW analysis.

### 3.4.4 Surface acoustic wave sensor

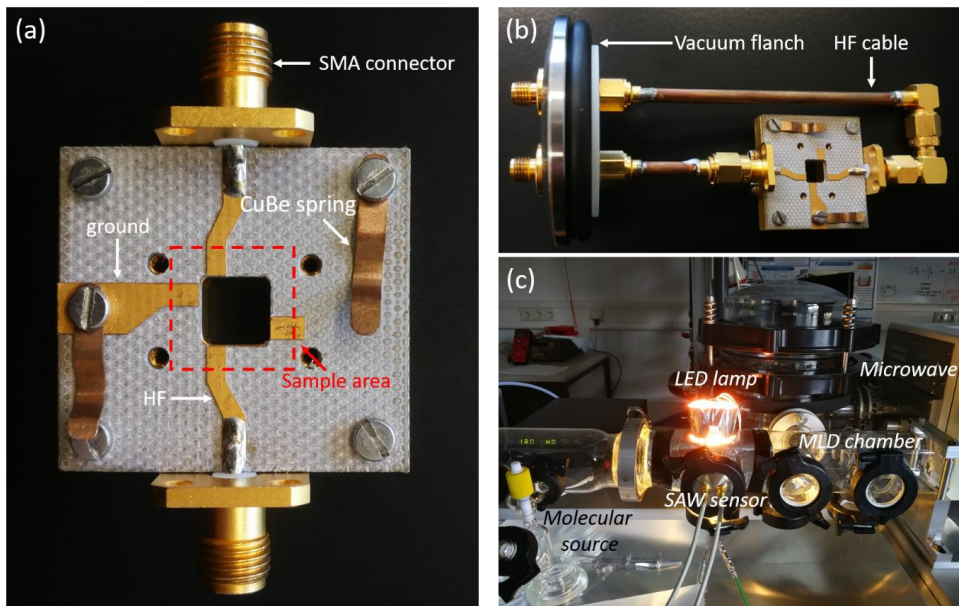


Figure 3.19. Images of the MLD compatible SAW device, (a) top side view of the sample holder, the CuBe springs are used to fix the sample, the SMA connectors are used to get access to HF signal, (b) sample holder mounted with a vacuum flange to get access to SAW generator and analyzer outside the MLD chamber, (c) SAW sensor mounted into MLD setup. (SAW sensor carrier designed in cooperation with Master student D. Finck [110] and built by the IBI-3 workshop of the FZJ)

In order to establish a SAW sensor system that is compatible with the MLD setup for in situ molecular deposition detection, a MLD compatible sample carrier was designed in cooperation with Master student D. Finck [110] and built by the IBI-3 workshop of the FZJ (see Fig. 3.19). The MLD-compatible sample carrier has a series of advantages:

- (i) allow access to high frequency signal,
- (ii) the surface are electroplated with Au to enhance the conductivity,
- (iii) the whole chip is organic-free, which will not introduce contamination to the chamber of the MLD setup,

- (iv) the sample can directly be fixed on the carrier by CuBe springs. As a result, the complex Al-wire bonding can be avoided, improving the stability and reproducibility of the SAW sensor system.

The sketch of MLD setup with integrated SAW sensor system and the operating recipe has been introduced in [chapter 3.1.4](#).

As mentioned in [chapter 2.3](#), the SAW sensor operation is typically realized based on measuring the shift of the center frequency during sensing. Therefore, it is of significant importance to monitor and record the change of the center frequency in real time. We established a Labview control system for in-situ molecular layer detection (see [Fig. 3.20](#)).

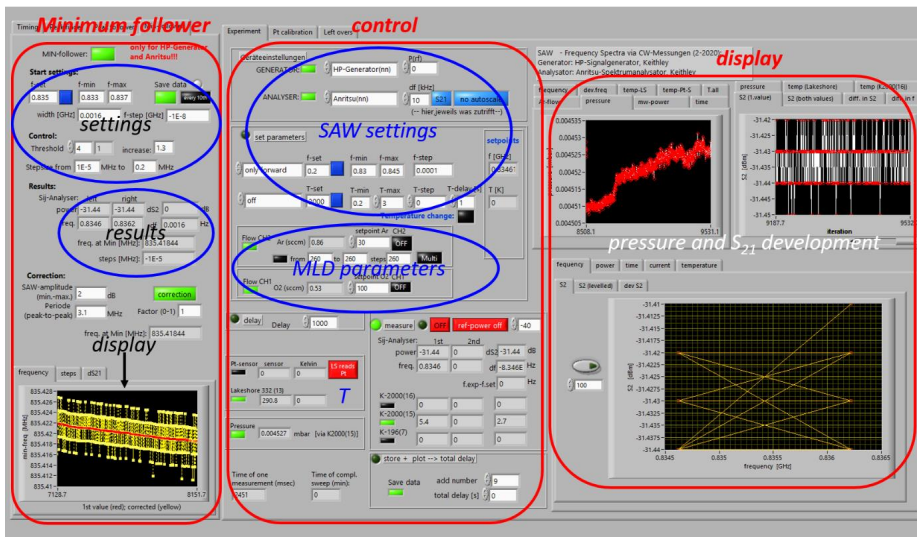


Figure 3.20. Labview control system for in-situ molecular layer detection. Units of the general SAW control, MLD setup parameters (gas flow/pressure) control and “minimum follower” for center frequency tracking are integrated in this Labview program.

This Labview program includes units of a general SAW measurement control, MLD setup control, and “minimum follower” module (see red frame on the left in [Fig. 3.20](#)), which allows an in situ detection of SAW frequency changes. The idea of the algorithm is based on analyzing the change of the interference pattern by tracking a sharp minimum within the interference pattern close to the resonance frequency (see [Fig. 3.21\(a\)](#)).

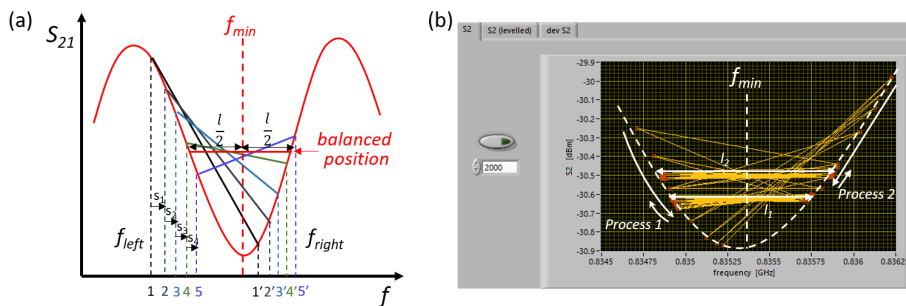


Figure 3.21. (a) Working principle of the “minimum follower” module, showing a series of subsequent steps (number 1 to 5) finding a minimum in a SAW spectrum by levelling two amplitudes  $S_{21}$  measured at frequencies  $\bar{f} - \frac{l}{2}$  and  $\bar{f} + \frac{l}{2}$ . (b) a real measurement of “minimum follower” program, two frequency distances  $l_1$  and  $l_2$  are tested to find the  $f_{min}$ .

The “minimum follower” module is a feedback control system that measures the transmission coefficient  $S_{21}$  for two frequencies  $f_{left} = \bar{f} - l/2$  and  $f_{right} = \bar{f} + l/2$ , where  $l$  is the distance between the left and right frequency. Picking a reasonable  $l$  value (e.g. half the period of the interference pattern), the program then tries to minimize the difference of  $S_{21}$  at  $f_{left}$  and  $f_{right}$ :

$$S_{21}(f_{right}) - S_{21}(f_{left}) = \Delta S_l \rightarrow 0 \quad (3.5)$$

Assuming a symmetric interference pattern, the frequency  $f_{min}$  of the minimum in  $S_{21}$  is then determined by:

$$f_{min} = \bar{f} = \frac{f_{left} + f_{right}}{2} (\Delta S_l \rightarrow 0) \quad (3.6)$$

The “minimum follower” typically starts with a nonzero  $\Delta S_l$  measurement and moves the measuring frequency stepwise in the direction of minimizing  $\Delta S_l$ . After several steps,  $\Delta S_l$  becomes smaller and smaller, i.e. closer and closer to zero. If  $\Delta S_l$  changes sign (e.g. from negative to positive), the direction of the step is inverted and reduced (typically to  $-s/2$ ) to further minimize the  $\Delta S_l$ . In the end, the measurement reaches to a balanced position and  $f_{min}$  is given by the average value of  $f_{left}$  and  $f_{right}$ . The parameters, e.g.  $l$  and  $s$ , can be adjusted by the user to optimize the control routine of the measurement.

Fig. 3.21(b) shows a real measurement of “minimum follower”. Two different frequency distances  $l_1$  and  $l_2$  were chosen to test the program (marked as process 1 and 2). As illustrated in Fig. 3.21(a), the frequency moves first forwards and then backwards (or on the contrary) to get to the balanced position. In the end, the two measurement processes point to the same  $f_{min}$ .

Finally, we expanded the program to record the shift of center frequencies at different harmonic. Accordingly, the Labview is further improved to enable simultaneous detection of frequency shift for 4 different harmonics, as shown in Fig. 3.22. The detailed measurements will be discussed in chapter 7.

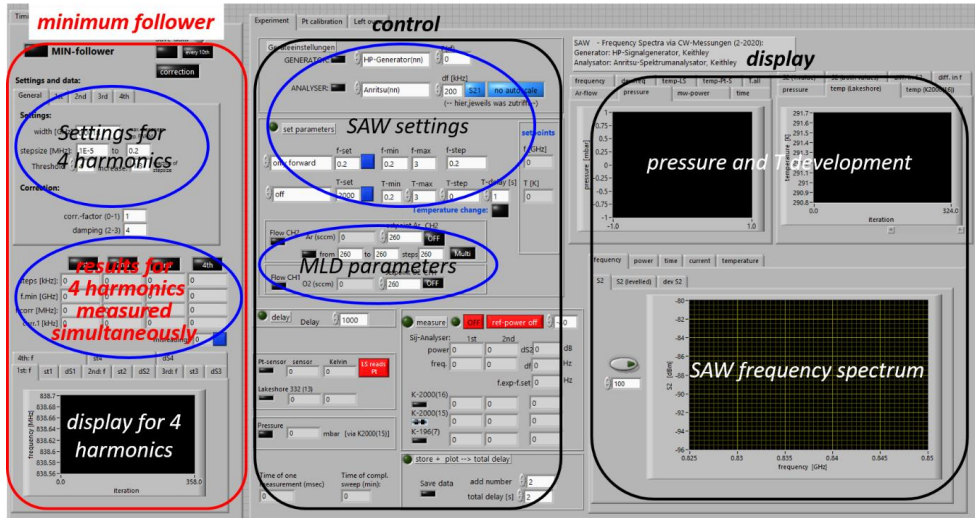


Fig. 3.22. Further improved Labview control system for in-situ molecular layer detection. The shift of frequency at 4 different harmonics can be detected simultaneously.

## 4 Strain engineering of the ferroelectric properties of $K_xNa_{1-x}NbO_3$ films

The ferroelectric properties of the epitaxially grown  $K_xNa_{1-x}NbO_3$  films on various scandate substrates are discussed in this chapter. Two methods—MOCVD and PLD—are applied to deposit  $K_xNa_{1-x}NbO_3$  thin films. The structural characterizations of MOCVD- and PLD-prepared samples are presented. The effects of strain on the phase transition temperature of  $K_xNa_{1-x}NbO_3$  thin films are investigated, structural and ferroelectric properties of MOCVD- and PLD-prepared samples are compared. Conventional and, alternatively, relaxor-type ferroelectric behavior is observed in MOCVD-prepared and PLD-prepared samples, respectively. Promising candidates are selected for SAW sensor applications.

### 4.1 Structure, strain, and stoichiometry

$K_xNa_{1-x}NbO_3$  thin films with a nominal composition of  $K_{0.7}Na_{0.3}NbO_3$  are deposited on various scandate substrates— $DyScO_3$  (DSO),  $TbScO_3$  (TSO),  $GdScO_3$  (GSO), and  $SmScO_3$  (SSO)—via MOCVD and PLD methods. The pseudocubic in-plane lattice parameters of unstrained  $K_{0.7}Na_{0.3}NbO_3$  and the different scandate substrates are compared in [table 4.1](#).

*Table 4.1: Pseudocubic in-plane lattice parameters of unstrained  $K_{0.7}Na_{0.3}NbO_3$  and the different scandate substrates as well as the resulting nominal strain of epitaxially grown KNN films for the different substrates. The lattice parameters given in brackets represent the averaged values used in the “square model” [50] for the evaluation of the strain of the films on the different substrate. (Data source from ref. [25, 127])*

Material	In-plane lattice parameter [Å]		Nominal strain [%]		
	$[001]_{pc}$	$[1\bar{1}0]_{pc}$	$[001]_{pc}$	$[1\bar{1}0]_{pc}$	
Substrate	$DyScO_3$	3.946	3.952	-1.20	-1.05
	$TbScO_3$	3.959	3.960	-0.88	-0.85
	$GdScO_3$	3.966	3.97	-0.70	-0.60
	$SmScO_3$	3.983	3.991	-0.28	-0.075
Film	$K_{0.7}Na_{0.3}NbO_3$	3.970 (3.994)	4.018 (3.994)	/	/

The pseudocubic in-plane lattice parameters of unstrained  $K_{0.7}Na_{0.3}NbO_3$  are calculated from pure perovskite  $KNbO_3$  and  $NaNbO_3$  signal crystals [96-100]. For the convenience of strain evaluation, a “square model” proposed by B. Cai et al [47,50] has been applied to identify the in-plane mismatch of epitaxially grown  $K_{0.7}Na_{0.3}NbO_3$  films. This model assumes that the epitaxial thin films initially form a square lattice on the substrates. Therefore, the in-plane lattice parameters can actually be given by the average of the nominal lattice parameters of  $[001]_{pc}$  (3.970Å) and  $[1\bar{1}0]_{pc}$  (4.018Å) orientations, i.e. 3.994Å. This lattice parameters based

on the square model have been used in this thesis to get an idea of the nominal strain introduced to the films due to the epitaxial growth (see [table 4.1](#), negative symbol indicates compressive strain).

The relationship between the in-plane lattice parameters of  $K_{0.7}Na_{0.3}NbO_3$  thin films and scandate substrates is schematically displayed in [Fig. 4.1](#). Since the lattice parameter of  $K_{0.7}Na_{0.3}NbO_3$  thin films is larger than that of the scandate substrates, a compressive in-plane strain will be introduced to the epitaxially grown films, which will be compensated by a tensile out-plane strain due to the Poisson effect (see the schematics of lattice in [Fig. 4.1](#)).

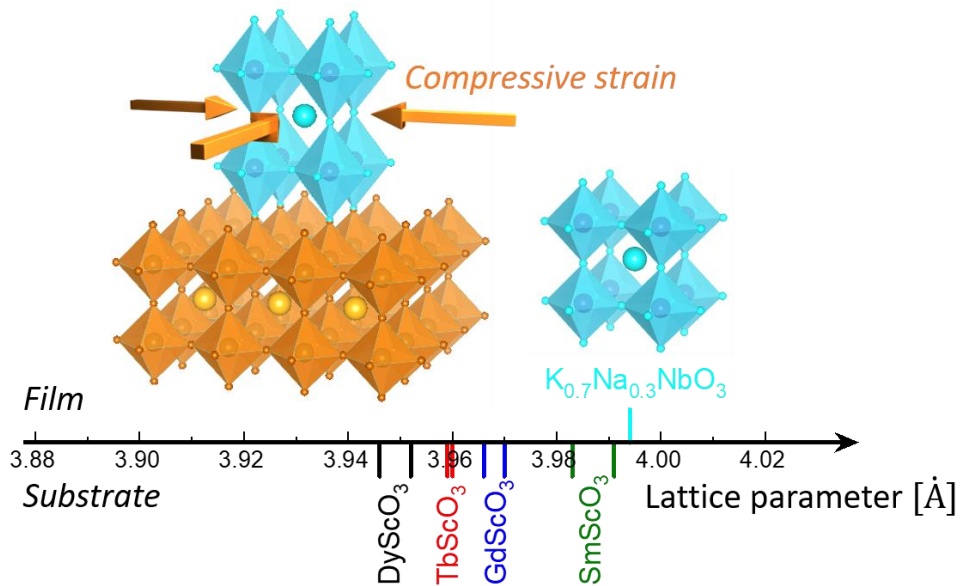


*Figure 4.1. Schematic of heteroepitaxy leading to an in-plane compressive strain and comparison of in-plane lattice parameters of  $K_{0.7}Na_{0.3}NbO_3$  thin films and various scandate substrates. Note that KNN films are represented by one in plane lattice parameter, whereas the scandates possess two different in plane lattice parameters.*

We investigated the epitaxial growth of KNN films via XRD experiments. The RSM measurements were performed by the IKZ in Berlin and then the data were analyzed and interpreted by me. [Fig. 4.2](#) shows RSM images of three MOCVD-prepared  $K_{0.7}Na_{0.3}NbO_3$  samples (47\_008 TSO, 47\_008 GSO, and 47\_008 SSO), as well as one PLD-prepared sample DP\_1303 TSO as examples which demonstrate the quality of the epitaxial growth. [Fig. 4.2 \(a\)](#), [\(b\)](#) and [\(c\)](#) represent the RSM data of MOCVD samples which were analyzed together with Yang Dai and also appear in his doctoral thesis [\[25\]](#). They are shown here to allow a systematic comparison with the PLD-prepared samples represented by [Fig. 4.2\(d\)](#). For each sample, the

RSMs are taken in the vicinity of the (620) and (444) Bragg reflections of the scandate substrates.

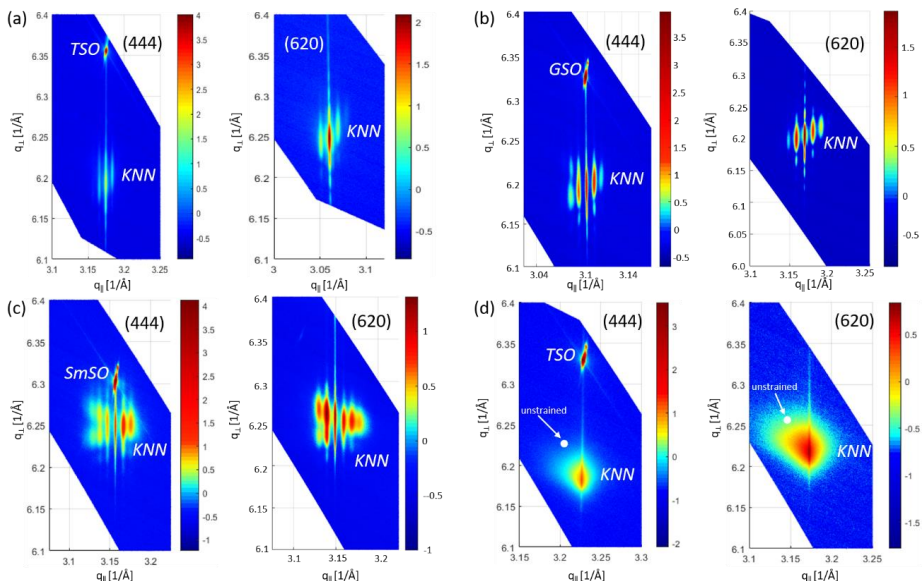


Figure 4.2. RSMs of MOCVD- and PLD-prepared samples in the vicinity of the (620) and (444) Bragg reflections of the scandate substrates. (a)  $K_{0.7}Na_{0.3}NbO_3$  on  $TbScO_3$  (MOCVD, 27 nm, 47\_008 TSO), (b)  $K_{0.7}Na_{0.3}NbO_3$  on  $GdScO_3$  (MOCVD, 27 nm, 47\_008 GSO), (c)  $K_{0.7}Na_{0.3}NbO_3$  on  $SmScO_3$  (MOCVD, 31 nm, 47\_008 SSO), (d)  $K_{0.7}Na_{0.3}NbO_3$  on  $TbScO_3$  (PLD, 27 nm, DP\_1303 TSO), the white dots mark the expected position of unstrained KNN. Note that, in some cases, the (620) Bragg reflections of the substrates lie outside the  $q_{\perp}$  scale. (Measurement L.v. Helden and D. Pfützenreuter, IKZ Berlin)

According to Fig. 4.2:

- (i) In case of MOCVD-prepared samples (Fig. 4.2(a), (b) and (c)), the agreement of the  $q_{\parallel}$  positions of the films and substrates indicates a perfect epitaxial growth with hardly any structural relaxation of the KNN thin films.
- (ii) The presence of satellite patterns in Fig. 4.2(a), (b) and (c) is indicative of a regular arrangement of ferroelectric domains, which is a clear indication of the ferroelectric state at RT in the films.
- (iii) In case of PLD-prepared samples (see Fig. 4.2(d)), the  $q_{\parallel}$  positions of the KNN is in agreement with the substrate reflections, confirming the epitaxial growth of the film. However, no satellite patterns are observed and the reflection is distorted in the direction of unstrained KNN (white dots in Fig. 4.2(d)), which are clear indications of a plastic relaxation. This leads to a relaxor-type ferroelectric which is discussed below in section 4.2.

- (iv) In both cases (MOCVD and PLD preparation), the resulting in-plane compressive strain is partially compensated by an out-of-plane tensile strain. Consequently, an increase of the out-of-plane lattice parameter,  $d_{\perp}$ , occurs. According to the RSM data, the  $d_{\perp}$  values of 47\_008 TSO, 47\_008 GSO, 47\_008 SSO, and DP\_1303 TSO samples are 4.057 Å, 4.044 Å, 4.017 Å, and 4.048 Å, respectively.

The composition of the  $K_xNa_{1-x}NbO_3$  samples is investigated via ToF-SIMS. The ToF-SIMS measurements were performed by Dr. Uwe Breuer (ZEA-3, FZJ), the data were analyzed by me. Fig. 4.3 shows two MOCVD-prepared samples (one on DyScO<sub>3</sub> and one on TbScO<sub>3</sub>), as well as two PLD-prepared samples (one on DyScO<sub>3</sub> and one on TbScO<sub>3</sub>) as examples to show the depth profile of the compositions of the  $K_xNa_{1-x}NbO_3$  films, given by the secondary ion intensity (Fig. 4.3(a), (c), (e), and (g)) and the intensity ratios of  $K^+/Na^+$ ,  $Nb^{5+}/K^+$ , and  $Nb^{5+}/Na^+$  (Fig. 4.3(b), (d), (f), and (h)). The experimental data shown in Fig. 4.3 demonstrate:

- (i) The dramatic decrease of ion intensity of  $K^+$ ,  $Na^+$ , and  $Nb^{5+}$ , which coincides with the dramatic increase of ion intensity of  $Tb^{3+}$ ,  $Dy^{3+}$ , and  $Sc^{3+}$  indicates the approach of the interface between  $K_xNa_{1-x}NbO_3$  film and scandate substrate. The values left to the dashed line represent the depth profile of the ~ 30 nm thick KNN films, whereas the right part of the data belongs to the composition of the substrate (i.e. Sc, Tb, and Dy).
- (ii) Using the ToF-SIMS calibration introduced in chapter 3.2.4, the K-Na composition  $x$  of the  $K_xNa_{1-x}NbO_3$  thin films calculated from the  $K^+/Na^+$  secondary ion intensity ratio are  $x = 0.55$  to  $0.64$ ,  $0.68$  to  $0.72$ ,  $0.66$ , and  $0.08$  for 47\_016 DSO, 41\_013 TSO, DP\_1345 DSO, and DP\_1353 TSO, respectively. This indicates that the actual composition  $x$  of the KNN films agrees reasonably with the nominal composition of  $x = 0.7$  and  $0.1$  for the first three and last one sample, respectively.
- (iii) According to the secondary ion intensity depth profile, the potassium is relatively homogeneous in the film, whereas the ion intensity of  $Na^+$  decreases with the depth, indicating an inhomogeneous Na distribution. This could be related to the volatility of Na during deposition and growth.

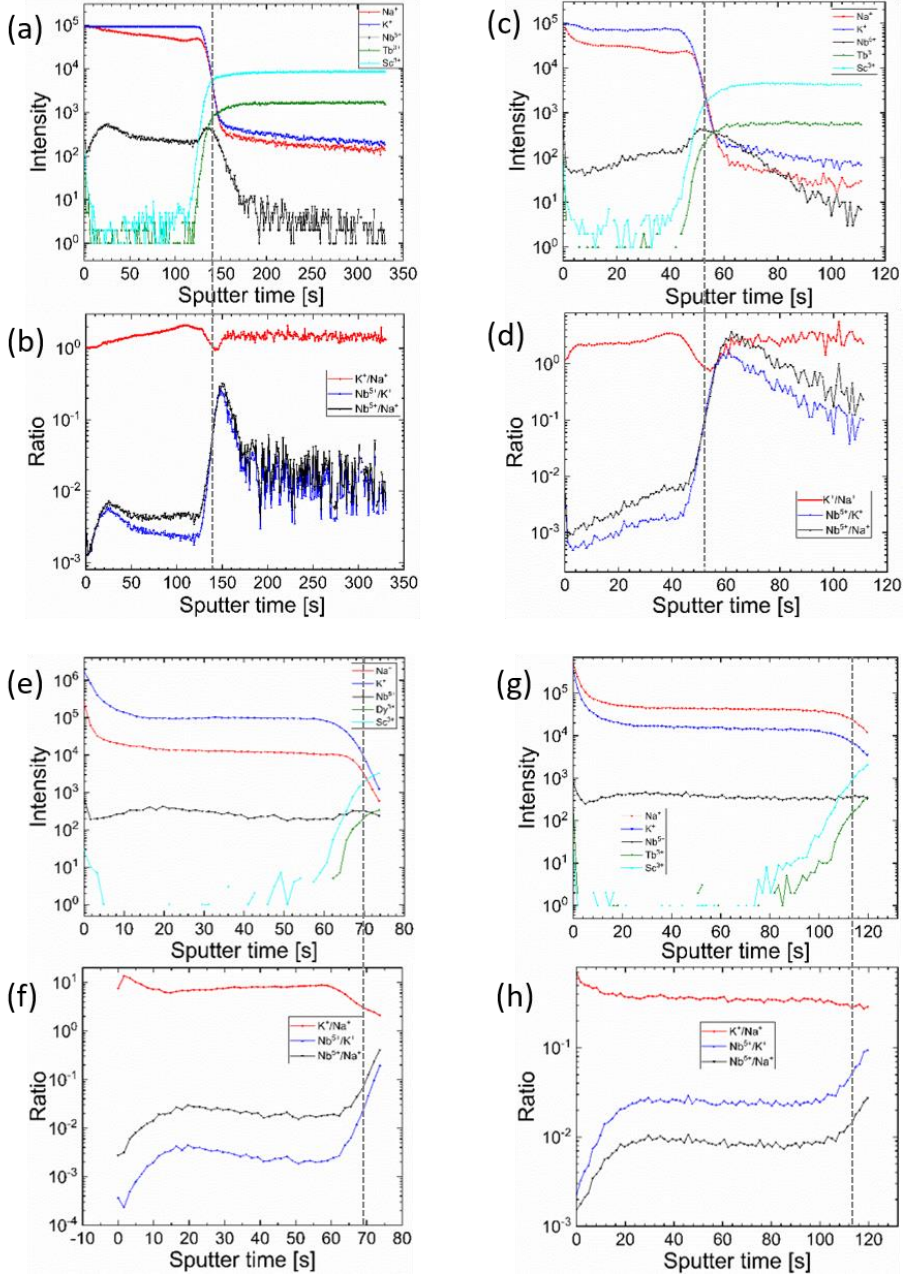


Figure 4.3. Secondary ion intensity ((a), (c), (e), and (g)) and intensity ratios of  $K^+/Na^+$ ,  $Nb^{5+}/K^+$ , and  $Nb^{5+}/Na^+$  ((b), (d), (f), and (h)) as function of sputter time, obtained from ToF-SIMS measurements. (a) and (b)  $K_{0.7}Na_{0.3}NbO_3$  on  $DyScO_3$  (MOCVD, 30 nm, 47\_016 DSO); (c) and (d)  $K_{0.7}Na_{0.3}NbO_3$  on  $TbScO_3$  (MOCVD, 47 nm, 41\_013 TSO); (e) and (f)  $K_{0.7}Na_{0.3}NbO_3$  on  $DyScO_3$  (PLD, 22 nm, DP\_1345 DSO); (g) and (h)  $K_{0.1}Na_{0.9}NbO_3$  on  $TbScO_3$  (PLD, 30 nm, DP\_1353 TSO). (Measurement: U. Breuer, Forschungszentrum Jülich)

## 4.2 Strain engineering of $T_C$

Strain can be used to modify the transition temperature,  $T_C$ , of a ferroelectric material as well as the type of ferroelectric behavior. Although this is not the main topic of this thesis, the impact of epitaxial strain on both properties of our KNN films will be discussed in this chapter. Moreover, due to its complex structure, the  $T_C$  suppression caused by the film-substrate lattice mismatch turns out to be more complex in our system compared to the  $T_C$  enhancement observed in cubic perovskites such as SrTiO<sub>3</sub> or BaTiO<sub>3</sub>. In a previous work [47,50], a “square model” has been proposed which allows an estimation of the averaged in plane strain in the film. In this work, we suggest an improved model which characterizes the strain by taking the out-of-plane lattice parameter, which is connected to the in-plane strain via the Poisson effect, as a measure for the in-plane strain. Both models are discussed in the following.

For simplicity, the  $T_C$  value is associated with the temperature of the maximum of the permittivity. Fig. 4.4 displays the temperature dependence of the real part of the dielectric constant for typical MOCVD- (Fig. 4.4(a)) and PLD-prepared (Fig. 4.4(b)) KNN films. For each sample, the permittivity has been measured along different orientations of the substrate, i.e. [001] (light-colored curves) and  $[1\bar{1}0]$  (dark-colored curves). The detailed information for each sample can be found in the sample list in Appendix. The analysis of the permittivity represents the standard method to obtain most of the properties of ferroelectric materials and is therefore vital to all our samples. Fig. 4.4 reveals a number of interesting aspects:

- (i) The phase transition temperature  $T_C$  (marked by arrows in Fig. 4.4) of the compressively strained films is shifted to lower temperatures compared with the original phase transition temperature  $T_C = 693$  K of unstrained KNN samples. Depending on the strain, the reduction of  $T_C$  is different. Due to the small strain, the phase transition temperature of MOCVD films on SmScO<sub>3</sub> is beyond the measurement limit of cryostat, thus no phase transition has been observed. The phase transition temperature of the MOCVD-prepared KNN films on TbScO<sub>3</sub> and GdScO<sub>3</sub> is shifted slightly higher than RT (325 to 340 K, see Fig. 4.4). For MOCVD-prepared KNN films on DyScO<sub>3</sub>, the phase transition temperature is shifted to 229.86 K, which is much lower than room temperature. As a consequence, we expect no ferroelectric behavior at room temperature for KNN on DyScO<sub>3</sub>, whereas all other MOCVD films should be suitable for room temperature SAW experiments. However, most likely the films on TbScO<sub>3</sub> and GdScO<sub>3</sub> should be the best candidates since the transition temperature is closer to room temperature.
- (ii) In the case of the PLD films (Fig. 4.4(b)), the transition is much broader and the maximum in the permittivity is lower and shifted to lower temperatures compared to the MOCVD counterparts. This difference is correlated to the structural properties and will be discussed later in this subchapter.

- (iii) It is interesting to note that the maximum permittivity and RT permittivity can be enhanced via strain. While unstrained KNN shows  $\epsilon'_{max} \approx 6400$  and  $\epsilon'_{RT} \approx 600$  for  $x = 0.5$  (see Fig. 2.26), our films reach  $\epsilon'_{max} = 13695$  and  $\epsilon'_{RT} = 5166$  for  $x = 0.7$ .
- (iv) The permittivity of the sample turns out to be anisotropic. It differs for different orientations of the electric field. The ratio of maximum permittivity,  $\epsilon'_{[1\bar{1}0]}/\epsilon'_{[001]}$ , is 1.33 and 1.25 for 47\_008 TSO and 47\_008 GSO samples, respectively.
- (v) The peak of the permittivity in PLD-prepared samples is much broader than that of MOCVD-prepared samples. In general, a broad and frequency dispersive phase transition is a feature of typical relaxor-type ferroelectrics. It implies that the properties of MOCVD-prepared samples are closer to conventional ferroelectrics, while that of PLD-prepared samples are more close to relaxor-type ferroelectrics. The comparison between PLD- and MOCVD-prepared samples and the behavior of relaxor ferroelectrics will be discussed in detail later on.

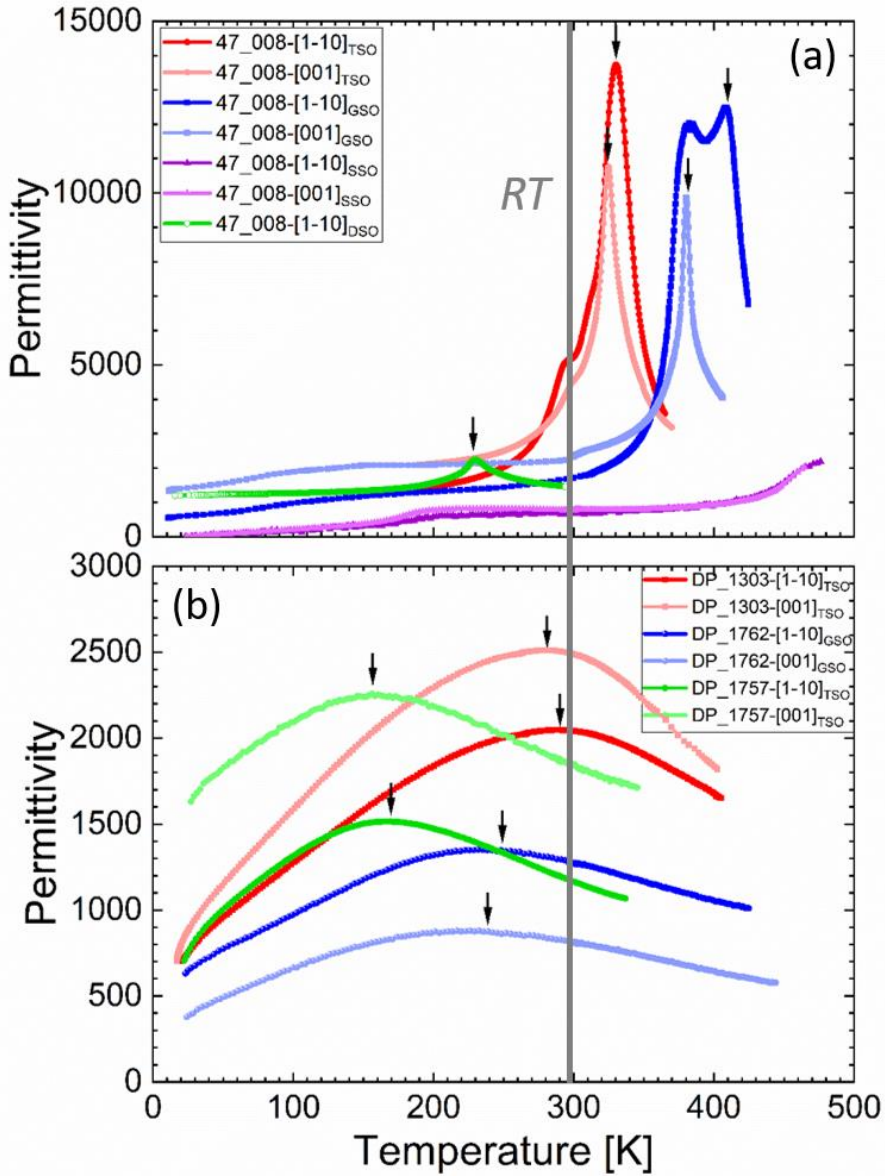


Figure 4.4. Temperature dependence of permittivity for (a) MOCVD-prepared samples, and (b) PLD-prepared samples. For each sample, the permittivity along two different orientations of the substrate has been measured, i.e.  $[1\bar{1}0]$  (dark curves) and  $[001]$  (light curves). The position of room temperature (RT) is marked by the gray line.

The strain-dependent shift of the phase transition temperature  $\Delta T_C$  in terms of the “square model” is shown in Fig. 4.5. The phase transition temperatures are extracted from Fig. 4.4, the colorful symbols represent the MOCVD samples, while the black symbols represent the PLD samples.

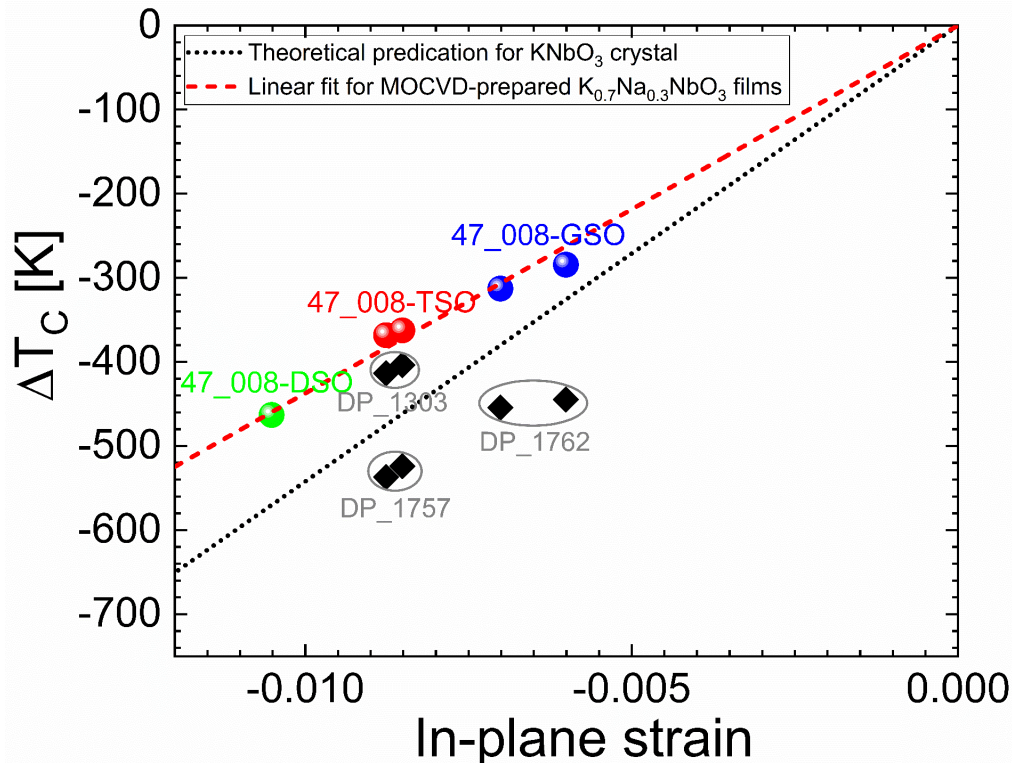


Figure 4.5. Shift of the phase transition temperature as function of strain calculated according to the “square model” [50] for MOCVD- and PLD-prepared  $K_{0.7}Na_{0.3}NbO_3$  films on (110)-orientated  $DyScO_3$ ,  $TbScO_3$  and  $GdScO_3$  substrates. The phase transition temperatures are extracted from Fig. 4.4. The dash red line is the linear fit of  $\Delta T_C$  for the MOCVD samples, the dot black line represents the theoretical prediction of  $\Delta T_C$  for  $KNbO_3$  crystal using eq. (2.14).

Approximating the properties of the films by using the material parameters of  $KNbO_3$  crystals [25], a theoretical prediction of the shift of phase transition temperatures can be obtained via eq. (2.13). The resulting theoretical prediction is shown in Fig. 4.5.

A glimpse on the data points in Fig. 4.5 shows that the shift of  $T_C$  of MOCVD samples are likely to depend linearly on the in-plane compressive strain. Moreover, the linear fit meet the origin at  $\Delta T_C(\epsilon = 0) = 0$  K. The perfect linearity is shown in Fig. 4.5 (dash red line). Considering the slight difference in material parameters for  $K_{0.7}Na_{0.3}NbO_3$  and  $KNbO_3$ , the experimental results seem to be in good agreement with the theoretical prediction.

The data points of the PLD samples show no clear dependence. Nevertheless, although the  $T_C$  values scatter and are generally below the MOCVD data, they still agree reasonably with the theoretical predication, especially taking into account that determination of  $T_C$  is ambiguous considering the broadness of the peak in the permittivity (Fig. 4.4(b)).

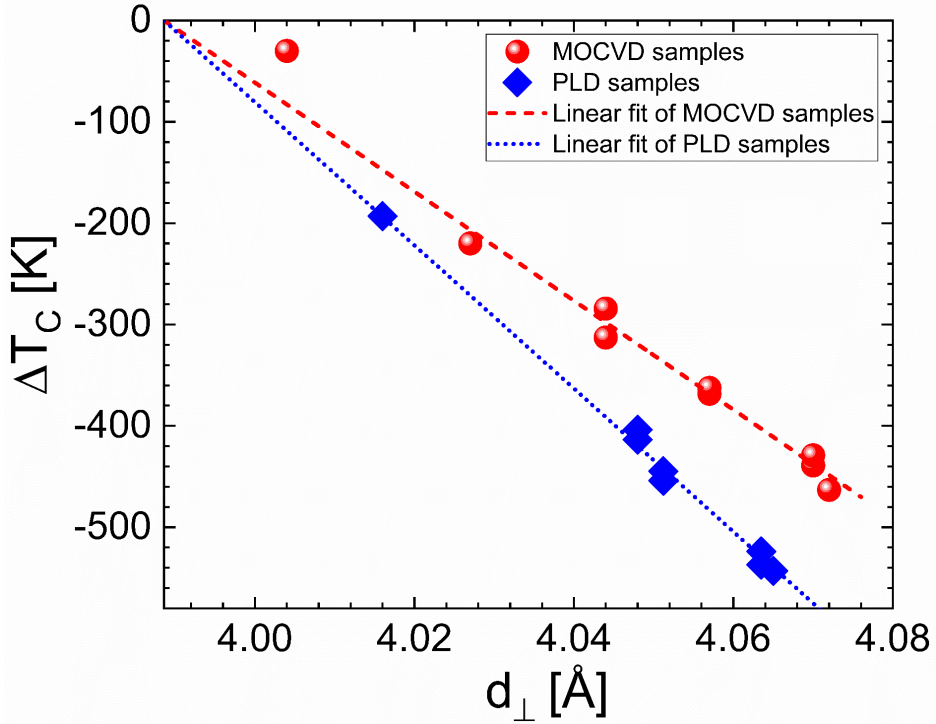


Figure 4.6. Shift of phase transition temperature as function of vertical lattice parameter for MOCVD- and PLD-prepared  $K_{0.7}Na_{0.3}NbO_3$  films on (110)-orientated  $DyScO_3$ ,  $TbScO_3$  and  $GdScO_3$  substrates. The red dashed line is the linear fit of  $\Delta T_C$  for the MOCVD samples, the blue dotted line represents the linear fit of  $\Delta T_C$  for PLD samples.

In order to improve the model, we use the normal lattice parameters  $d_{\perp}$  of the KNN thin films in this thesis to qualitatively evaluate the strain and its impact on  $T_C$  in the epitaxial KNN films. The normal lattice parameters are measured by HRXRD (see chapter 2.2). Due to the Poisson effect, the in plane compressive strain is compensated by a corresponding out-of-plane tensile strain. As a result, the normal lattice parameter increases with the compressive in plane strain. In this way, the normal lattice parameter reflects the actual in-plane strain in a better way compared to the “square model”.

Fig. 4.6 shows the shift of  $T_C$  as function of the vertical lattice parameter for MOCVD- (red data points) and PLD-prepared (blue data points)  $K_{0.7}Na_{0.3}NbO_3$  films on (110)-orientated  $DyScO_3$ ,  $TbScO_3$  and  $GdScO_3$  substrates. In this approach, the data points of MOCVD and PLD samples can be fitted linearly with the origin  $\Delta T_C = 0$  at the out-of-plane lattice parameter of unstrained KNN. The fact that we obtain a perfect linear dependence for both preparation methods supports the use of this new “normal lattice model” (NLM) for the description of the  $T_C$  dependence on the strain. Moreover, since the out-of-plane lattice parameter can easily be determined, it might represent a useful tool to predict the  $T_C$  values of strained films in general.

The slopes of the linear fits are different between PLD samples and MOCVD samples. This indicates that the KNN films prepared by PLD and MOCVD possess different properties. For example, the defect density, homogeneity, elastic modulus, or electrostrictive coefficient might be different for the two deposition methods. This is also visible in the shape of the transition which is discussed in the following part.

### 4.3 Strained conventional and relaxor-type ferroelectrics

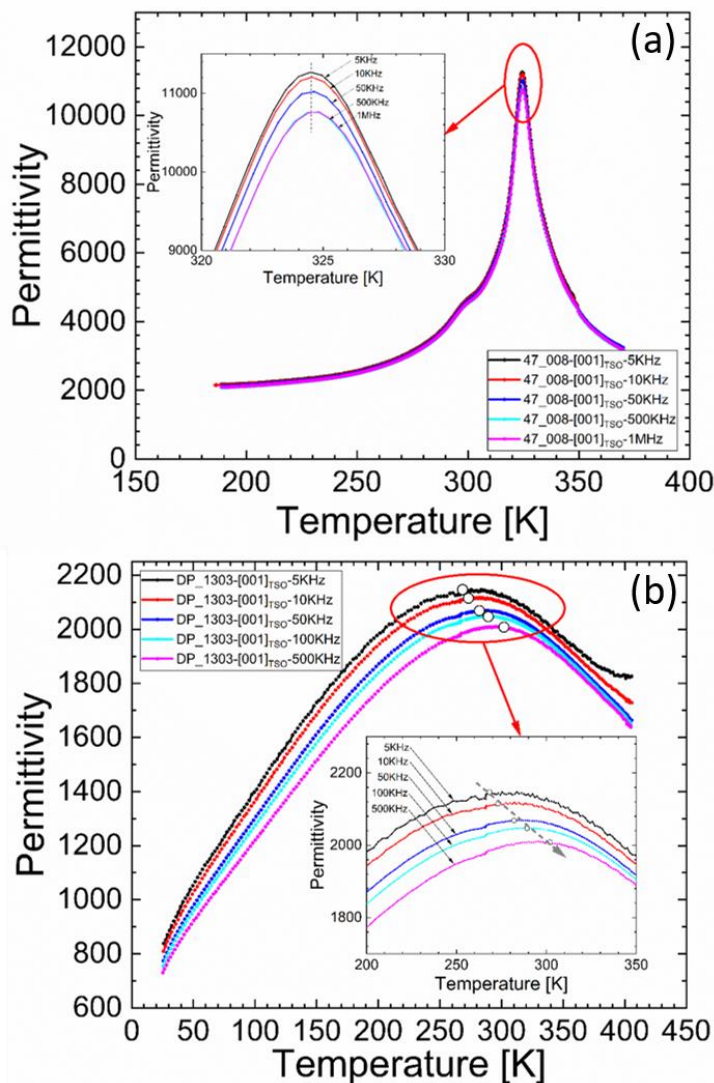


Figure 4.7. Temperature dependence of the permittivity at various frequencies for (a) MOCVD-prepared 47\_008 TSO (27 nm  $K_{0.7}Na_{0.3}NbO_3$  on (110)-oriented  $TbScO_3$ ) and (b) PLD prepared DP\_1303 TSO (25 nm  $K_{0.7}Na_{0.3}NbO_3$  on (110)-oriented  $TbScO_3$ ). The insets zoom in the regions of the maximum permittivity.

As shown already in Fig. 4.4, the broad permittivity peak of PLD-prepared KNN films implies a behavior more approximate to relaxor-type ferroelectrics, while the sharp permittivity peak of MOCVD-prepared KNN films indicates a behavior closer to conventional ferroelectrics. To analyze the different ferroelectric behaviors of MOCVD and PLD samples, the frequency

dispersion of the temperature dependence of the permittivity is measured. Fig. 4.7 shows the data obtained for 47\_008 TSO and DP\_1303 TSO. It indicates that the permittivity of the MOCVD sample almost overlapped for different frequencies. The inset in Fig. 4.7 (a) is a zoom of the regime of maximum permittivity, the gray dash line marks the position of temperature  $T_{max}$  of maximum permittivity. It can be seen that  $T_{max}$  almost does not disperse as the frequency changes, indicating that the transition is frequency independent and that clustering of dipoles (e.g. in form of PNRs, see chapter 2.2.3) cannot be seen. In contrast, the PLD sample (Fig. 4.7(b)) shows a broad and especially frequency dispersive phase transition. The gray arrow in the inset of Fig. 4.7(b) indicates that  $T_{max}$  tends to increase with the frequency. The frequency dispersion of  $T_{max}$  is a clear indication of clustering of dipoles (most likely PNRs) which leads to a reduced mobility of the dipole orientation in the applied AC field. The frequency dependence of  $T_{max}$  agrees with the Vogel-Fulcher behavior [112,113], which will be discussed in detail in chapter 6. Here we restrain the discussion on the broadness of the transition which is described by the Lorentz simulation [114]:

$$\frac{\varepsilon'_{max}}{\varepsilon'} - 1 = \frac{(T - T_{max})^\gamma}{2\sigma^2} \quad (4.1)$$

for  $T > T_{max}$  with  $\gamma$  representing the degree of the dielectric relaxation and  $\sigma$  denoting the degree of the diffuseness of the phase transition. The sharp transition peak of conventional ferroelectrics is described by  $\gamma = 1$ , whereas a relaxor-type phase transition is usually given by  $\gamma = 1.5 - 2$ .

Rewriting Eq. 4.1 by:

$$\ln\left(\frac{\varepsilon'_{max} - \varepsilon'}{\varepsilon'}\right) = \gamma \ln(T - T_{max}) - \ln 2\sigma^2 \quad (4.2)$$

shows that the normalized permittivity (left part of eq. (4.2)) should show a linear temperature dependence in a double logarithmic plot of  $\ln[(\varepsilon'_{max} - \varepsilon')/\varepsilon']$  versus  $\ln(T - T_{max})$ . The slope of this plot provides the value  $\gamma$ , the intercept gives the value  $\sigma$ .

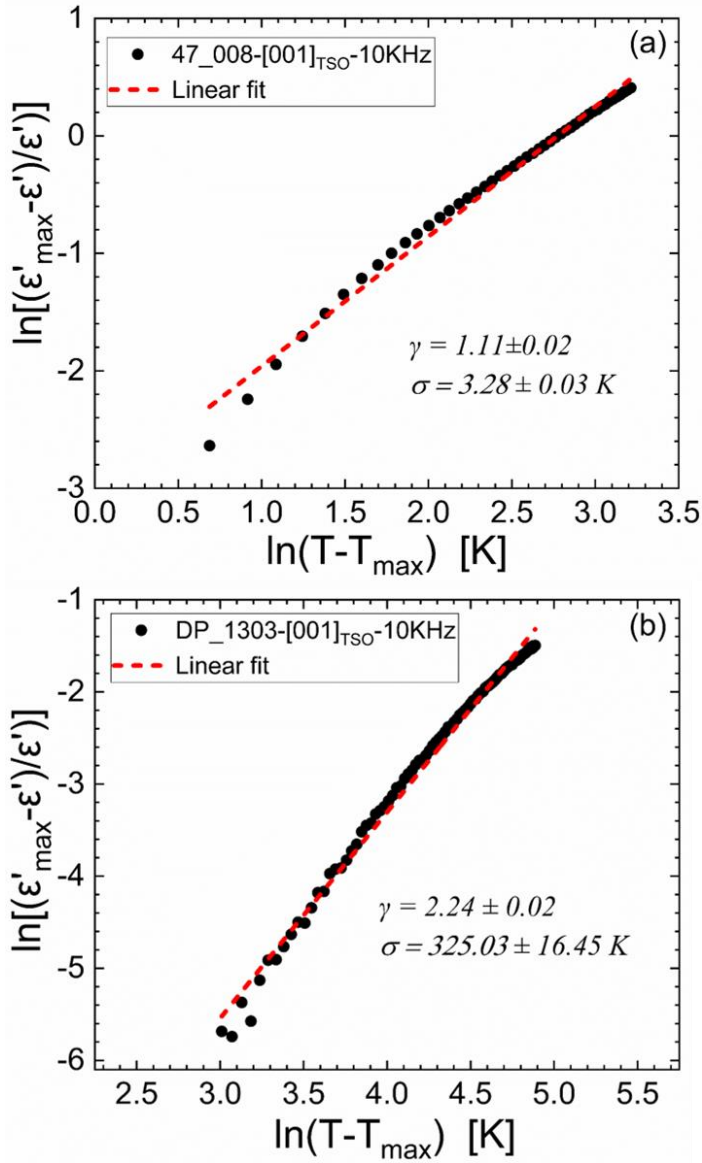


Figure 4.8. Lorentz fit of the permittivity measured at 10 KHz for (a) MOCVD-prepared 47\_008 TSO (27 nm  $K_{0.7}Na_{0.3}NbO_3$  on (110)-oriented  $TbScO_3$ ) and (b) PLD prepared DP\_1303 TSO (25 nm  $K_{0.7}Na_{0.3}NbO_3$  on (110)-oriented  $TbScO_3$ ).

The Lorentz fits (Fig. 4.8) provide a  $\gamma$  value of  $1.1 \pm 0.02$  for the MOCVD sample, whereas a  $\gamma$  value of  $2.24 \pm 0.02$  is obtained for the PLD sample. This supports the assumption that the MOCVD samples are very close to conventional ferroelectrics, whereas the PLD samples are closer to relaxor-type ferroelectrics. As introduced in chapter 2.2, the generation of relaxor-

type ferroelectrics is generally a result of microscopic composition inhomogeneity that leads to the so-called polar nanoregions (PNR). The high energy deposition of PLD makes it more likely to yield films with microscopic composition inhomogeneities, thus relaxor-type ferroelectrics can be expected for this deposition technique. In contrast, MOCVD represents a deposition technique known for its low particle energy. The resulting films are generally more homogeneous and possess less defect, which seems to allow a PNR-free ferroelectric state even though the films are heavily strained. This is a remarkable result. Therefore, from now on the films prepared by MOCVD will be termed as conventional ferroelectric, whereas the PLD samples will be considered as relaxor-type ferroelectric. The SAW properties of conventional and relaxor-type ferroelectrics will be discussed separately in [chapter 5](#) and [chapter 6](#).

Considering our aim of room temperature SAW applications, a strong SAW signal, i.e. a strong piezoelectricity of the samples at RT, is necessary. It will be shown in [chapter 5](#) that the temperature dependence of the SAW signal corresponds to the temperature dependence of the permittivity. Since the maximum of piezoelectricity appears close to the phase transition temperature, samples with  $T_C$  values slightly higher than RT should be ideal candidates. Therefore, the MOCVD samples 47\_008 TSO and 47\_008 GSO with phase transition temperatures in the range of 324 to 408 K ([Fig. 4.4](#)) are considered to be promising candidates for SAW applications at RT.

## 4.4 Summary

In this chapter, KNN films prepared via MOCVD and PLD are characterized. Their epitaxial growth, composition, and the strain dependence of  $T_C$  are discussed and compared for MOCVD and PLD samples. The main results are:

- (i) The MOCVD-prepared KNN samples show a perfect epitaxial growth with hardly any structural relaxation. In contrast, the PLD-prepared samples also show perfect epitaxy, however, an onset of plastic relaxation is observed. As a consequence, the MOCVD samples exhibit a typical conventional ferroelectric behavior with hardly any frequency dispersion of the ferroelectric phase transition, whereas the PLD samples show a broad and frequency dispersive ferroelectric phase transition.
- (ii) The phase transition temperatures  $T_C$  of MOCVD and PLD samples are shifted to lower temperatures by the compressive epitaxial strain. The known “square model” is used for the first analysis of the strain dependence of the shift of  $T_C$ . The MOCVD samples show a perfect linearity of  $\Delta T_C$  vs strain. However, the PLD samples show no clear dependence. In order to improve the model, a “normal lattice model” (NLM) is proposed to evaluate the strain dependence of  $\Delta T_C$ . The new model is based on the Poisson effect, the strain is represented by the vertical lattice parameter  $d_L$  of the KNN film. In this model,  $\Delta T_C$  vs  $d_L$  of MOCVD and PLD samples show a perfect linearity with slightly different slopes, which supports the use of the new model for the description of the strain dependence of the phase transition temperature.
- (iii) The dielectric properties of KNN films are highly improved by the strain, e.g. a maximum permittivity of  $\epsilon'_{max} \approx 13695$  at  $\sim 330$  K and a RT permittivity of  $\epsilon'_{RT} \approx 5166$  are achieved for a 27 nm-thick  $K_{0.7}Na_{0.3}NbO_3$  film on TSO prepared by MOCVD compared to  $\epsilon'_{max} \approx 6400$  and  $\epsilon'_{RT} \approx 600$  for unstrained KNN. Moreover, the dielectric properties turn out to be anisotropic. The permittivity along  $[1\bar{1}0]$  and  $[001]$  directions of the substrate show a ratio of  $\epsilon'_{[1\bar{1}0]}/\epsilon'_{[001]} = 1.33$  and 1.25 for the MOCVD films on TSO and GSO.

In the following chapter the SAW properties of MOCVD and PLD samples will be discussed.

## 5 SAW properties in conventional ferroelectric (K,Na)NbO<sub>3</sub>

The SAW properties of the MOCVD-prepared samples will be discussed in this chapter. In [chapter 4.2](#) we showed that the phase transition temperature of MOCVD-prepared samples can be shifted to around room temperature via compressive strain. In contrast to the relaxor-type ferroelectric behavior, which will be discussed in [chapter 6](#), they showed the typical behavior of conventional ferroelectrics. The SAW properties of these “conventional” ferroelectric (K,Na)NbO<sub>3</sub> films, including the SAW velocity, intensity, and generation of harmonics will be discussed in this chapter.

This chapter is based on our publication [[111](#)]: **S. Liang**, Y. Dai, L. von Helden, J. Schwarzkopf, R. Wördenweber, *Appl. Phys. Lett.* **113**, 052901 (2018).

### 5.1 SAW properties at room temperature

Let us start with the SAW properties of MOCVD samples at RT which includes the generation of harmonics, the anisotropy, and the effect of strain on SAW intensity.

As demonstrated in [chapter 4.2](#), the phase transition temperature of MOCVD-prepared samples has been shifted to temperatures slightly higher than RT, the MOCVD samples on TbScO<sub>3</sub> (47\_008 TSO) and GdScO<sub>3</sub> (47\_008 GSO) are used to analyze the SAW properties at room temperature.

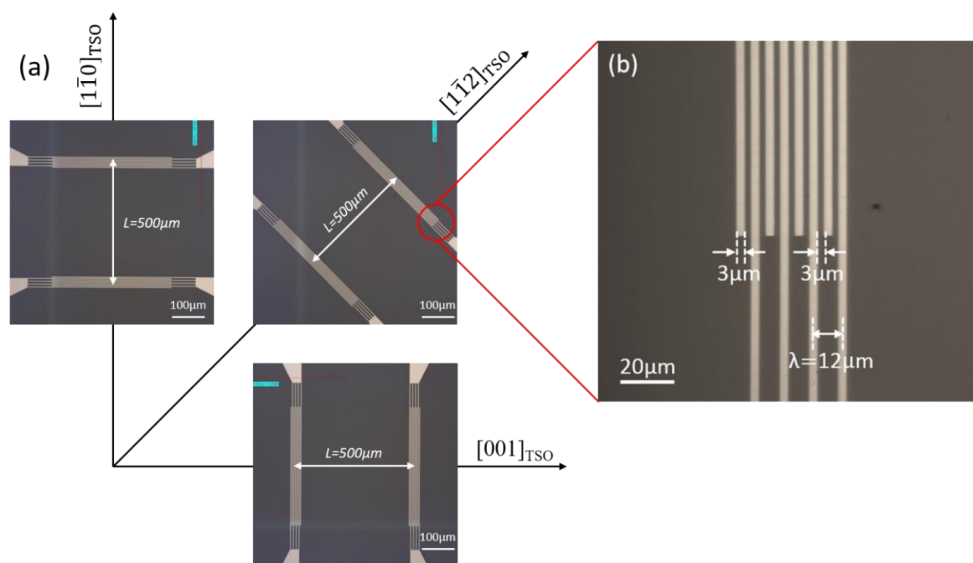


Figure 5.1. (a) Layout and (b) enlarged image of the IDTs on the  $K_{0.7}Na_{0.3}NbO_3$  for the SAW experiments. The crystalline orientation of the different IDTs with respect to the (110)-oriented substrate (here TbScO<sub>3</sub>) and the important design parameters  $L = 500 \mu\text{m}$  (distance between input and output IDTs), spacing and width of the electrodes ( $3 \mu\text{m}$ ), and the resulting wavelength  $\lambda = 12 \mu\text{m}$  are added.

For the SAW characterization of the films, interdigital transducers (IDT) are fabricated by means of electron-beam lithography, metallization, and lift-off technique (see [chapter 3.1](#) and [3.3](#)), resulting in electrodes of a 5 nm-thick adhesion layer of Ti and a 45 nm-thick layer of Pt. The layout and orientation of the IDTs for the surface acoustic wave experiments are shown in [Fig. 5.1](#).

The complete device consists of a generator IDT (input) and an analyzer IDT (output) with identical structures, i.e. 4 finger pairs with 3  $\mu\text{m}$  width and gap size (as shown in [Fig. 5.1\(b\)](#)), yielding a SAW wavelength of  $\lambda = 12 \mu\text{m}$ , an effective (free) finger length of 500  $\mu\text{m}$  and a propagation distance for the SAWs (center-to-center distance between generator and analyzer) of  $L = 500 \mu\text{m}$  (see [Fig. 5.1\(a\)](#)), the arrows of the orientations indicate the propagation direction of SAW). The input IDT is driven by a rf signal generator (HP E4422B or Keithley 2920A) in a frequency range from 50 MHz to 3 GHz with an input power of typically 0 dBm and a spectrum analyzer (Anritsu MS2661C or Keithley 2820A) is used to measure the SAW frequency response.

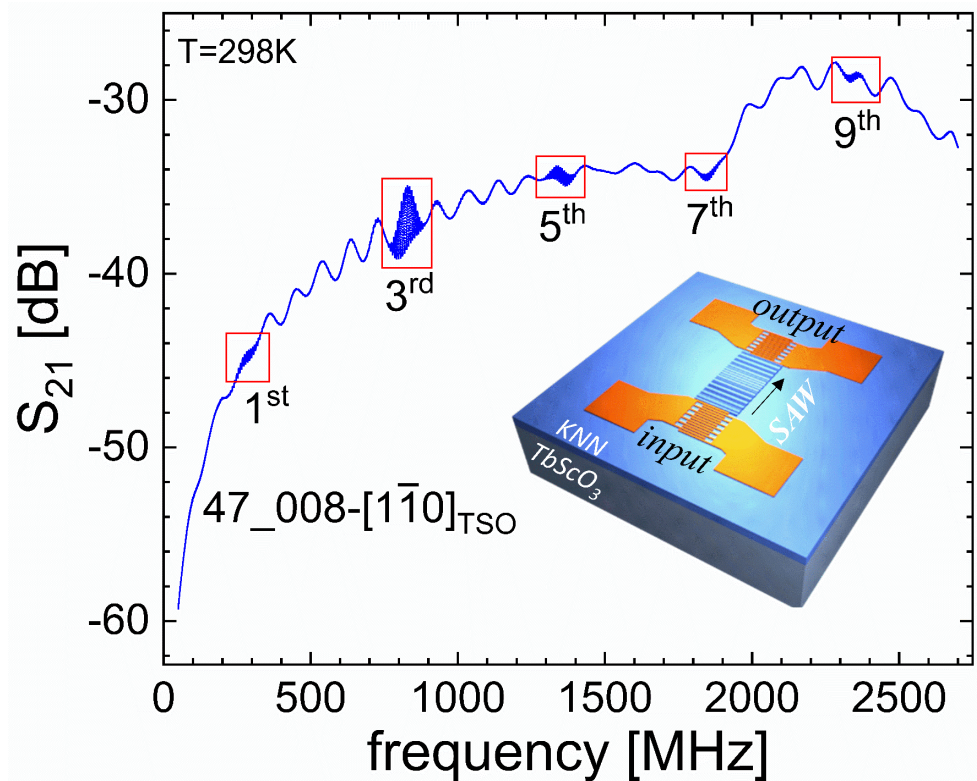


Figure 5.2: Frequency dependence of the transmission signal of a SAW structure, where  $\lambda=12 \mu\text{m}$  and  $L=500 \mu\text{m}$  (see [Fig. 5.1](#)), on a 27 nm-thick  $K_{0.7}Na_{0.3}NbO_3$  film on (110)  $TbScO_3$  (47\_008 TSO) measured at room temperature, which exhibits SAW signals for the odd harmonics marked from 1<sup>st</sup> to 9<sup>th</sup> for the small-strain direction  $[1\bar{1}0]_{\text{TSO}}$ . The schematic illustrates the generation, propagation, and detection of the SAW.

Fig. 5.2 summarizes the SAW data obtained at room temperature for a 27 nm-thick  $\text{K}_{0.7}\text{Na}_{0.3}\text{NbO}_3$  film on  $\text{TbScO}_3$  (47\_008 TSO). The schematic illustrates the generation, propagation, and detection of the SAW on KNN film. A complete frequency scan of the response of the interdigital transducers oriented along the  $[1\bar{1}0]_{\text{TSO}}$  direction is shown in the main plot. In general, the signal received by the IDT at the output end is composed of:

- (i) The background, attributed to the direct electromagnetic transmission between generator IDT and receiver IDT;
- (ii) The oscillation, resulted from the resonance of the devices (e.g. high frequency cables), this will yield an oscillated background;
- (iii) The SAW, at the frequencies where the SAWs are generated, an electric signal converted from the acoustic wave due to piezoelectric effect will be transmitted to the output IDT, resulting in an enhancement of the signal (see red frames in Fig. 5.2).

A number of interesting aspects are revealed in Fig. 5.2.

Firstly, only the fundamental and odd harmonic excitations are visible – not the even harmonics. The fundamental SAW signal at the first center frequency  $f_i \approx 275$  MHz is followed by further SAW signals at the odd harmonics 3 to 9 (marked by 3<sup>rd</sup>, 5<sup>th</sup>, 7<sup>th</sup>, and 9<sup>th</sup> in Fig. 5.2) at center frequencies of about 824 MHz, 1.37 GHz, 1.86 GHz, and 2.34 GHz, respectively. This agrees with the expectation for strong-coupling material and “conventional” IDTs, i.e. IDTs with identical finger width and finger spacing [115,116]. The electromechanical coupling coefficient  $K^2$  can be obtained from the radiation resistance  $G_a$  and susceptance  $B$  via the crossed-field model according to [117]:

$$K^2 = \left( \frac{\pi G_a}{4N B} \right)_{f=f_i} \quad (5.1)$$

with  $N$  representing the number of IDT finger pairs. The resulting  $K^2$  values for our film are  $(1.4 \pm 0.2)\%$  and  $(0.6 \pm 0.1)\%$  for the directions  $[1\bar{1}0]_{\text{TSO}}$  and  $[001]_{\text{TSO}}$ , respectively. Considering (i) the thinness of our piezoelectric layer (30 nm) and (ii) that the  $K^2$  value strongly decreases with the ratio  $h/\lambda$  ( $h$ : thickness of the layer), this represents an excellent value. For comparison 800 nm thick  $\text{LiNbO}_3$  films and 500 nm thick  $\text{ZnO}$  films showed  $K^2$  factors of 0.52% and  $< 1\%$ , respectively [118,119]. We can therefore conclude that the  $\text{K}_{0.7}\text{Na}_{0.3}\text{NbO}_3$  film is a material with a strong piezoelectric coupling expressed by a large coupling coefficient.

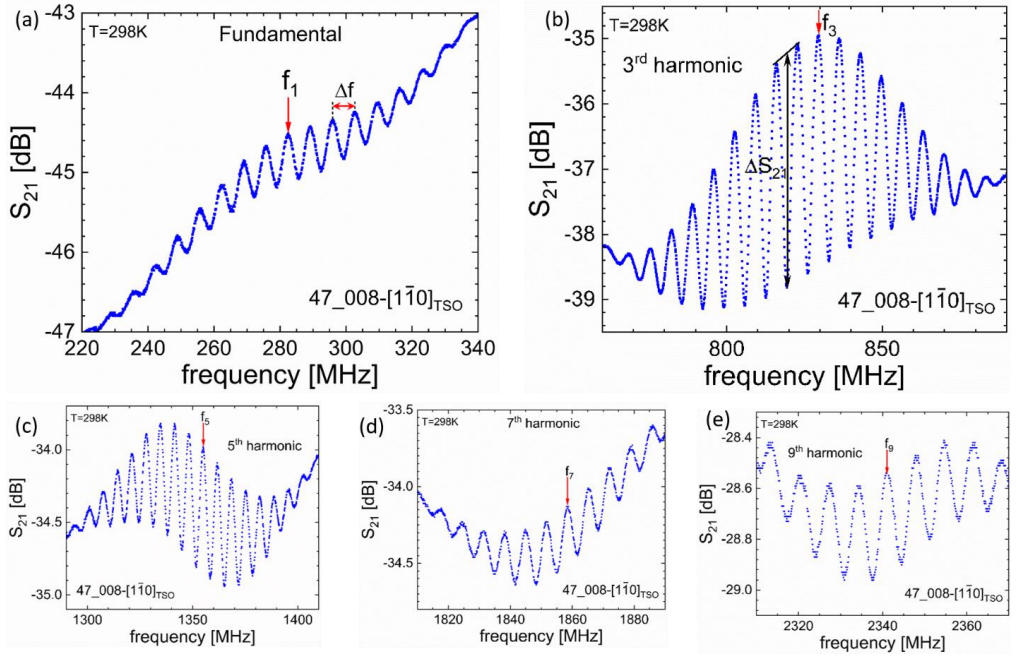


Figure 5.3. Interference pattern of SAW frequency spectrum at (a) fundamental; (b) 3<sup>rd</sup> harmonic; (c) 5<sup>th</sup> harmonic; (d) 7<sup>th</sup> harmonic and (e) 9<sup>th</sup> harmonic. The period of the interference pattern  $\Delta f$  is marked in (a). The amplitude of the interference pattern  $\Delta S_{21}$  is defined in (b) by the peak-to-valley value, which directly provide the intensity of the SAW signal at given frequencies.

Secondly, the SAW spectrum around the center frequency of each harmonic shows the typical interference pattern with a periodicity  $\Delta f$  of about 6.7 MHz. The detailed SAW spectrum at each harmonic is shown in Fig. 5.3(a)-(e). This can be attributed to the interference of acoustic and electromagnetic waves. As just mentioned, the signal at the output IDT includes (i) the directly coupled electromagnetic signal from the input IDT and (ii) the electric signal converted from the acoustic wave. The difference in velocity between acoustic and electromagnetic waves leads to a phase difference between the two components and therefore to the observed interference pattern with a periodicity of:

$$\Delta f = v/L \quad (5.2)$$

where  $L$  represents the distance between input IDT and output IDT. Inserting the SAW velocity yields an expected periodicity of  $(6.68 \pm 0.15)$  MHz, which agrees perfectly with the experimental observation. Later we will use this eq. (5.2) based on the interference pattern to determine the wave velocity of the SAW.

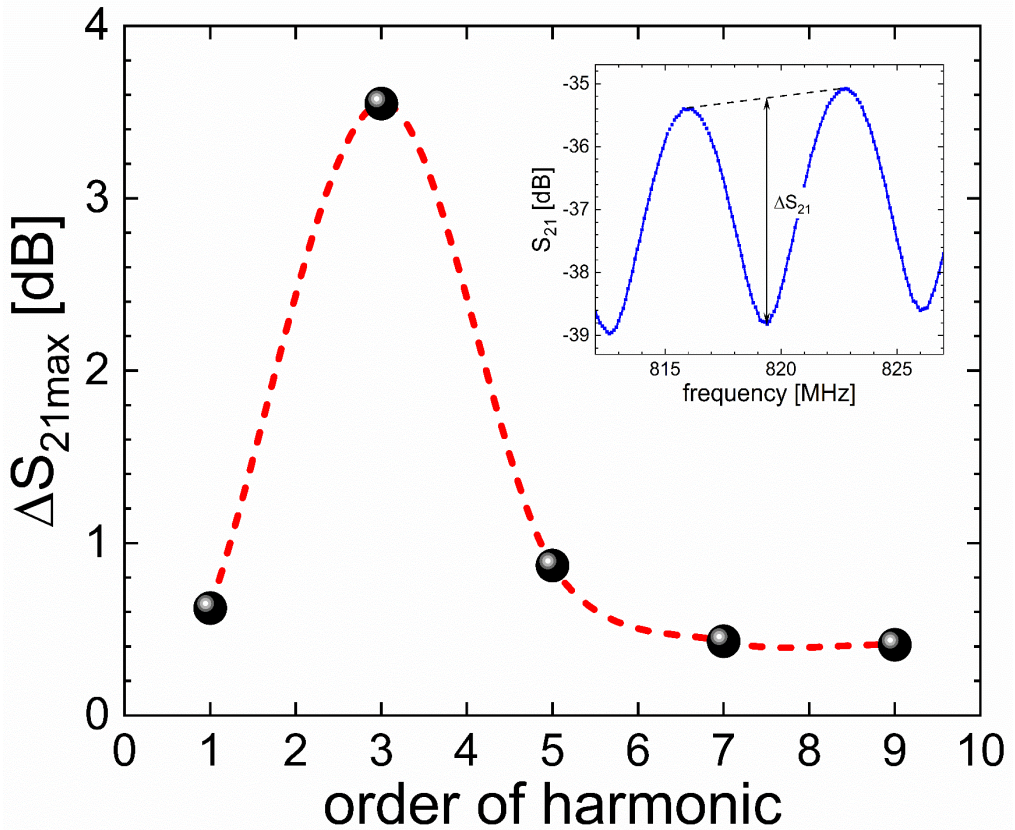


Figure 5.4. SAW intensity  $\Delta S_{21max}$  as function of the order of harmonic. The inset sketches the definition of the amplitude of the interference pattern  $\Delta S_{21}$ .  $\Delta S_{21}$  reaches its maximum  $\Delta S_{21max}$  at the center frequency of each harmonic.

Thirdly, the largest signal is observed for the 3<sup>rd</sup> harmonic. Fig. 5.4 shows the SAW intensity  $\Delta S_{21max}$  as function of the order of harmonic. The amplitude of the interference pattern  $\Delta S_{21}$  is defined in Fig. 5.3(b) by the peak-to-valley value (see also inset in Fig. 5.4), which can directly provide the intensity of the SAW signal at given frequencies. The  $\Delta S_{21}$  reaches to its maximum  $\Delta S_{21max}$  at the center frequency, which is defined as the intensity of each SAW harmonic.

It is shown in Fig. 5.4 that the 3<sup>rd</sup> harmonic possesses the largest intensity among all the observed harmonics. This is rather unusual at first glance. The SAW signal at the different harmonics generally depends on the ratio between the width  $w$  and spacing  $s$  of the electrode's fingers. For  $w/s = 1$ , which agrees with our design, the fundamental excitation should generate the largest SAW signal and the intensity should decrease with the order of the higher harmonic [115]. Moreover, in thin-film SAWs, high-order harmonics are usually quite weak [120]. One explanation for this would be the existence of high-order Sezawa-mode

waves, which are observed in layered structures in which the substrate has a higher acoustic velocity than the overlaying film (see [chapter 2.3](#)). The appearance of this type of wave is determined by the ratio of the piezoelectric film thickness  $h$  and the SAW wavelength  $\lambda$ . Sezawa waves are usually observed when  $h/\lambda > 0.15$  [121,122]. However, in our case  $h/\lambda = 0.0025$  is extremely small and, thus, higher-order Sezawa waves are very unlikely to occur.

Another explanation might be the extreme thinness of the piezoelectric layer compared to typical thin film SAW devices. At the fundamental frequency, the wavelength (12  $\mu\text{m}$ ) is much larger than the film thickness (27 nm). Since the SAW typically penetrates about one wavelength into the free surface, only a small fraction of the mechanical energy can be stored in our very thin  $\text{K}_{0.7}\text{Na}_{0.3}\text{NbO}_3$  film, whilst a large fraction is damped in the non-piezoelectric  $\text{TbScO}_3$  substrate. This situation changes with the higher harmonics. At the 3<sup>rd</sup> harmonic, the wavelength is already 3 times smaller and the energy is generally more concentrated at the surface, meaning a larger amount of the SAW energy is concentrated in the film. As a result, the percentage of SAW energy stored in the thin film increases with the order of harmonics, whilst the general signal height decreases with increasing order. This leads to a maximum of the SAW signal for the 3<sup>rd</sup> harmonic.

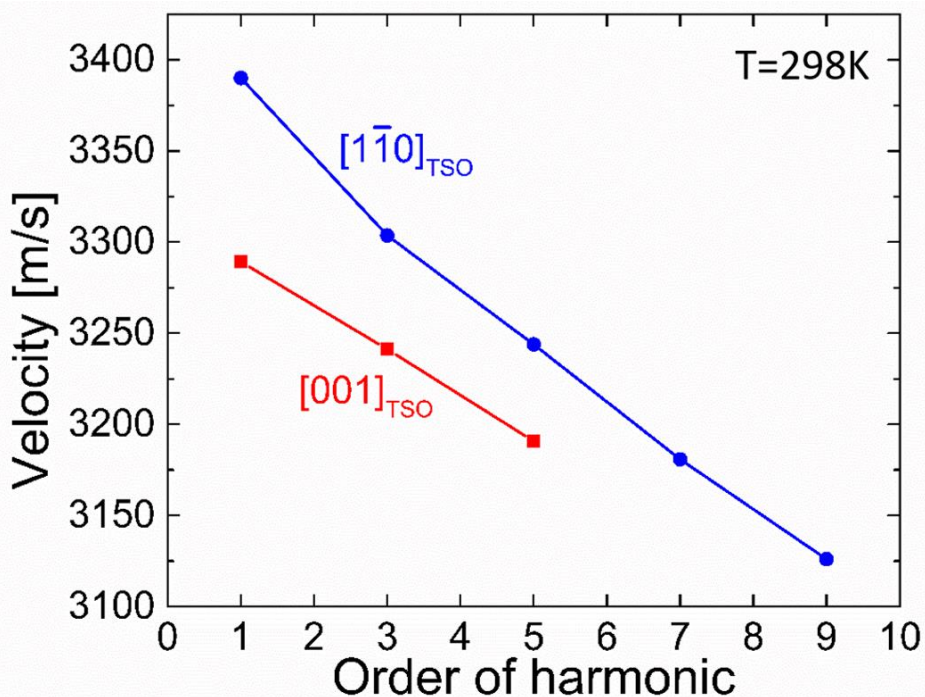


Figure 5.5. Phase velocity of the surface acoustic wave as function of the harmonic order for the directions  $[1\bar{1}0]_{\text{TSO}}$  and  $[001]_{\text{TSO}}$  for a 27nm-thick  $\text{K}_{0.7}\text{Na}_{0.3}\text{NbO}_3$  film on (110)  $\text{TbScO}_3$  (47\_008 TSO) measured at room temperature.

Fourthly, the velocity slightly decreases with the harmonic order (see Fig. 5.5). As shown in the Fig. 5.2, the surface acoustic wave along  $[1\bar{1}0]_{\text{TSO}}$  direction has center frequencies of 282.5, 825.9, 1351.6, 1855.5 and 2344.6 MHz for fundamental, 3<sup>rd</sup>, 5<sup>th</sup>, 7<sup>th</sup> and 9<sup>th</sup> harmonics, respectively. The center frequencies for 3<sup>rd</sup>, 5<sup>th</sup>, 7<sup>th</sup> and 9<sup>th</sup> harmonics are not exactly 3, 5, 7 and 9 times the center frequency of the fundamental but slightly smaller than the integer values. The discrepancy is related to the thickness-to-wavelength ratio,  $h/\lambda$ . As  $h/\lambda$  increase, the velocity of surface acoustic wave decreases. Since the wavelengths of 3<sup>rd</sup>, 5<sup>th</sup>, 7<sup>th</sup> and 9<sup>th</sup> harmonics are 1/3, 1/5, 1/7 and 1/9 the wavelength of fundamental surface acoustic wave,  $h/\lambda$  increases with the order of harmonics. As a result, the velocity of SAW decreases as order of harmonic increase. It shows the expected trend for both crystalline directions in Fig. 5.5.

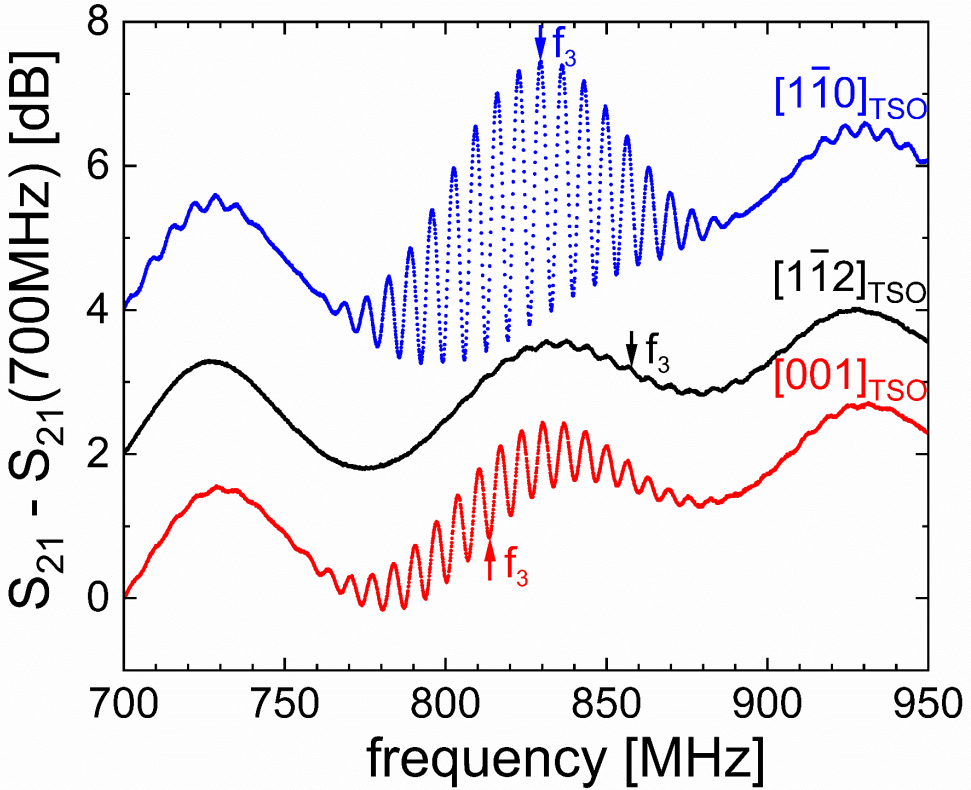


Figure 5.6. Frequency dependence of the transmission signal at the 3<sup>rd</sup> harmonic for SAWs propagating along  $[1\bar{1}0]_{\text{TSO}}$  (blue),  $[001]_{\text{TSO}}$  (red), and  $[1\bar{1}2]_{\text{TSO}}$  directions.

Furthermore, the SAW signal is strongly anisotropic. Fig. 5.6 provides detailed plots of the device signal at the 3<sup>rd</sup> harmonic for SAWs propagating along different orientations of the device. For better visibility,  $S_{21}$  is normalized and vertically shifted for the different measurements. The black arrows denote the respective center frequencies  $f_3$  for the different

directions. The velocity  $v$  of the SAW is obtained from the center frequency and the wavelength  $\lambda$  according to:

$$v = (f_n \cdot \lambda) / n \quad (5.3)$$

with  $n$  representing the order of harmonics. According to this equation, we obtain slightly different SAW velocities for the different directions: 3277 m/s, 3296 m/s, and 3419 m/s for  $[001]_{\text{TSO}}$ ,  $[\bar{1}\bar{1}0]_{\text{TSO}}$ , and  $[\bar{1}\bar{1}2]_{\text{TSO}}$ , respectively. These values are comparable to the velocities measured for classical SAW materials such as  $\text{LiNbO}_3$ ,  $\text{LiTaO}_3$ , and quartz.

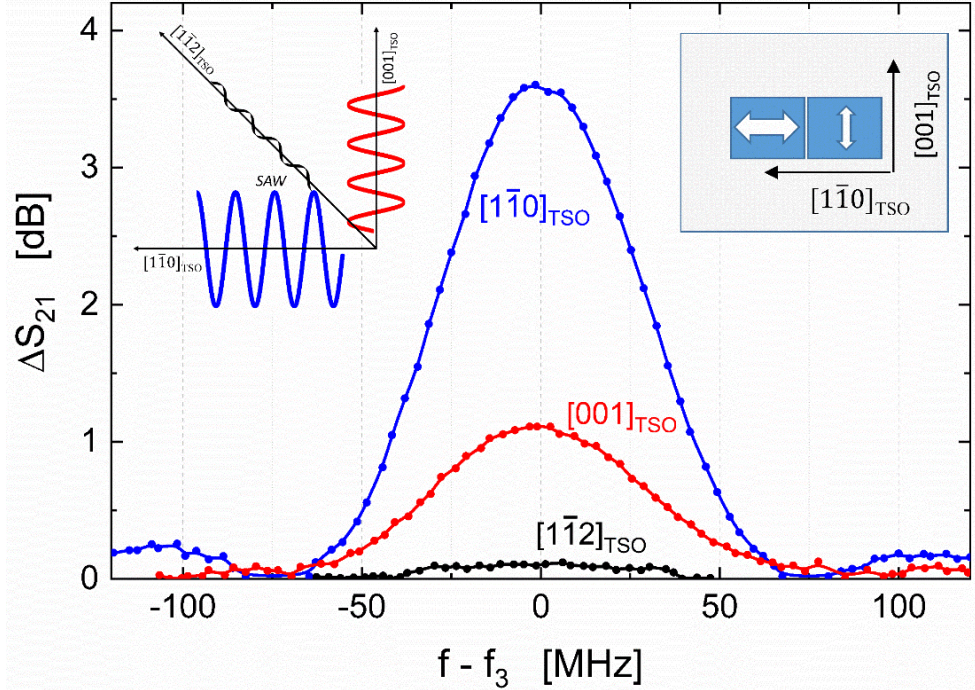


Figure 5.7: Amplitude of the SAW signal ( $\lambda = 12 \mu\text{m}$  and  $L = 500 \mu\text{m}$ ) at the 3<sup>rd</sup> harmonic at frequency  $f_3$  for the different directions –  $[\bar{1}\bar{1}0]_{\text{TSO}}$ ,  $[001]_{\text{TSO}}$ , and  $[\bar{1}\bar{1}2]_{\text{TSO}}$  – of the SAW propagation for a 27 nm-thick  $\text{K}_{0.7}\text{Na}_{0.3}\text{NbO}_3$  film on  $(110) \text{TbScO}_3$  (47\_008 TSO) measured at room temperature. The insets sketch the different SAW intensity along different propagation directions (left) and the possible explanation of the anisotropy of the SAW signal (right) due to two types of domains with different polarizations in  $[\bar{1}\bar{1}0]_{\text{TSO}}$  and  $[001]_{\text{TSO}}$  directions, respectively.

In order to further analyze the SAW signal and its anisotropy, we plotted the amplitude of the SAW interference pattern  $\Delta S_{21}$ , which is defined by the peak-to-valley value within the interference pattern (see Fig. 5.3(b)), around the 3<sup>rd</sup> harmonic (see Fig. 5.7). The parameter  $\Delta S_{21}$  directly provides the intensity of the SAW signal at given frequencies, whilst the center frequency is given by the frequency at which  $\Delta S_{21}$  reaches its maximum. The SAW bandwidth  $B$  is generally expected to be inversely proportional to the number of IDT cells according to:

$$B = 2 \frac{f_0}{N} \quad (5.4)$$

where  $f_0$  and  $N$  represent the fundamental frequency and the number of finger pairs, respectively. In our case, the expected bandwidth is  $(139 \pm 3)$  MHz, which corresponds quite well with the experimental value  $B \approx 138$  MHz observed for all directions.

However, the signal height is very different for the various directions. For example,  $\Delta S_{21}$  is largest for the SAW orientation along  $[1\bar{1}0]_{\text{TSO}}$  ( $\Delta S_{21}(f_3) = 3.6$  dB), whilst the maximum is significantly smaller ( $\Delta S_{21}(f_3) = 1.1$  dB) along the direction  $[001]_{\text{TSO}}$ . For the intermediate direction  $[1\bar{1}2]_{\text{TSO}}$ , it is hardly measurable ( $\Delta S_{21}(f_3) \approx 0.1$  dB). This means that SAWs propagate along the major crystallographic directions at different intensities, but hardly do so in the intermediate direction. This anisotropic behavior could be explained by the polarization and structural anisotropy of the sample. In [ref. \[123\]](#), it was shown that  $\text{K}_{0.7}\text{Na}_{0.3}\text{NbO}_3$  films on  $(110)$   $\text{TbScO}_3$  develop a regular domain structure consisting of four variants of “superdomains” with domain wall alignment under  $\pm 45^\circ$  with respect to  $[001]_{\text{TSO}}$ . Nevertheless, due to charge neutrality reasons there are only two possible in-plane directions of the electrical polarization vector:  $\text{P} \parallel [001]_{\text{TSO}}$  and  $\text{P} \parallel [1\bar{1}0]_{\text{TSO}}$  (see sketch in [Fig. 5.7](#)). As a result, we only expect measurable SAW signals in these two directions. Furthermore, the polarizability and the development of SAWs is slightly different in the major directions  $[001]_{\text{TSO}}$  and  $[1\bar{1}0]_{\text{TSO}}$  due to the slight structural anisotropy of  $\sim 0.025\%$  provided by the difference of the in-plane lattice parameter of the substrate. This difference is also visible in the measurements of permittivity and the resulting ferroelectric transition temperature, which have been discussed in [chapter 4.2](#).

## 5.2 Impact of strain on SAW properties

Obviously the SAW properties should vary with the strain. [Fig. 5.8\(a\)](#) shows the frequency spectrums of MOCVD samples prepared on different substrates and measured at room temperature. All frequency spectra were measured independently by me, Dr. Yang Dai cooperated in the data analysis of the GSO sample, i.e. the cyan and blue curves in [Fig. 5.8](#), which was published in his doctoral thesis [\[25\]](#). A zoom of the frequency spectrum in the regime of the 3<sup>rd</sup> harmonic is shown in [Fig. 5.8\(b\)](#). Please note that the data are uncalibrated which especially due to the used bonding technology leads to different background signal. Nevertheless, in most cases the characteristic interference pattern of the SAW at the different harmonics are visible.

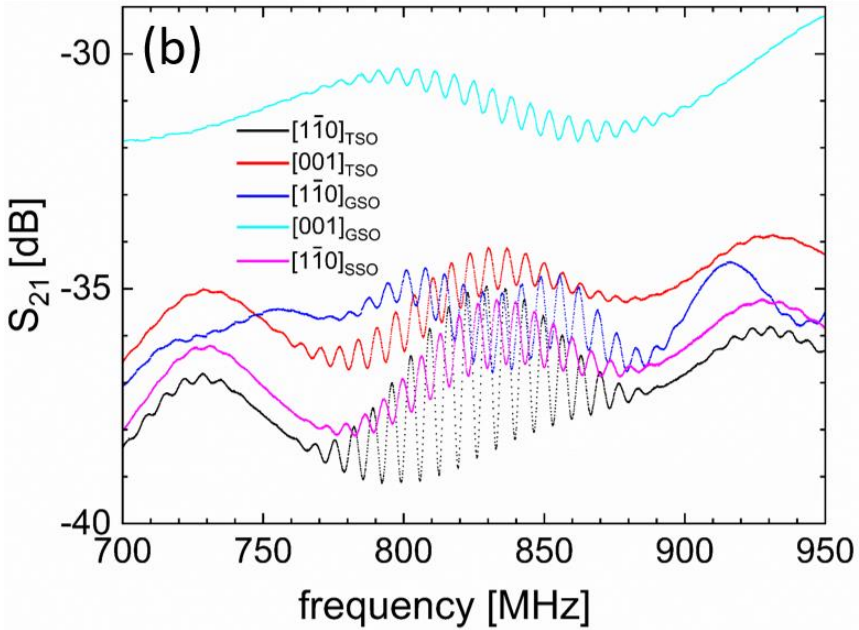
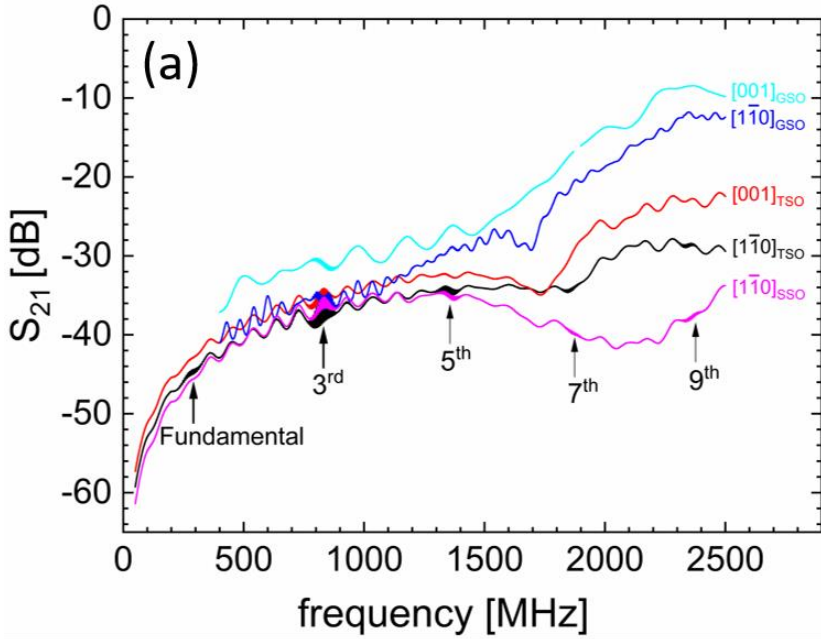


Figure 5.8. (a) Frequency dependence of the transmission signal of SAW structures aligned along [001] and  $[1\bar{1}0]$  substrate orientations for a 27 nm-thick  $K_{0.7}Na_{0.3}NbO_3$  film on  $TbScO_3$  (47\_008 TSO), a 27 nm-thick  $K_{0.7}Na_{0.3}NbO_3$  film on  $GdScO_3$  (47\_008 GSO), and a 27 nm-thick  $K_{0.7}Na_{0.3}NbO_3$  film on  $SmScO_3$  (47\_008 SSO) measured at RT. The IDTs are identical to those shown in Fig. 5.1. (b) A zoom of the regime of the 3<sup>rd</sup> harmonic for all the frequency spectrums.

The SAW signal of all MOCVD samples shows a similar behavior, namely the strongest SAW signal appears at the 3<sup>rd</sup> harmonic and the intensity and also velocity (not shown here) decrease as the order of harmonic increases. However, the SAW intensity varies with the strain. The relationship between the intensity of the 3<sup>rd</sup> harmonic  $\Delta S_{21}(f_3)$  and the in-plane compressive strain is shown in Fig. 5.9. The “square model” (see chapter 4.2) is applied in Fig. 5.9(a) to evaluate the in-plane strain, whereas the “normal lattice model” is used in Fig. 5.9(b) to investigate the strain dependence of SAW intensity.

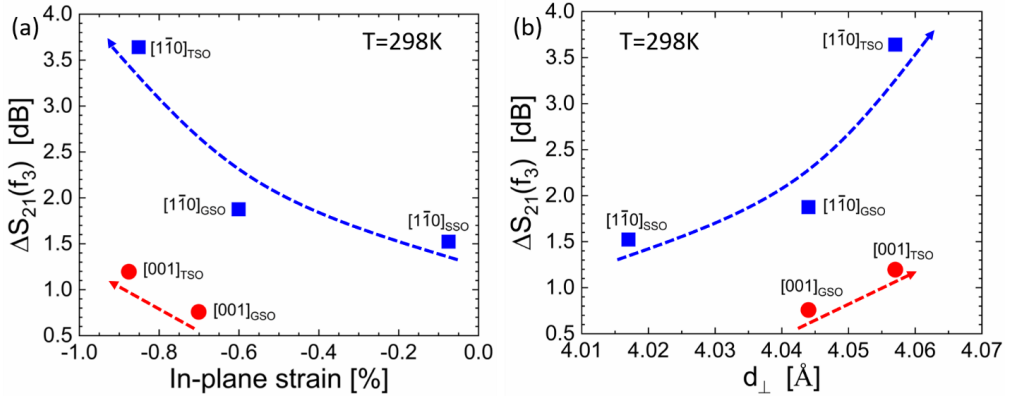


Figure 5.9. SAW intensity of the 3<sup>rd</sup> harmonic at RT as function of in-plane compressive strain evaluated from (a) the “square model” and (b) the “normal lattice model”.

Firstly, all samples show similar anisotropic behavior, namely the SAW intensity along the  $[1\bar{1}0]_{\text{sub}}$  direction is larger than that along the  $[001]_{\text{sub}}$  direction, which has been discussed in the last chapter. Secondly, the SAW intensity at the 3<sup>rd</sup> harmonic increases with the in-plane compressive strain (Fig. 5.9(a)) as well as the vertical lattice parameter of the KNN film (Fig. 5.9(b)). Since the increase of the vertical lattice parameter indicates an increase of the in-plane compressive strain, the two evaluation methods are in good agreement with each other. This again supports that our new model based on the vertical lattice parameter might represent a useful tool to investigate the strain dependent behavior in epitaxial films.

A larger in-plane compressive strain shifts the phase transition temperature closer to RT (see chapter 4.2). Since we could not detect any SAW signal for samples with  $T_C < \text{RT}$  (i.e. no ferroelectricity at RT), the largest SAW signal is expected for samples with  $T_C$  values close to RT. This means the compressive strain should be sufficient but not too large to shift the phase transition temperature below RT. The optimum case seems to be obtained for our set of substrates for  $\text{TbScO}_3$ , nevertheless, maybe there exist even better candidates (i.e. single crystalline substrates) which lead to an even better strain and, then,  $T_C$  suppression. Therefore, it is of importance to look at the temperature dependence of the SAW signal and permittivity.

### 5.3 Temperature dependence of permittivity and SAW signal

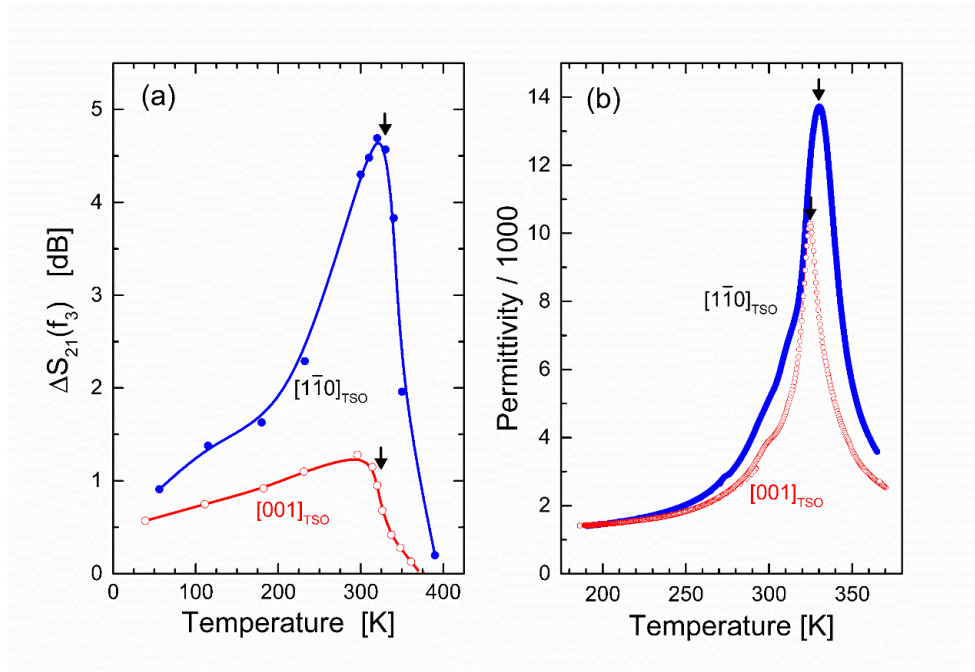


Figure 5.10. Comparison of the temperature dependence of the SAW signal ( $\lambda=12\mu\text{m}$  and  $L=500\mu\text{m}$ ) at the 3<sup>rd</sup> harmonic (a) and dielectric permittivity (b) for the different directions of the electric field and SAW propagation for a 27 nm-thick  $K_{0.7}Na_{0.3}NbO_3$  film on  $TbScO_3$  (47\_008 TSO). The arrows denote the temperature of the ferroelectric phase transition, again defined by the temperature of maximum permittivity.

Fig. 5.10 shows a comparison of the temperature dependence of the SAW signal at the 3<sup>rd</sup> harmonic and the corresponding permittivity for the different electric field and SAW propagation directions for the KNN films on  $TbScO_3$ . The permittivity data of Fig. 5.10(b) have also been shown in Fig. 4.4(a).

The large permittivity of  $\epsilon'_{max} \approx 10,300$  and 14,000 at  $T_C \approx 324$  K and 330 K, respectively, (see Fig. 5.10(b)) demonstrates the large polarizability of the  $K_{0.7}Na_{0.3}NbO_3$  film around RT. The temperature dependence resembles the typical behavior of a ferro-to-paraelectric transition with a peak in the permittivity  $\epsilon'$  at the transition temperature  $T_C$ . Due to the compressive strain,  $T_C$  is reduced from 693 K for unstrained bulk  $K_{0.7}Na_{0.3}NbO_3$  to 324 K and 330 K for the directions  $[1\bar{1}0]_{TSO}$  and  $[001]_{TSO}$ , respectively. The small difference in  $T_C$  obtained for both directions results from the small difference in the strain. As a result of the shift of  $T_C$ , the peak in the permittivity also shifts towards room temperature. For instance, a permittivity of  $\epsilon'_{[001]}$

$= 3970$  and  $\varepsilon'_{[1\bar{1}0]} = 5160$  is measured at RT, which rises up to  $\varepsilon'_{[001]} = 10270$  and  $\varepsilon'_{[1\bar{1}0]} = 13695$  at the respective  $T_C$ .

A similar behavior is visible in the SAW experiments (Fig. 5.10(a)). The anisotropy is even more pronounced for the SAW signal compared to the permittivity measurement. For both major directions, the SAW signal  $\Delta S_{21}(f_3)$  exhibits a maximum slightly below the ferroelectric phase transition  $T_C$ , reaching maximum values of 1.3 dB and 4.7 dB for the different directions. Since the transition temperature is adjusted via strain to a temperature slightly above room temperature, the room temperature values for  $\Delta S_{21}(f_3)$  were found to be close to the maximum values. Above  $T_C$ , the SAW signal declines rapidly and finally vanishes slightly below 400 K. This supports the strain dependence of the SAW intensity discussed in the last chapter.

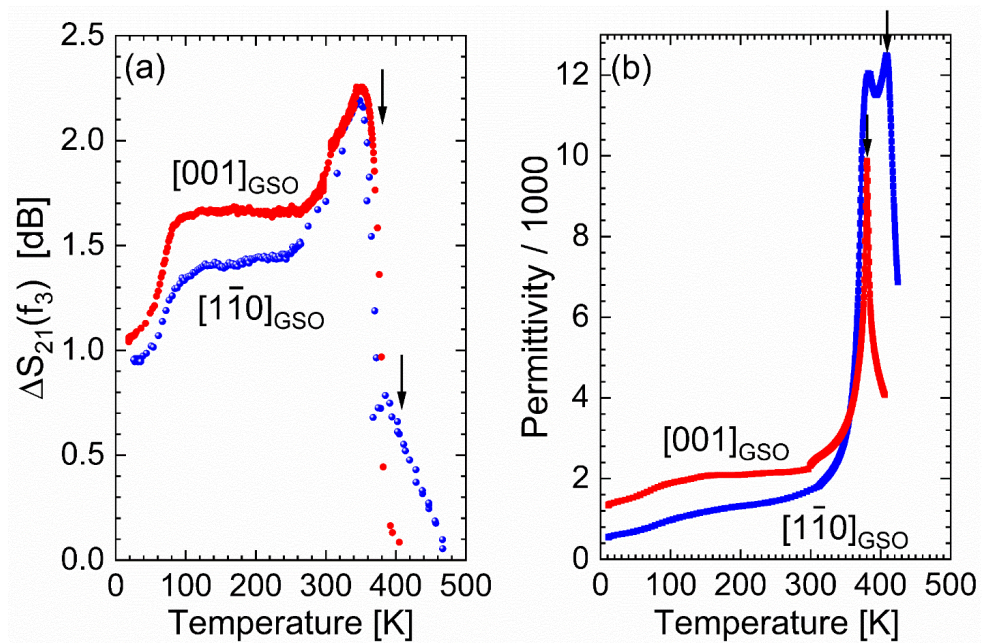


Figure 5.11. Temperature dependence of the SAW signal ( $\lambda=12\mu\text{m}$  and  $L=500\mu\text{m}$ ) at the 3<sup>rd</sup> harmonic (a) and dielectric permittivity (b) for the different directions of the electric field and SAW propagation for a 27 nm-thick  $K_{0.7}Na_{0.3}NbO_3$  film on  $GdScO_3$  (47\_008 GSO). The arrows denote the temperature of the ferroelectric phase transitions.

In case of MOCVD prepared 47\_008 GSO sample, the phase transition and anisotropy of permittivity seems to be a little bit more complicated. An additional peak is observed for the permittivity measurement along the  $[1\bar{1}0]_{GSO}$  direction (see Fig. 5.11(b)). However, the position of the first peak coincides with the peak observed for the  $[001]_{GSO}$  direction. It has been observed before in other thin film perovskite systems (e.g.  $SrTiO_3$ ) and can be attributed to the integral character of the permittivity measurement. With other words, we do see both

transitions ( $[1\bar{1}0]_{\text{GSO}}$  and  $[001]_{\text{GSO}}$ ) in the measurement along the  $[1\bar{1}0]_{\text{GSO}}$  direction. Therefore, we end up with two transition at  $T_{C,[1\bar{1}0]} = 408.7$  K and  $T_{C,[001]} = 380.2$  K. All these features (i.e. lower SAW signal below  $T_C$ , maxima at  $T_C$ , and vanishing signal above  $T_C$ ) are reflected in the temperature dependence of the SAW signal shown in Fig. 5.11(a).

The important parameter which is later used for the sensor application is not the amplitude (and its attenuation) but the velocity of the SAW. Fig. 5.12 shows the temperature dependence of the SAW velocity for one of the MOCVD samples (47\_008 GSO).

The permittivity along  $[001]_{\text{GSO}}$  direction is larger than that along the  $[1\bar{1}0]_{\text{GSO}}$  direction at temperature below 350 K, whilst smaller than that along the  $[1\bar{1}0]_{\text{GSO}}$  direction at temperature higher than 350K. All these features are reflected in the curve of SAW intensity as function of temperature, as shown in Fig. 5.8(a).

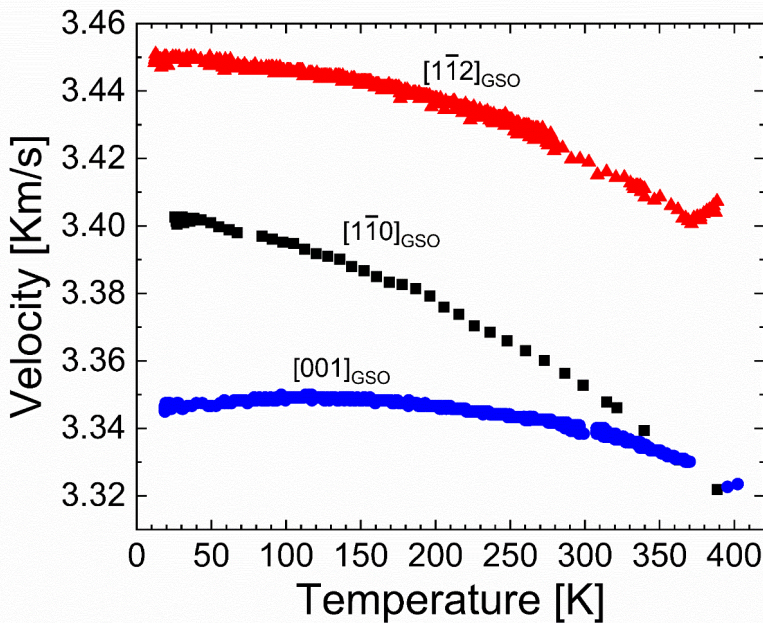


Figure 5.12. Temperature dependence of the SAW velocities for a 27 nm-thick  $K_{0.7}Na_{0.3}NbO_3$  film on  $GdScO_3$  (47\_008 GSO) along  $[001]_{\text{GSO}}$ ,  $[1\bar{1}0]_{\text{GSO}}$ , and  $[1\bar{1}2]_{\text{GSO}}$  directions. The increase of the SAW velocity at high temperatures might be an artifact of the experiment.

The SAW velocity is slightly different for the different crystallographic orientations, which could be related to different material constants, e.g. density and elastic modulus, for different orientations. Moreover, the SAW velocity doesn't exhibit any "phase transition-like" behavior in the examined temperature regime (10 K to 350 K) which could be an indication for changes of material constants at structural phase transitions. Considering the phase transition

temperature of the sample is in the range of 380-400 K, the accessible temperature regime of the measurement might be too low to see such a phase transition.

## 5.4 Summary

In this chapter, the SAW properties of MOCVD samples are investigated. The SAW generation and detection are illustrated, the SAW intensity, velocity, and anisotropy are discussed, and the strain and temperature dependence of SAW properties are studied. The main results are:

- (i) The SAW properties of our KNN thin films are comparable or better than other commonly used SAW materials like ZnO, AlN, and LiNbO<sub>3</sub> (see [table 5.1](#)):
  - a. The intensity of the SAW signal of our KNN thin film system, represented by  $\Delta S_{21}$ , is comparable to even bulk LiNbO<sub>3</sub> system.
  - b. Considering the thinness ( $\sim 30$  nm) of our film system and the fact that electromechanical coupling coefficient  $K^2$  decreases significantly with the ratio  $h/\lambda$ , our KNN system is promising for miniaturized SAW applications.
  - c. Moreover, attributed to the generation of higher orders of SAW, the operation frequency of our KNN film system is much higher than other SAW systems. Since the sensitivity of SAW sensors is proportional to the square of operational frequency (see [chapter 2.3](#)), our SAW system could be extremely sensitive when applied as a SAW sensor.

Table 5.1: Comparison of SAW properties of our  $K_xNa_{1-x}NbO_3$  thin films and other commonly used SAW systems at RT.

Material	$\Delta S_{21}/\text{dB}$	Film/Bulk	Thickness	Operation Frequency
$K_{0.7}Na_{0.3}NbO_3$	3.6	film	30 nm	830 MHz to 2.3 GHz
ZnO [121]	8.1	film	5.5 $\mu\text{m}$	173 MHz
ZnO [124]	1.9	film	500 nm	360 MHz
AlN [122]	15	film	3.5 $\mu\text{m}$	120.6 MHz
LiNbO <sub>3</sub> [118]	10	bulk	1 mm	172 MHz

- (ii) The SAW properties are anisotropic. The strongest SAW is obtained along the main crystalline directions of the substrate  $[001]_{\text{sub}}$  and  $[\bar{1}\bar{1}0]_{\text{sub}}$  of the substrate, but the SAW is hardly visible along intermediate crystalline directions, e.g.  $[\bar{1}\bar{1}2]_{\text{sub}}$ . This anisotropic behavior could improve the focusing of SAWs.

(iii) The temperature dependence of SAW signal seems to be comparable to that of permittivity. As a consequence, a maximum SAW signal is expected close to  $T_C$ , e.g.  $\Delta S_{21}$  up to 4.7 dB was observed at the temperature around the ferroelectric phase transition for 47\_008 TSO sample.

The outstanding SAW properties of the MOCVD samples are promising for SAW sensor applications. A thin film SAW sensor system based on MOCVD samples will be demonstrated in [chapter 7](#).

## 6 Tunable SAW properties of relaxor-type ferroelectric (K,Na)NbO<sub>3</sub>

In this chapter we discuss the SAW properties of the PLD-prepared KNN samples. As shown in [chapter 4.2](#), the PLD samples exhibit the typical behavior of relaxor-type ferroelectrics. This textbook-like relaxor-type ferroelectric behavior will first be characterized for PLD-prepared KNN thin films, then we demonstrate that the SAW properties of the relaxor-type ferroelectrics depend strongly on the applied external electric field. Finally, polar nanoregions (PNR) based model is proposed to explain the novel SAW behavior of these films, the tunable SAW signal.

This chapter is based on our publication [125]: **S. Liang**, D. Pfützenreuter, D. Finck, L. von Helden, J. Schwarzkopf, R. Wördenweber, Appl. Phys. Lett. **116**, 052902 (2020).

### 6.1 SAW properties without dc bias

Sample DP\_1303 TSO (25 nm K<sub>0.7</sub>Na<sub>0.3</sub>NbO<sub>3</sub> on (110) TbScO<sub>3</sub>) has been taken as an example for the characterization of the ferroelectric behavior of the PLD samples. Although RSMs of the high resolution XRD experiments confirm the epitaxial growth of our PLD films, they indicate an onset of plastic lattice relaxation of the strained films (see [Figs. 6.1\(a\) and \(b\)](#) and compare with discussion in [chapter 4.1](#)). The maxima of the  $q_{\parallel}$  positions of the KNN reflections coincide with the substrate reflections  $(620)_{\text{TSO}}$  ( $q_{\parallel} = 3.1733 \text{ \AA}^{-1}$ ) and  $(444)_{\text{TSO}}$  ( $q_{\parallel} = 3.1745 \text{ \AA}^{-1}$ ). However, both the absence of satellite patterns (indicative of a regular arrangement of domains [123]) and especially the broadness of the KNN layer reflection and its distortion in the direction of unstrained KNN are clear indications of a plastic relaxation of the strained KNN layer structure.

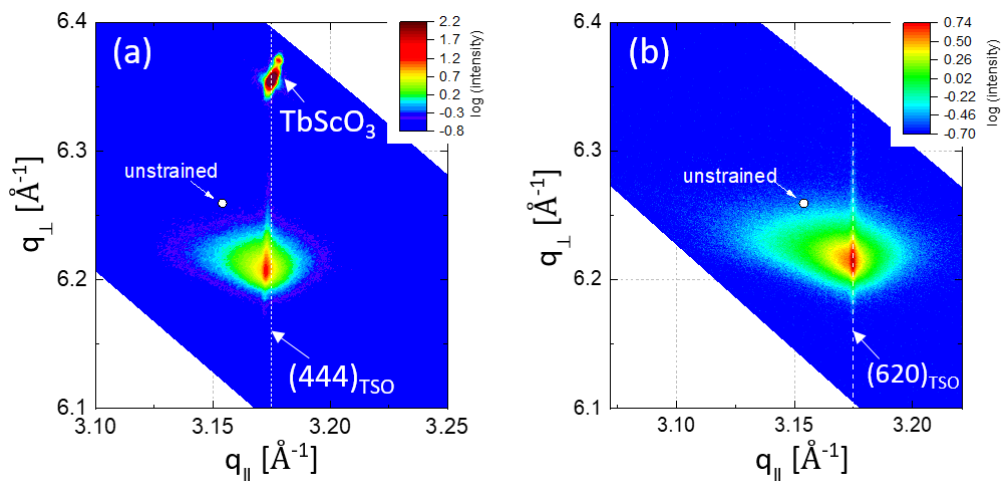


Figure 6.1. X-ray reciprocal space maps (RSM) in the vicinity of the (a) (444) and (b) (620) Bragg reflections of the TbScO<sub>3</sub> substrate, the dashed white lines and white dots in (a) and (b) mark the  $q_{\parallel}$  position of the TbScO<sub>3</sub> and the expected position of unstrained KNN, respectively. (Measurement D. Pfützenreuter, IKZ Berlin)

Usually, epitaxially strained films exhibit relaxor-type ferroelectric behavior [52]. This is even more likely for strained films showing plastic strain relaxation. The relaxors possess peculiar features which are correlated to the formation of polar nano regions. At high temperatures, relaxors exist in a non-polar paraelectric phase, which is similar to the paraelectric phase of ordinary ferroelectric. Upon cooling, they transition into an ergodic relaxor state, in which polar regions are formed on the nanometer scale with a random orientation of dipole moment (see also detailed introduction in chapter 2.2). Since relaxor-type behavior can strongly affect the ferroelectric properties, we first analyze the temperature and frequency dependence of the KNN film and demonstrate its textbook relaxor behavior.

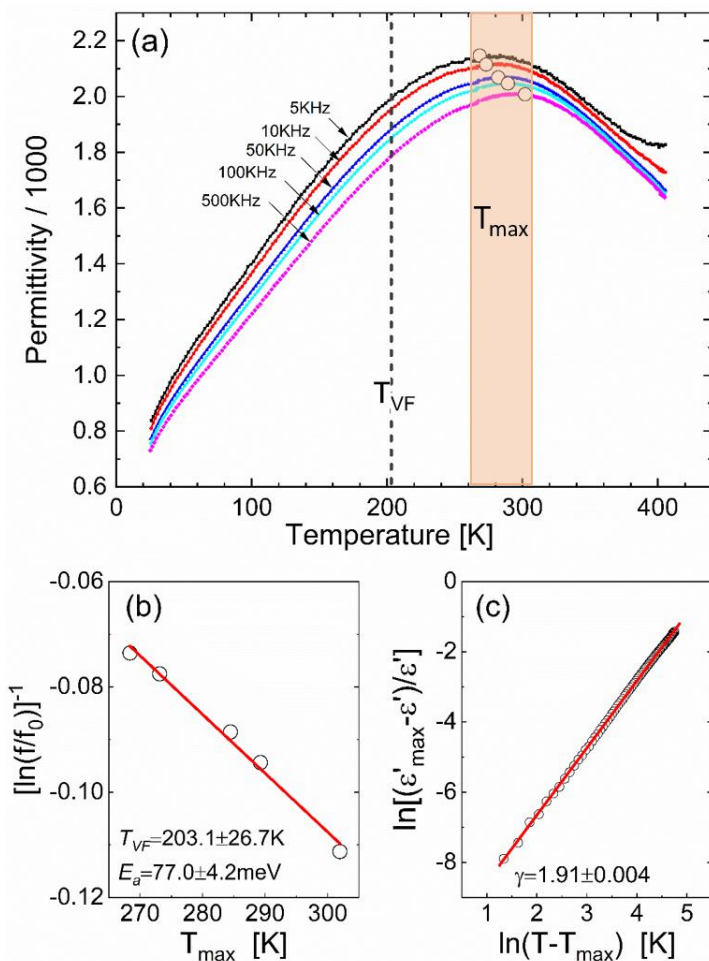


Figure 6.2. (a) Temperature dependence of the permittivity at different frequencies, (b) resulting Vogel-Fulcher fit (solid line) using an attempt frequency  $f_0=4$  GHz, and (c) Lorentz fit (solid line) of the permittivity measured at 100 kHz for a 25 nm-thick  $K_{0.7}Na_{0.3}NbO_3$  film on (110)  $TbScO_3$  (DP\_1303 TSO). The reddish shaded area in (a) marks the temperature regime of maximum permittivity.

Fig. 6.2(a) shows the temperature dependence of the permittivity measured at different frequencies for DP\_1303 TSO.

First, the broadness of the transition peak can be scaled according to the empirical Lorentz relation (see chapter 4.2):

$$\frac{\varepsilon'_{max}}{\varepsilon'} = 1 + \frac{(T - T_{max})^\gamma}{2\sigma^2} \quad (6.1)$$

for  $T > T_{max}$ , where  $\varepsilon'_{max}$  is the maximum permittivity at  $T_{max}$ ,  $\gamma$  is the degree of dielectric relaxation, and  $\sigma$  is the degree of diffuseness of the phase transition. A sharp transition peak near  $\gamma = 1$  indicates a conventional ferroelectric, whereas the relaxor-type phase transition is usually characterized by a broad peak with  $\gamma$  ranging from 1.5 to 2. Our KNN film shows a broad peak with  $\gamma \approx 1.9$  at measurement frequency of 100 KHz (see Fig. 6.1(c)).

Second, not only the frequency dispersion of the permittivity but also the frequency dependence of the temperature  $T_{max}$  are clear indications of a relaxor-type ferroelectric. The frequency dependence of  $T_{max}$  (marked in Fig. 6.1(a)) of a relaxor typically obeys the Vogel-Fulcher law [112,113]:

$$f = f_0 \exp \left[ -\frac{E_a}{k_B(T_{max} - T_{VF})} \right] \quad (6.2)$$

with activation energy  $E_a$ , Vogel-Fulcher freezing temperature  $T_{VF}$ , attempt frequency  $f_0$ , and Boltzmann constant  $k_B$ . A logarithmic transformation of Eq. (6.1) gives:

$$\left[ \ln \left( \frac{f}{f_0} \right) \right]^{-1} = -\frac{k_B}{E_a} (T_{max} - T_{VF}) \quad (6.3)$$

By choosing a reasonable attempt frequency (e.g.  $f_0 = 4$  GHz) we can extract  $E_a \approx (77 \pm 4)$  meV and  $T_{VF} \approx (203 \pm 27)$  K for our KNN film from the resulting Vogel-Fulcher fit (Fig. 6.1(b)). The former describes the energy needed for the reorientation of the PNRs' polarization, while the latter characterizes the temperature below which the PNRs start to freeze, i.e. become immobile.

We therefore conclude that our PLD-prepared KNN films are textbook examples of relaxor-type ferroelectric.

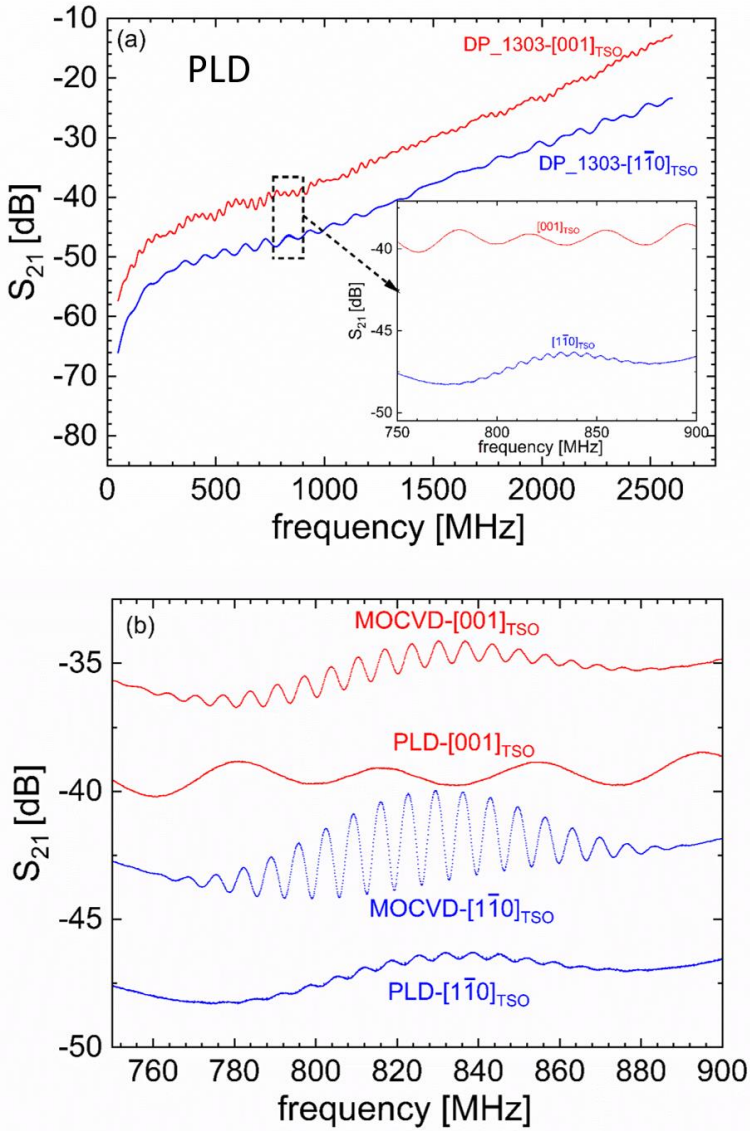


Figure 6.3. (a) Transmission signal of SAW structures aligned along the  $[1\bar{1}0]_{\text{Tso}}$  and  $[001]_{\text{Tso}}$  directions ( $\lambda=12 \mu\text{m}$  and  $L=500 \mu\text{m}$ ) on a PLD sample (DP\_1303 TSO), the inset shows a detailed plot of the signal at the 3<sup>rd</sup> harmonic, (b) comparison of the SAW signal (3<sup>rd</sup> harmonic) of a MOCVD sample (47\_008 TSO) and a PLD sample (DP\_1303 TSO). The KNN films are deposited on  $(110) \text{TbScO}_3$ , the data are recorded at RT.

Fig. 6.3 shows the SAW signal of the PLD sample DP\_1303 TSO measured at RT for  $[1\bar{1}0]_{\text{Tso}}$  and  $[001]_{\text{Tso}}$  directions. The SAW signal of the PLD sample turns out to be extremely weak (see Fig. 6.3(a) and inset), it is hardly visible along the  $[001]_{\text{Tso}}$  direction and barely visible for

the 3<sup>rd</sup> harmonic along  $[1\bar{1}0]_{\text{TSO}}$  direction ( $\Delta S_{21} \approx 0.2$  dB). In comparison to a comparable MOCVD sample (47\_008 TSO, Fig. 6.2(b)), the signal is at least 15 times weaker in the PLD sample.

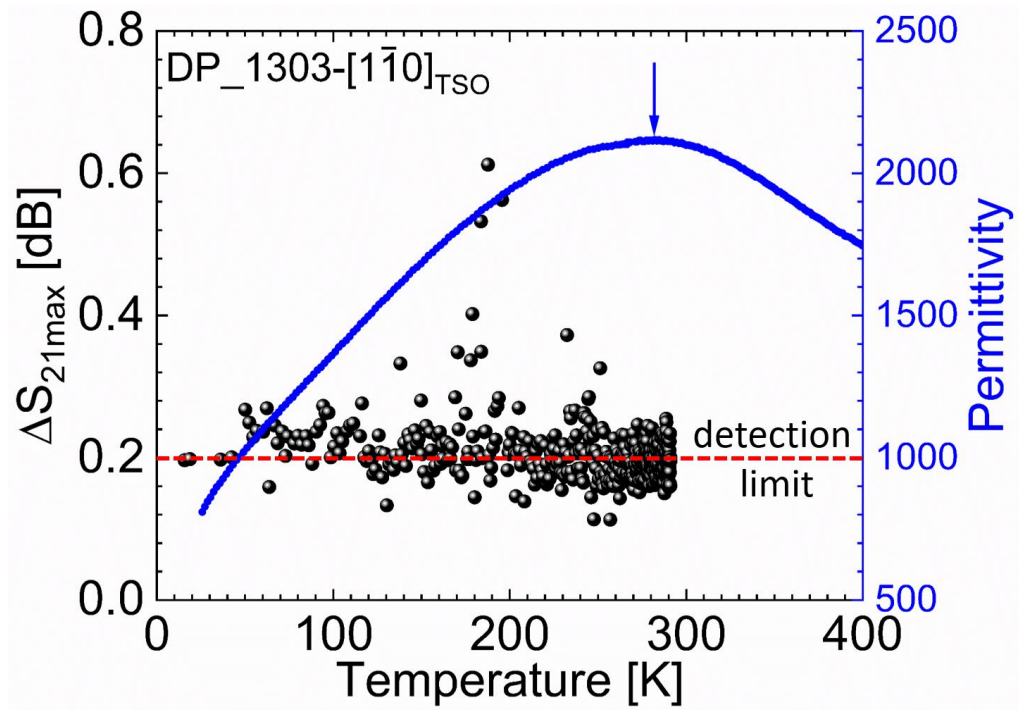


Figure 6.4. Temperature dependence of SAW intensity (symbols) and permittivity (line) for PLD-prepared 25 nm-thick  $K_{0.7}Na_{0.3}NbO_3$  film on  $(110)$   $TbScO_3$  (DP\_1303 TSO). The arrow marks the position of the temperature of maximum permittivity. The dashed red line indicates the detection limit of the measurement.

Since the phase transition temperature of this sample (DP\_1303 TSO) seems to be below RT (279 - 289 K), and since we expect the strongest SAW at temperatures around the ferroelectric phase transition, the sample has been cooled down to  $\sim 10$  K to investigate the temperature dependence of the SAW signal strength (see Fig. 6.4). The SAW signal is extremely small for the whole temperature regime (10 K to RT) and close to the detection limit of  $\sim 0.2$  dB. Therefore, we do not see any feature in the temperature dependence, only a few times (mainly around 200 K) a slightly larger signal ( $\sim 0.6$  dB) pops up.

## 6.2 DC bias tuning of the SAW

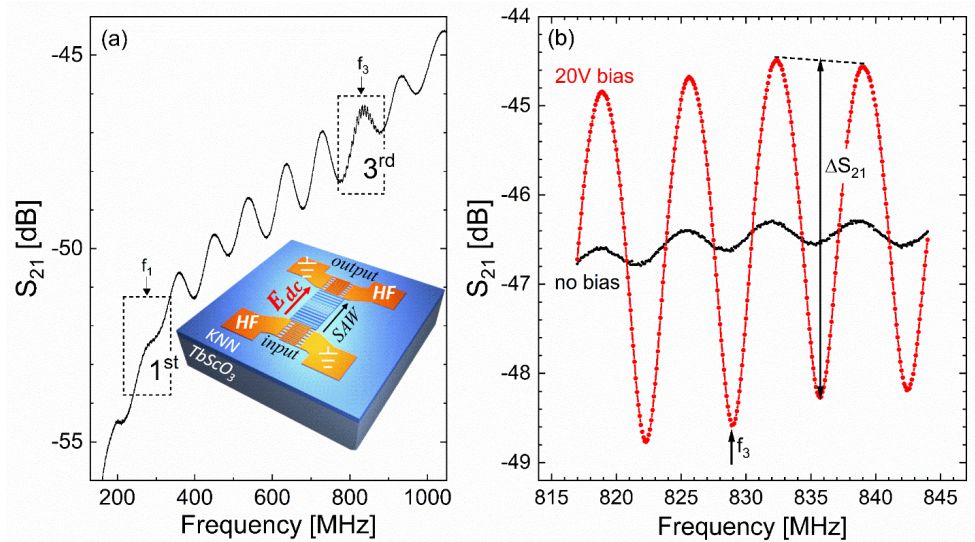


Figure 6.5. Frequency dependence of the transmission signal of a SAW structure with IDTs with a periodicity  $\lambda = 12 \mu\text{m}$  and distance  $L = 500 \mu\text{m}$  on a 25 nm-thick  $\text{K}_{0.7}\text{Na}_{0.3}\text{NbO}_3$  film on  $\text{TbScO}_3$  (DP\_1303 TSO) measured along the  $[1\bar{1}0]_{\text{TSO}}$  direction at room temperature; (a) shows the signal including the 1<sup>st</sup> (fundamental) and 3<sup>rd</sup> harmonic for zero DC bias, whereas (b) provides a comparison of the zero bias and 20 V-bias signals at the 3<sup>rd</sup> harmonic. The schematic illustrates that the DC bias is applied on a pair of diagonal HF electrodes, whereas the other electrodes are grounded.

Fig. 6.5 summarizes the SAW data obtained at room temperature for a PLD sample. A first complete frequency scan of the response of the IDTs oriented along the  $[1\bar{1}0]_{\text{TSO}}$  direction shows the disappointingly small signal while was already discussed in the previous section. As discussed in chapter 5, due to the thinness of the film and the design of the IDTs, only odd harmonic excitations are visible and the largest SAW signal is expected for the 3<sup>rd</sup> harmonic at center frequency of  $f_3 = 828.8 \text{ MHz}$ . However, in these samples, the signal is hardly measurable for the 1<sup>st</sup> harmonic and very small for the 3<sup>rd</sup> harmonic (e.g.  $\Delta S_{21} \approx 0.2 \text{ dB}$  in Fig. 6.5(a)).

This situation changes significantly with the application of a DC bias. The amplitude of the SAW's interference pattern at the odd harmonics, which is attributed to the interference between acoustic and electromagnetic waves at the output IDTs, is greatly boosted by the DC field. The schematic in Fig. 6.5(a) illustrates how we apply the DC bias. The DC bias is applied on a pair of high frequency (HF) electrodes, whereas the other electrodes are grounded. We found that only when the bias is applied on a pair of diagonal (not parallel) electrodes, it has an impact on the SAW signal. We believed that it is because the DC bias is shielded by the fingers within the IDTs when applied in other ways, which need to be further investigated.

As shown in Fig. 6.5(b),  $\Delta S_{21}(f_3)$  increases from  $\sim 0.2$  dB for zero-field to  $\sim 4$  dB at a DC bias of 20 V. The latter value is comparable to results obtained without bias for MOCVD-grown KNN films with comparable thickness and stoichiometry but better crystallinity (see chapter 5).

Since the impact of the DC bias on the SAW signal might be attributed to the relaxor-type behavior of the KNN film, especially the arrangement and alignment of the PNRs, we examined the bias dependence of the SAW signal as well as its temperature dependence and relaxation behavior in more detail.

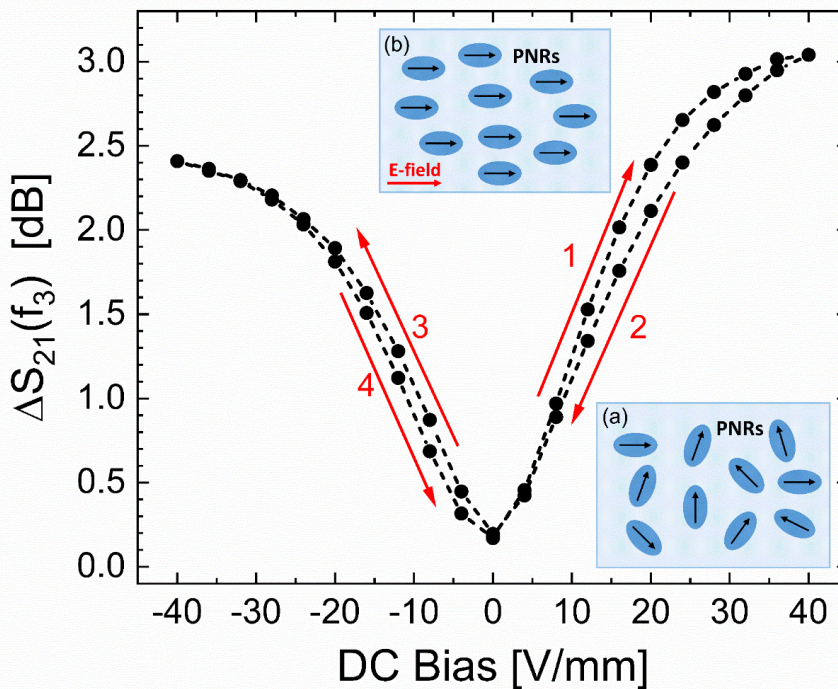


Figure 6.6. DC-bias dependence of the SAW intensity for a 25 nm-thick  $K_{0.7}Na_{0.3}NbO_3$  film on  $(110)$   $TbScO_3$  at room temperature. The red arrows reveal the sequence of applying the DC field; the dashed lines act as a visual guide.

Fig. 6.6 shows the DC-bias dependence of the SAW signal. We analyzed the electric field dependence of the maximum amplitude  $\Delta S_{21}(f_3)$  by modifying the bias incrementally by  $\pm 2$  V (i.e.  $\pm 4$  V/mm) between  $-20$  V and  $20$  V starting at zero field. The DC field and SAWs are oriented in  $[1\bar{1}0]_{T\text{SO}}$  direction. The sample shows a butterfly-type tunability of the SAW signal:

- (i) Generally, the SAW signal increases with the DC field for positive and negative bias. This increase seems to level off for a large field. Furthermore, a small asymmetry can be observed (i.e. the signal is larger for a positive field).

- (ii) The bias dependence shows slight hysteretic behavior, although all data points were recorded after a long stabilization (~20 min) at a given DC field.

The schematics in Fig. 6.6 illustrate the mechanism of the tunability of SAWs, which is believed to be related to the reorientation of the PNRs under the DC field. At a low DC field (inset (a)), the PNRs are randomly distributed in the matrix, and the disordered polarization state dramatically attenuates the generation and propagation of SAWs, resulting in a very weak SAW signal. Meanwhile at a high DC field, the PNRs become oriented (or better oriented) by the E-field, inducing an ordered polarization state which facilitates the generation and propagation of SAWs and thus a strong SAW signal.

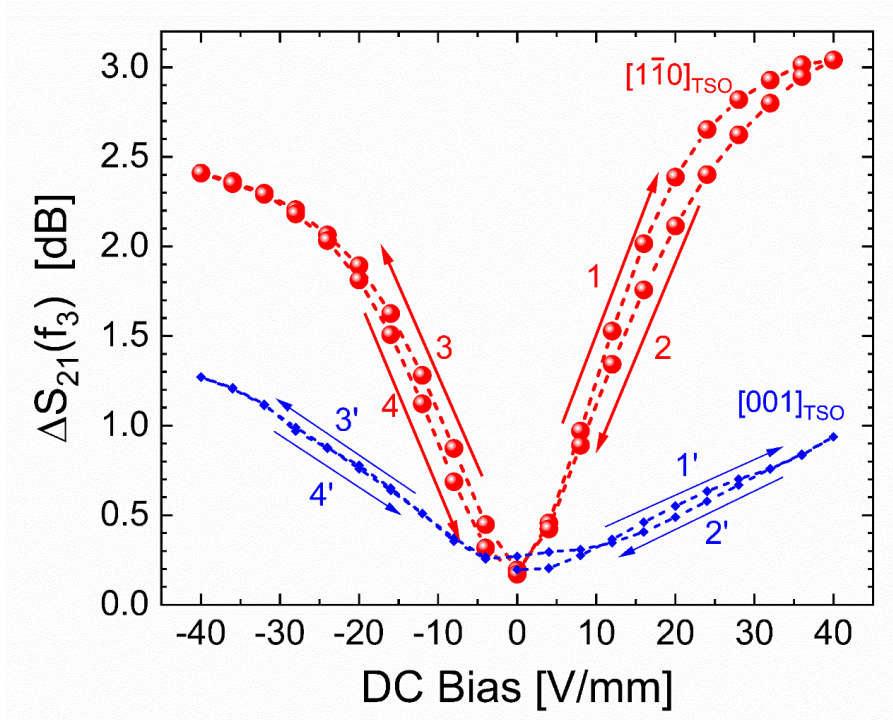


Figure 6.7. DC-bias dependence of the SAW intensity for a 25 nm-thick  $K_{0.7}Na_{0.3}NbO_3$  film on  $TbScO_3$  (DP\_1303 TSO) measured along  $[1\bar{1}0]_{TSO}$ , and  $[001]_{TSO}$  direction at room temperature.

To investigate the anisotropic behavior, the bias dependence of SAW intensity has been measured along  $[1\bar{1}0]_{TSO}$ , and  $[001]_{TSO}$  direction (see Fig. 6.7). The DC bias dependence of the SAW intensity shows a similar behavior along  $[1\bar{1}0]_{TSO}$  and  $[001]_{TSO}$  direction. However, the SAW intensity along  $[1\bar{1}0]_{TSO}$  is 1.8 to 3.2 times stronger than that along the  $[001]_{TSO}$  direction, indicating an anisotropy that is analogous to that in MOCVD samples without E-tuning.

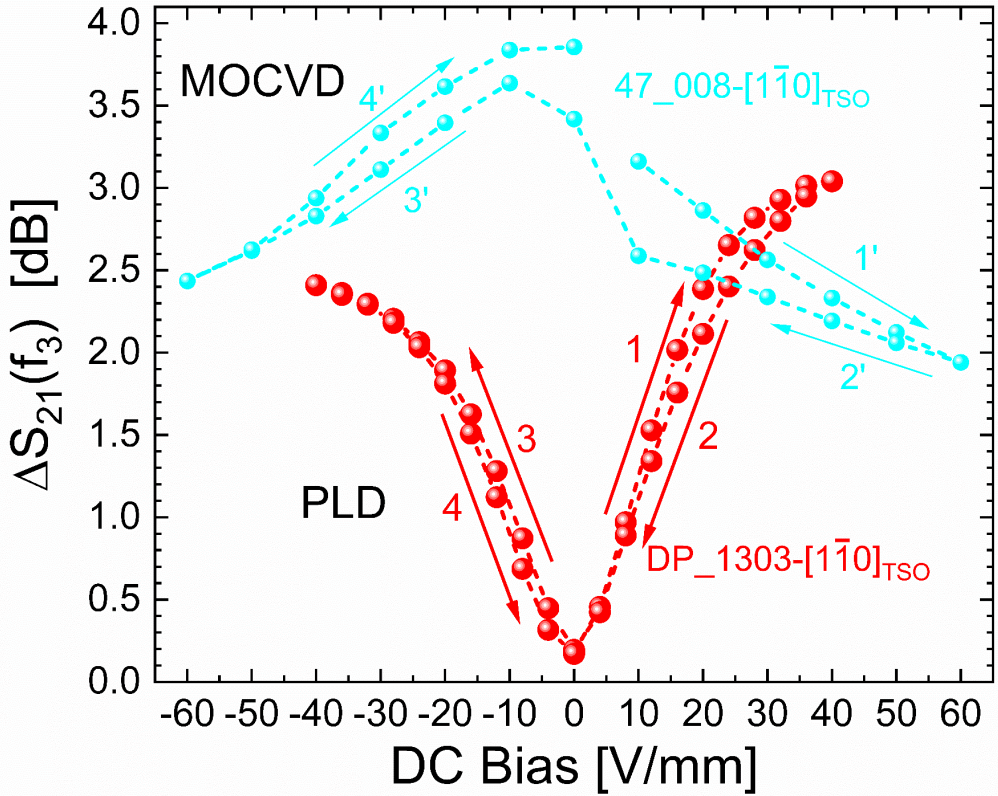


Figure 6.8. Comparison of the DC-bias dependence of the SAW intensity for a PLD sample (DP\_1303 TSO) and a MOCVD sample (47\_008 TSO) measured along  $[1\bar{1}0]_{\text{TSO}}$  direction at room temperature.

Finally, the bias dependence of the SAW intensity has been compared for PLD and MOCVD samples. Fig. 6.8 shows the bias dependence of the SAW intensity for a PLD (red symbols) and a MOCVD sample (cyan symbols) for the  $[1\bar{1}0]_{\text{TSO}}$  direction. In contrast to PLD sample, the bias has a negative effect on the SAW intensity of the MOCVD sample. As discussed before, the MOCVD sample represents a conventional ferroelectric, it means a more ordered state and absence of PNRs. With an applied DC bias, the DC electric field actually restrains the motion of dipoles under DC field, i.e. the electromechanical response is weakened by the application of DC field, resulting the observed decreased SAW intensity.

### 6.3 PNR-model for DC bias tuning

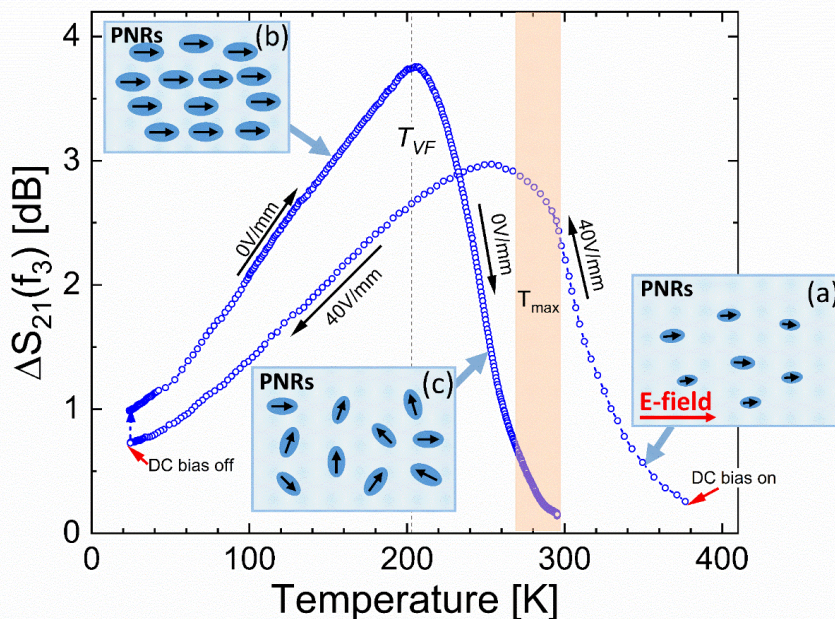


Figure 6.9. Temperature dependence of SAW intensity for a 25 nm-thick  $K_{0.7}Na_{0.3}NbO_3$  film on  $TbScO_3$  (DP\_1303 TSO). First the sample is cooled from 400 K to 20 K with a DC bias of 40 V/mm, then the DC E-field is removed at the minimum temperature of  $\sim 20$  K, and finally the sample is heated up to room temperature again. The schematics illustrate the evolution of PNRs orientation for the different states.

To further understand the mechanism of DC bias effect, the temperature dependence of SAW intensity with the presence of DC bias is investigated. Fig. 6.9 shows the temperature dependence of the SAW signal for the 25 nm-thick KNN film. Starting in the paraelectric phase ( $T \gg T_{max}$ ), no SAW signal can be detected without DC bias. An SAW signal only becomes visible after the DC bias is switched on (here 40 V/mm at  $\sim 380$  K). In terms of our explanation, this indicates that there are still a few PNRs at this temperature and that the polarization vectors of the normally randomly distributed and highly mobile PNRs will be oriented by the DC field, resulting in an ordered state (see inset (a) of Fig. 6.9) and a detectable SAW signal (e.g.  $\sim 0.2$  dB at 380 K). Upon cooling, the size and amount of PNRs, and thus the SAW signal, increase. At 253.6 K, slightly below the phase-transition temperature, the SAW signal reaches a first maximum of 2.97 dB. At even lower temperatures, the PNRs start to freeze, i.e. they become immobile. As a result of the reduced mobility of the PNRs, the SAW signal strength decreases. At the lowest temperature (here  $\sim 20$  K), we remove the DC bias. This removal of the field leads to a sudden increase of the SAW signal. At this temperature clearly below  $T_{VF}$ , it is expected that the ordered state of PNRs is preserved. However, tiny rearrangements of

the PNRs might still be possible. By removing the restriction imposed by the DC field on the oriented PNRs, these small changes might be responsible for the significant increase of the SAW signal (we will see this *release mechanism* again in Fig. 6.10).

Upon heating, now without the DC field, the SAW intensity increases due to the increasing mobility of the PNRs. It reaches a maximum at approximately  $T_{VF}$  ( $\Delta S_{21}(f_3) \approx 3.8$  dB). In the temperature regime below  $T_{VF}$ , the SAW intensity is significantly higher than during cooling with the DC bias. This again can be attributed to the above-described *release mechanism*. Above the freezing temperature  $T_{VF}$ , the PNRs are no longer immobile, and the thermal motion leads to an order-disorder transition for the relaxor (inset (c) of Fig. 6.9). As a consequence, the SAW intensity drops precipitously and can no longer be detected above room temperature.

Finally, we investigated the dynamic of the bias release and relaxation of the PNRs. For this purpose, the sample is first heated to approx. 380 K and then cooled to a given temperature while applying a DC bias of 40 V/mm. After stabilizing at a given temperature, the bias is removed and the SAW signal is recorded for 1 hour. Fig. 6.10 shows the resulting development of the SAW signal for different temperatures. Generally, we observe:

- (i) An initial sudden and significant increase of the signal (first data point recorded after  $\sim 5$  s),
- (ii) followed by a more gentle increase towards
- (iii) a maximum in  $\Delta S_{21}$  (at time  $t_{peak}$ ), and
- (iv) henceforth a decrease of the SAW signal.

The dynamics of the process strongly depend on the temperature. At low temperatures ( $T < T_{VF}$ , Fig. 6.10(a)), we do not reach the maximum in  $\Delta S_{21}$  within the measuring time. At  $T_{VF}$  the maximum is reached after  $t_{peak} \approx 0.6$  h, whereas for 220 K and 270 K the peak is observed at  $\sim 1$  min and  $\sim 5$  s, respectively. The subsequent decrease in signal strength behaves similarly. It starts gently at low temperatures and becomes more rapid as the temperature increases.

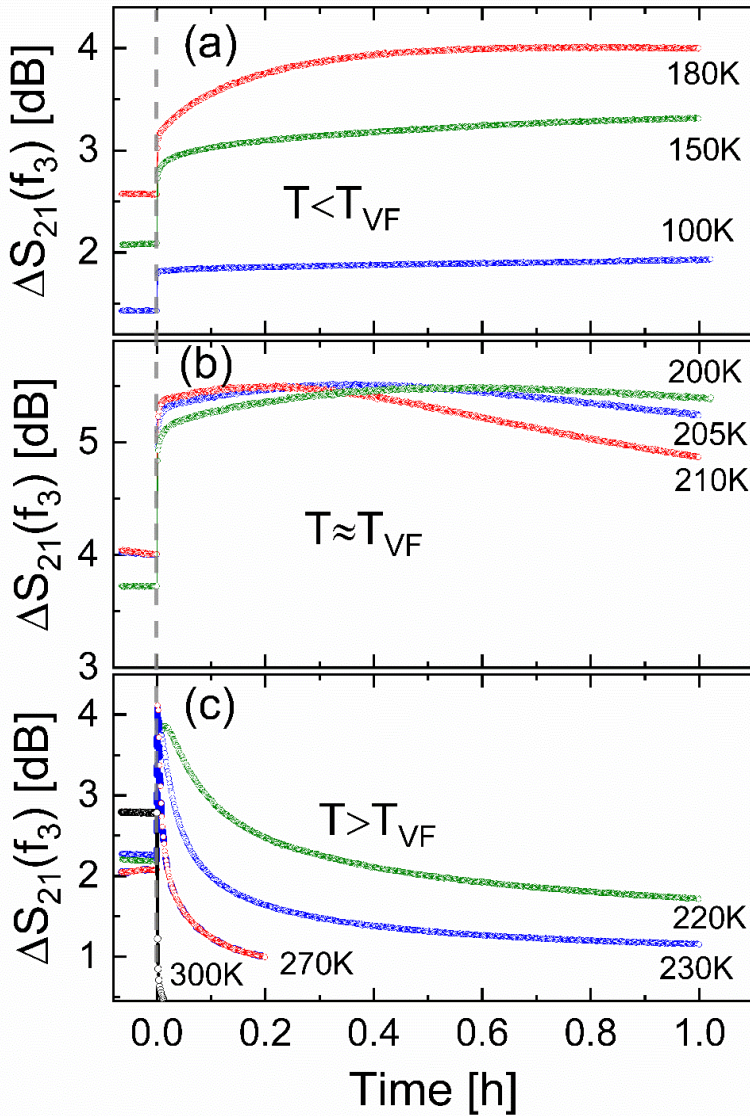


Figure 6.10. Time dependence of the SAW signal after removing the DC bias (40 V/mm) at  $t=0$  for different temperatures for (a)  $T < T_{VF}$ , (b)  $T \approx T_{VF}$ , and (c)  $T > T_{VF}$ . Prior to each experiment, the sample was heated to an elevated temperature (380 K), and subsequently cooled to a given temperature with an applied DC bias.

Especially at higher temperatures (see curves for  $T > T_{VF}$  in Fig. 6.10(c)), a typical relaxation behavior towards a finite value can be observed. An exponential fit of this part of the curve (for  $t > t_{peak}$ ) provides a characteristic relaxation time  $\tau$  of the relaxation process.

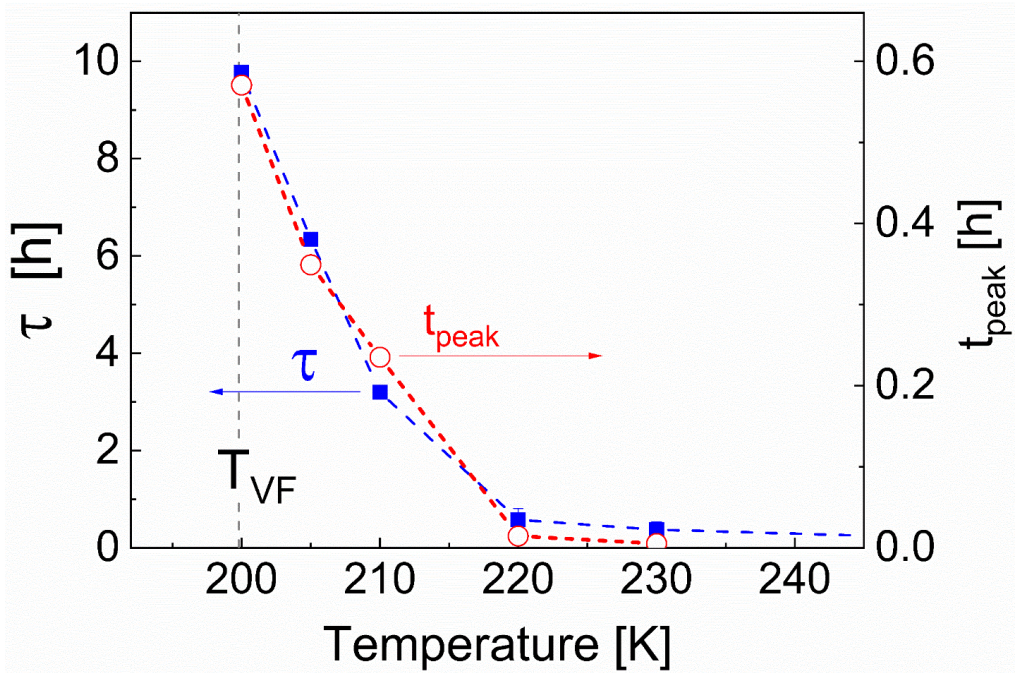


Figure 6.11. Temperature dependence of the relaxation time  $\tau$  that describes the exponential decay of the SAW signal and  $t_{peak}$  that indicates the time needed to reach the peak of SAW signal after the release of the electric field.

Fig. 6.11 shows the temperature dependence of  $\tau$  and  $t_{peak}$ . First, the relaxation time seems to be correlated to the freezing process of the PNRs. Far above the freezing temperature  $T_{VF}$ , it is extremely small (e.g.  $\tau(270\text{ K}) \approx 150\text{ s}$ ), and very close to  $T_{VF}$  it rapidly (exponentially) increases (e.g. from  $\tau(230\text{ K}) \approx 22\text{ min}$  to  $\tau(200\text{ K}) \approx 9.8\text{ h}$ ). Below  $T_{VF}$  the relaxation is no longer recorded. Second,  $t_{peak}$  shows a very similar temperature dependence, i.e. it increases rapidly upon approaching the freezing temperature. Therefore, we conclude that, except for the initial jump in  $\Delta S_{21}$  (release mechanism), the further development of the SAW signal is caused by one and the same relaxation mechanism, which firstly ( $t < t_{peak}$ ) leads to an increase and then ( $t > t_{peak}$ ) to a decrease of  $\Delta S_{21}$ . The temperature dependence of  $\tau$  and  $t_{peak}$  indicates that this mechanism is based on the relaxation of PNRs, i.e. a consequence of the relaxor-type behavior of the film.

## 6.4 Summary

In this chapter, the relaxor-type ferroelectric behavior of PLD samples have been discussed and a novel electronic tuning of the SAW signal is introduced. The major results are:

- (i) The PLD-prepared DP\_1303 TSO sample exhibits very weak (hardly visible) SAW at RT without the application of DC bias.
- (ii) However, the relaxor-type behavior of the PLD samples allows a novel electronic tuning of the SAW signal. A simple DC bias can reversibly boost the signal up to  $\sim 4$  dB (for 40 V/mm), which makes it comparable to the MOCVD samples.
- (iii) The novel E-tuning is explained by the behaviors of PNRs. At temperatures below the freezing temperature for PNR motion, the strong SAW signal can be preserved, and can even be enhanced due to a release of the electronically fixed PNR. At elevated temperatures, a reversible switching of the SAW signal is possible. The switching shows relaxation dynamics that are typical for relaxor ferroelectrics. The relaxation time  $\tau$  decreases exponentially from several hours at the freezing temperature to a few seconds at room temperature.

The use of epitaxially strained relaxor-type ferroelectric films could represent a novel option for the development of electronically tunable SAW devices.

## 7 KNN thin film gas-phase SAW sensor

In this chapter we describe a first test of thin KNN films in a SAW sensor application. For this purpose, we developed a setup consisting of carrier on a vacuum flanch, which allows to monitor the organic molecules in the gas phase. This setup was tested in a deposition device designed for the gas phase deposition of organic molecular monolayers. After a brief description of the deposition setup, design, working mechanism and sensitivity of the SAW gas phase sensor are discussed in this chapter.

### 7.1 MLD sensor system

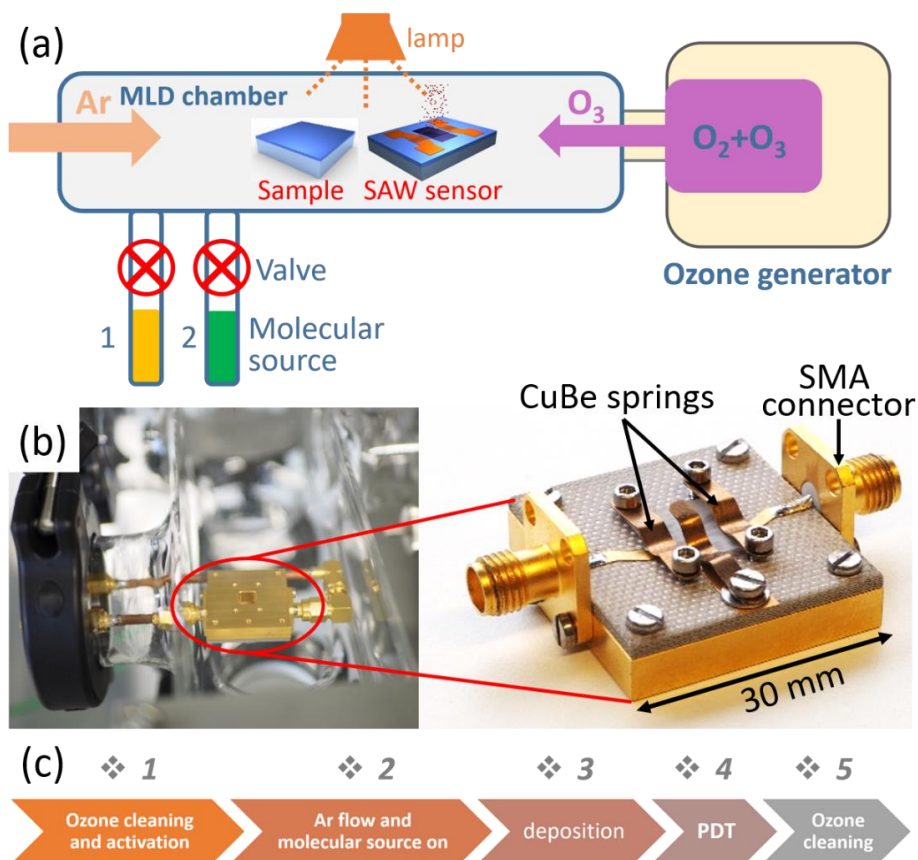


Figure 7.1. (a) Schematic of the molecular layer deposition (MLD) sensor system. Samples and SAW sensor are placed in the center of the MLD chamber which is connected with the molecular sources, an optical heater is applied on top of the chamber to control the deposition temperature, an Ar flow is applied to control the pressure in the chamber. (b) Picture of a MLD compatible sensor carrier, the rigid HF cables connect the carrier to the vacuum flanch via the SMA connectors. The SAW sensor is mounted on the carrier by CuBe springs and then inserted into the chamber to monitor the deposition. (c) Work flow of an intact MLD process, "PDT" represents "post-deposition treatment".

Fig. 7.1 (a) schematically illustrates the structure of the molecular layer deposition (MLD) sensor system. The molecular deposition is conducted in a MLD chamber which is connected with various molecular sources (e.g. APTES and GLYMO). The molecular sources are controlled via manual valves. In order to insert the SAW sensor into the chamber to monitor the deposition, I developed a sensor carrier together with the Master student D. Finck [110], which is compatible with the MLD system, as shown in Fig. 7.1(b). The HF cables are used to connect the carrier to the vacuum flanch via SMA connectors, which not only support the carrier but also allow access to the HF signal. The SAW sensor is mounted on the carrier by CuBe springs to get a stable contact between the IDTs and the HF cables on the carrier. Note that the structure of the IDTs has to be designed to fit to the positions of the HF cables on the carrier to get access to the high frequency signal. During deposition, the samples and SAW sensor are placed in the center of the chamber, the deposition temperature is controlled by an optical heater placed on top of the MLD chamber, the deposition pressure is adjusted by the flow of Ar gas. An ozone generator (a commercial microwave) is connected with the MLD chamber to provide ozone to clean and activate the surface of the SAW sensor and samples.

Fig. 7.1(c) shows the work flow of a typical MLD process:

- (i) Firstly, before deposition, the surface of the SAW sensor has to be cleaned and activated by the ozone which is generated by a commercial microwave. The aim of the ozone activation is to create hydroxyl groups on the surface of the oxides to get covalent bond with the head group of the silane molecules (e.g. APTES and GLYMO).
- (ii) Secondly, after the ozone activation, the oxygen is pumped out of the MLD chamber, the Ar flows in to provide a proper pressure (typically 0.1 -1 mbar for APTES and GLYMO deposition) and an inert gas environment for molecular deposition.
- (iii) Thirdly, when the chamber pressure is stable, the valve of the molecular source will be opened for deposition. In general, the deposition lasts for ~ 10 min for APTES and ~ 1 h for GLYMO. During the deposition, the center frequency shift of the SAW sensor will be recorded to monitor the deposition.
- (iv) Then after the deposition, the samples will stay in the vacuum chamber for hours to get rid of the physically absorbed layers on the surface, which is called post-deposition treatment (PDT).
- (v) Finally, the SAW and the MLD chamber will be cleaned by the ozone plasma again to get prepared for the next round of deposition.

For the first test of the sensor with a KNN film, a 27 nm-thick MOCVD sample on GdScO<sub>3</sub> (47\_008 GSO) has been chosen since:

- (i) we observed a reasonable large SAW signal for this sample (see Fig. 7.2(a)),
- (ii) the two harmonics (3<sup>rd</sup> and 5<sup>th</sup>) are clearly visible and can be used simultaneously to monitor a gas loading (see Fig. 7.2(b) and (c)), and

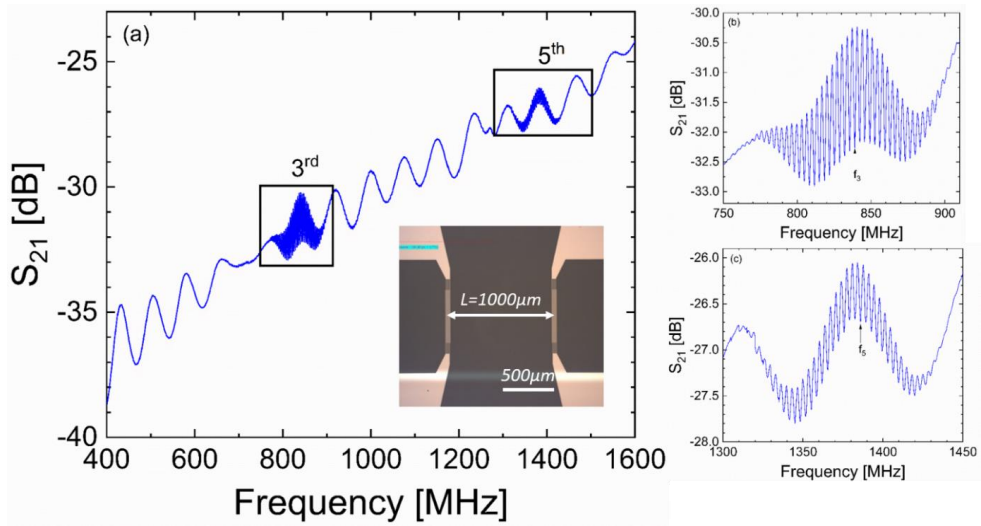


Figure 7.2. Frequency dependence of the transmission signal of a SAW structure with  $\lambda = 12 \mu\text{m}$  and  $L = 1000 \mu\text{m}$  (see inset) on a 27 nm-thick  $\text{K}_{0.7}\text{Na}_{0.3}\text{NbO}_3$  film on  $\text{GdScO}_3$  (47\_008 GSO)) measured at room temperature along  $[001]_{\text{GSO}}$  direction and detailed plots of the signal at the 3<sup>rd</sup> and 5<sup>th</sup> harmonic (center frequency indicated by arrows).

- (iii) the SAW signal are visible up to elevated temperature ( $T \approx 370 \text{ K}$ , see Fig. 7.3) which allow sensing at higher deposition temperatures often used for MLD process.

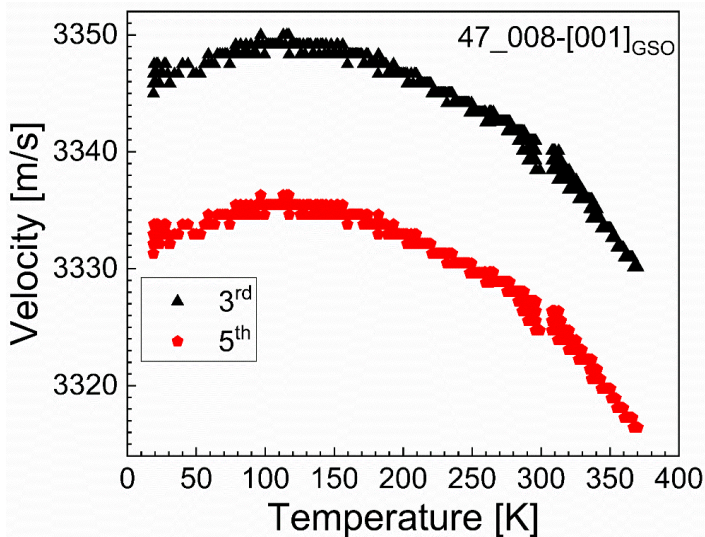


Figure 7.3. Temperature dependence of the SAW velocity at the 3<sup>rd</sup> and 5<sup>th</sup> harmonic for the sample 47\_008 GSO along  $[001]_{\text{GSO}}$  direction.

- (iv) Moreover, we enlarged the delay line of the SAW design from  $L = 500 \mu\text{m}$  to  $1000 \mu\text{m}$  (see inset Fig. 7.2(a)) which automatically modifies the interference pattern and, thus, improves the sensitivity of the sensor.

The 47\_008 GSO sample is mounted on the MLD-chamber compatible sensor carrier (see Fig. 7.1(b)) for the in situ detection of molecules during MLD deposition. The in situ detection is based on the absorption and desorption of molecules on the sensor surface (especially the delay line) and operates in terms of a mass loading sensor. The mass loading affects the velocity of the SAW (see also chapter 2.3) which results in a change in the frequency response:

$$\frac{\Delta f_n}{f_n} = \frac{\Delta v}{v_0} \quad (7.1)$$

where  $v_0$  and  $f_n$  represent the velocity and frequency for the  $n^{\text{th}}$  harmonic with mass loading which are simply given by:

$$v_n = \frac{\lambda f_n}{n} \quad (7.2)$$

By recording the shift of the interference pattern we obtain a sensitive measure for the change of the frequency (see Fig. 7.4).

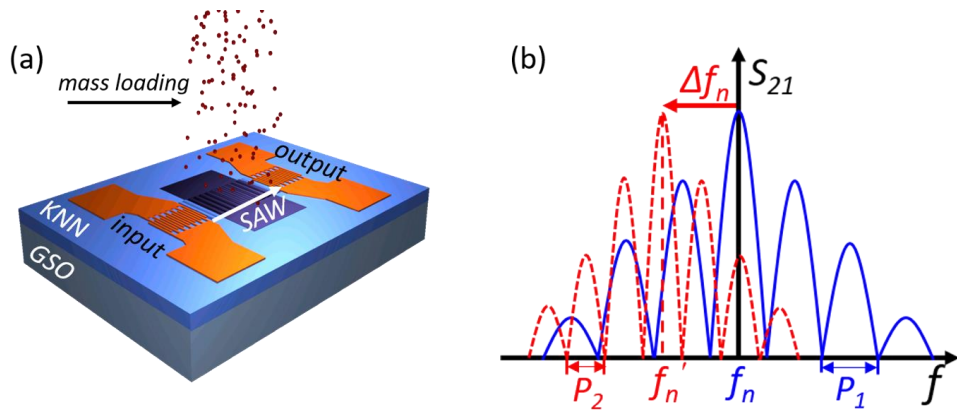


Figure 7.4. (a) Schematic of the mass loading during MLD and (b) the resulting shift of the interference pattern.

Therefore, qualitatively, there are mainly two parameters that will result in the shift of the center frequency during deposition:

- (i) Mass loading (see also chapter 2.3, e.g. Sauerbrey equation) which will lead to a decrease of the operation frequency, the removing of the surface mass will result in an increased center frequency.

- (ii) Temperature also has to be considered (see Fig. 7.3) The SAW velocity decreases as temperature increases. Consequently, the center frequency will shift to a lower value if the temperature increases and to a higher value if the temperature decrease.

Fig. 7.5 shows a typical MLD process used for the deposition of an organic silane layer. We will analyze the complex process step by step and show that the SAW sensor can play an important role for the whole series of deposition process steps.

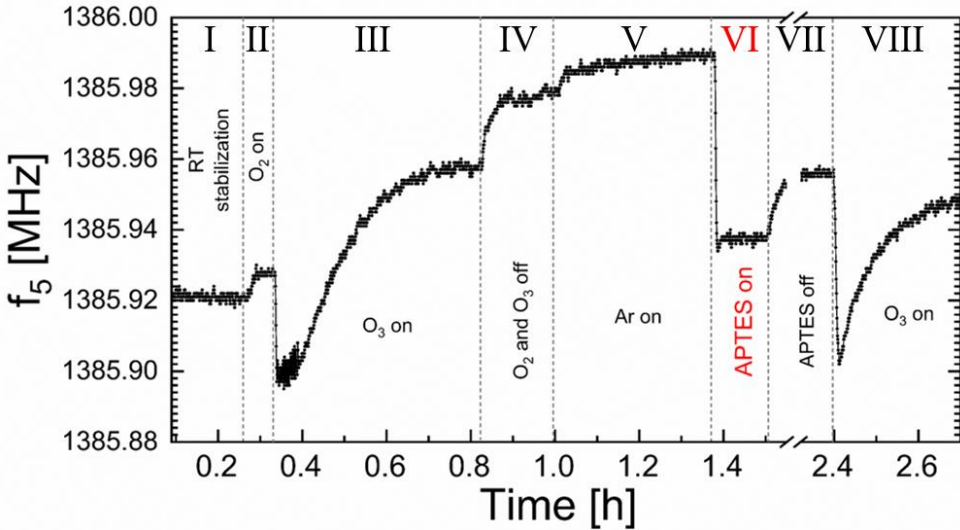


Figure 7.5. Example of the operation of the SAW sensor at the 5<sup>th</sup> harmonic for a MLD of APTES monitoring. The MLD process consists of the following major steps: (i) RT stabilization, (iii) ozone cleaning and activation, (iv) APTES deposition, and (vii) post deposition treatment.

In general, the MLD process shown in Fig. 7.5 can be divided into the 3 parts pre-deposition, deposition, and post-deposition:

- (i) **Pre-deposition.** This part is composed of 5 steps I to V in Fig. 7.5. Firstly, the complete setup including the SAW sensor needs to be stabilized at the operation temperature (here RT) to provide a stable center frequency before deposition. Then an O<sub>2</sub> flow is established for the generation of ozone (step II). Since the temperature of O<sub>2</sub> flow is lower than that of the sensor, the sensor surface will be slightly cooled, resulting in slight increase of the center frequency. When the ozone is generated (see III), the sensor temperature increases, resulting in an initial decrease of  $f_5$ . The ozone is used to clean the surfaces (device, substrates and sensor) and facilitate the binding of the APTES molecule to the surfaces. Therefore, the surface mass load will be removed and after the initial decrease the center frequency starts to increase again (see III). After the thorough cleaning, O<sub>2</sub> is pumped out of the chamber, leading to a decrease of the

temperature (increase of the center frequency, see step IV). In order to provide a proper process pressure (we typically use an Ar pressure of 0.1 - 1 mbar) for the deposition of molecules, a suitable Ar flow is established (step V). Before opening the vessel of the molecule sources, the system is again stabilized in the Ar flow until it is stable.

The pre-deposition process (5 steps) is important for the deposition and complex. As a consequence, the trace of the SAW sensor seems to be complicated. However, as described above, it can be understood and reflect the different process step well. Although we could not get to a quantitative interpretation yet, it turned out to be very helpful for the control of the pre-deposition process.

- (ii) **Deposition.** After the stabilization of the operation frequency, the vessel of the molecular source is opened for the actual deposition (see step VI in Fig. 7.5). The mass loading of the molecule (in this case, APTES) on the sample surface during deposition causes a decrease of operating frequency. A detailed plot is shown in Fig. 7.6. The moment the APTES source is open, the center frequency starts to decrease, indicating the mass loading. The signal stabilizes at certain value when absorption and desorption get into balance. The actual deposition step lasts for  $\sim 10$  min,  $f_5$  shifts by  $-0.055$  MHz. A quantitative analysis of this frequency drop is given later.

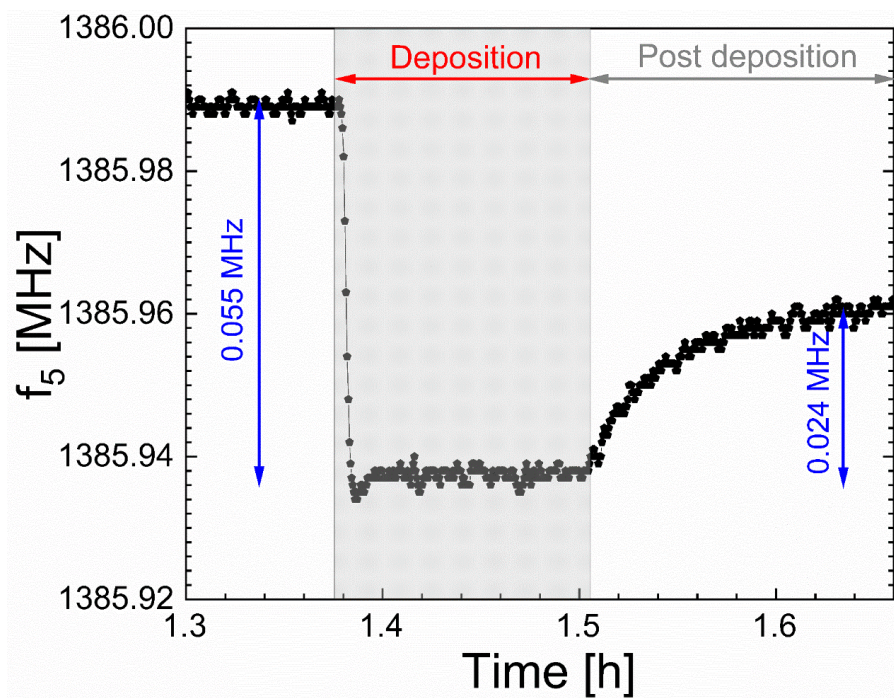


Figure 7.6. The shift of the center frequency  $f_5$  during actual APTES deposition monitored by the SAW sensor operated at the 5<sup>th</sup> harmonic.

(iii) **Post-deposition.** The molecule source is turned off after deposition (step VII). Without the continuous supply of molecular, the molecular layer that is physically absorbed on the surface is pumped away. As a result, the center frequency starts to recover to a higher value and reaches a new balance. Fig. 7.6 indicates that the center frequency increases by 0.024 MHz after the source of APTES is switched off. This step VII is usually the last step for the deposition of APTES (silanization). However, in order to reset the sensor we added step VIII to remove the molecule from the sensor. In this step the sensor surface (and the whole MLD setup) is cleaned by ozone for the next round. The center frequency starts to shift towards the original state.

In the next series of experiments we used the SAW sensor to monitor the organic molecule deposition simultaneously at two harmonics, i.e. 3<sup>rd</sup> and 5<sup>th</sup> harmonics. This could demonstrate different sensitivities, but also the slightly different mechanical coupling of the mass load at the different frequencies could be interesting.

For the deposition we used 2 different candidates APTES ((3-Aminopropyl)triethoxysilane) and GLYMO ((3-Glycidyloxypropyl)trimethoxysilane). APTES and GLYMO are the most commonly used silanes for covalent binding of organic films to metal oxides and potential formation of self-assembled monolayer (SAM). Some important material properties of APTES and GLYMO are listed in table 7.1.

Table 7.1. Parameters of the silanes APTES and GLYMO

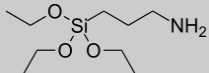
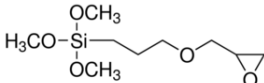
Molecule	Structural formula	Chemical formula	Density [g/mL]	Monolayer thickness [nm]
APTES		C <sub>9</sub> H <sub>23</sub> NO <sub>3</sub> Si	0.946	0.7[104]
GLYMO		C <sub>9</sub> H <sub>20</sub> O <sub>5</sub> Si	1.07	0.3[104]

Fig. 7.7 shows the simultaneously recorded drop of the center frequency  $f_3$  and  $f_5$  during deposition of APTES and GLYMO. The center frequencies drop by -15.6 KHz and -55 KHz for APTES deposition and -9.6 KHz and -35 KHz for GLYMO deposition for 3<sup>rd</sup> and 5<sup>th</sup> harmonic, respectively.

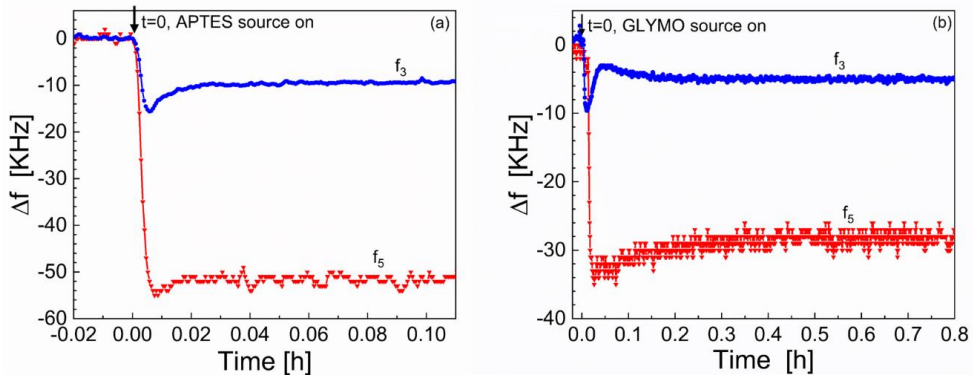


Figure 7.7. SAW sensor operating at 3<sup>rd</sup> and 5<sup>th</sup> harmonic for in situ detection of (a) APTES and (b) GLYMO deposition. The moment the molecule source is opened is defined as time zero.

The figure reveals a number of interesting aspects:

- (i) The SAW sensor seems to exhibit extremely high sensitivity. Although we could not prove that a monolayer (maybe even a SAM) is formed immediately, the drop and subsequent release of the SAW signal during deposition and post-deposition shown in Fig. 7.6 indicate that the effective film thickness is only slightly larger (30 – 50%) than a monolayer. Therefore, assuming a film thickness of a monolayer APTES or GLYMO (i.e. 0.7 nm or 0.3 nm, see table (7.1)) would result in sensor sensitivities

$$S = \frac{\Delta f}{\Delta h} \quad (7.3)$$

where  $\Delta f$  is the shift of center frequency, and  $\Delta h$  is the thickness of molecular layer, of the SAW sensor of  $S_3 \approx -22.3 \text{ KHz} / \text{nm}$  and  $S_5 \approx -78.6 \text{ KHz} / \text{nm}$  for APTES and  $S_3 \approx -32 \text{ KHz} / \text{nm}$  and  $S_5 \approx -116.7 \text{ KHz} / \text{nm}$  for GLYMO. Since the resolution of the signal analyzer (keithley 2920) is  $\sim 200 \text{ Hz}$ , a detection limit of 0.009 nm (3<sup>rd</sup>) and 0.0025 nm (5<sup>th</sup>) can be expected for APTES deposition, while the detection limits for GLYMO deposition are 0.006 nm (3<sup>rd</sup>) and 0.0017 nm (5<sup>th</sup>).

- (ii) The center frequency increases with the order of the harmonic. As introduced in chapter 2.3, the sensitivity of the sensor depends strongly on the frequency. It can be described by:

$$\Delta f = -c_s \frac{\Delta m f_0^2}{A} = -c_s \rho \Delta h f_0^2 \quad (7.4)$$

where  $c_s$  is a constant which describes the sensing system,  $\rho$  is the density of the deposited molecule, and  $A$  is the sensing area. Therefore, the shift of the center frequency is expected to be proportional to the square of the operation frequency. The sensitivity of our sensor should therefore show a  $(5/3)^2 \approx 2.8$  times higher sensitivity at

the 5<sup>th</sup> harmonic compared to the 3<sup>rd</sup> harmonic. Experimentally, we observe  $S_5/S_3 = 3.52$  and  $3.65$  for APTES and GLYMO deposition, respectively, which is in reasonable agreement with the theoretical prediction. It also implies that the sensitivity of the system could be further improved by measuring at even higher orders of harmonics (7<sup>th</sup>, or 9<sup>th</sup>).

The sensor characteristic constant  $c_s$  can be evaluated by a linear fit of  $\Delta f$  as function of  $\rho\Delta h f_0^2$ . Assuming again a monolayer thickness we get a perfect linear behavior of all experimental data (see Fig. 7.8). The slope of the fitted line yields a sensor constant of  $c_s = (0.0446 \pm 0.0036) \text{ m}^2/\text{Kg}\cdot\text{MHz}$ . This constant can be applied to evaluate the thickness of the layers that are deposited at various conditions, which will be discussed in the next subchapter.

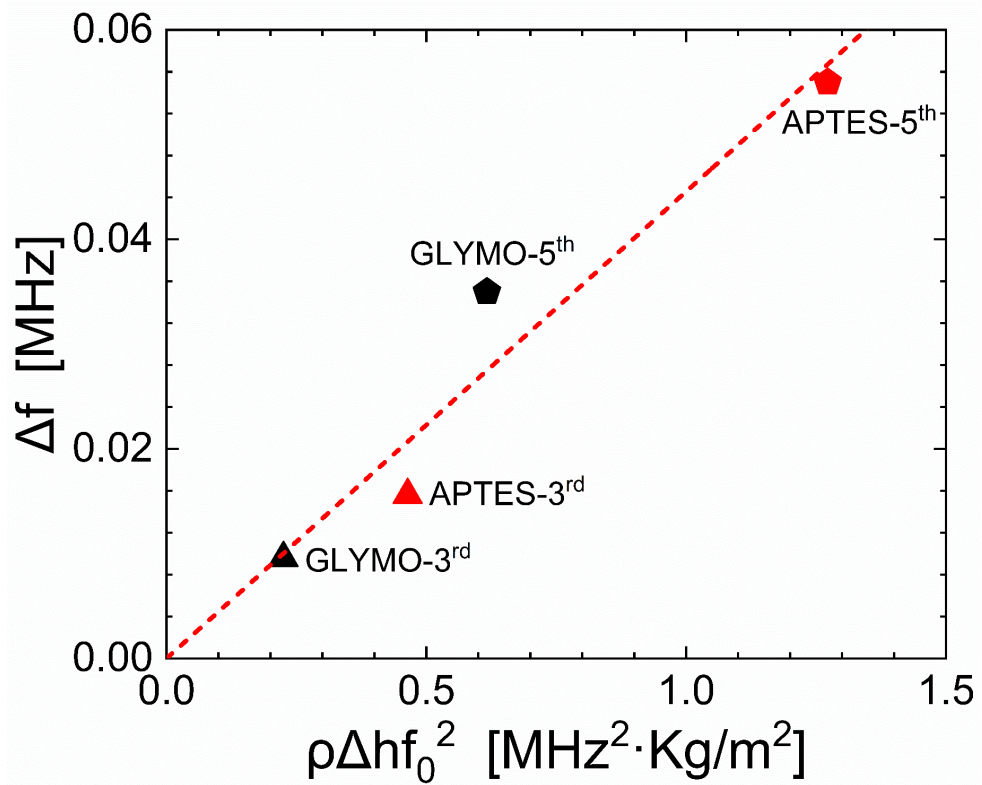


Figure 7.8. Shift of center frequency as function of  $\rho\Delta h f_0^2$  for APTES and GLYMO deposition measured at 3<sup>rd</sup> and 5<sup>th</sup> harmonic shown in Fig. 7.7. The linear fit (red dashed line) of the data yields the sensor constant of  $c_s = 0.0446 \pm 0.0036 \text{ m}^2/\text{Kg}\cdot\text{MHz}$ .

## 7.2 SAW sensor operation at elevated MLD temperature

In order to further demonstrate the use of the SAW sensor for MLD process, APTES has been deposited at various elevated temperature in the presence of the SAW sensor device based on sample 47\_008 GSO. The shift of the center frequency at the 3<sup>rd</sup> and 5<sup>th</sup> harmonics has been simultaneously recorded during the whole deposition process, as shown in Fig. 7.9. Again the moment that the APTES source is opened is defined as zero time. The shift of the frequency at the 3<sup>rd</sup> harmonic (see Fig. 7.9(a)) lies in the regime of -16.2 to -8.6 KHz, whereas that of the 5<sup>th</sup> harmonic (see Fig. 7.9(b)) is in the regime of -55 to -21 KHz.

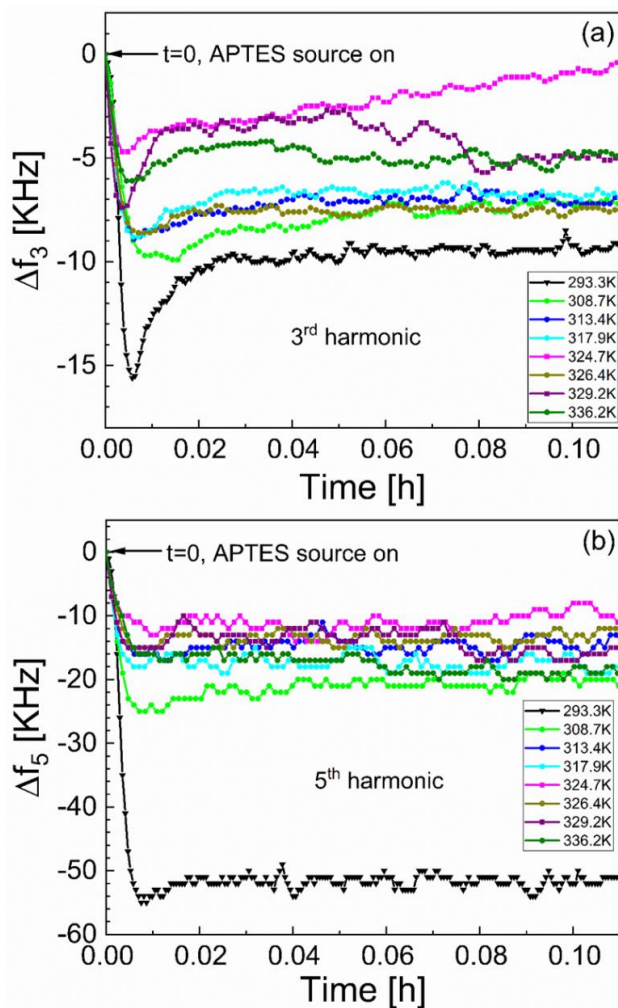


Figure 7.9. Shift of the center frequency during APTES deposition for different deposition temperatures monitored by a SAW sensor based on a 27 nm-thick  $K_{0.7}Na_{0.3}NbO_3$  on  $GdScO_3$  (47\_008 GSO) operating at (a) 3<sup>rd</sup> harmonic and (b) 5<sup>th</sup> harmonic.

The resulting temperature dependence of the shift of the center frequency is summarized in Fig. 7.10(a). It indicates a couple of interesting points:

- (i) The deposition at RT exhibits the largest shift of center frequency. It means that the mass loading on SAW sensor is largest at RT. This could be due to larger amount of APTES molecules are physically absorbed leading to larger thickness layer than a monolayer.
- (ii) As the deposition temperature increases (from RT to  $\sim 325$  K), the shift of the center frequency decreases, indicating less mass loading on the SAW sensor. This is reasonable because the physisorption at elevated temperature becomes less likely due to a large particle energy which can overcome the physical interaction (Van der Waals or electrostatic binding). However, the thermal energy might still be too small to allow a covalent binding of the APTES. The mass loading and therefore the shift of the center frequency decreases with temperature.
- (iii) A further increase of the temperature ( $T > 325$  K) on the one hand leads to a further decrease of physisorption, on the other hand, the energy is large enough to allow instantaneous binding of the APTES molecule. Therefore, the mass loading and therefore  $\Delta f$  start to increase and reaches a maximum at 326.4 K. At even higher temperature, the thermal energy of the particles is too large to allow any stable or temporary binding. It should even be, that molecules are destroyed at these temperatures. As a result,  $\Delta f$  starts to decrease again. The 3<sup>rd</sup> and 5<sup>th</sup> harmonics show the same behaviors of  $\Delta f$  vs  $T$ , whereas the shift of frequency at 3<sup>rd</sup> harmonic is smaller than that of the 5<sup>th</sup> harmonic.

It implies that in order to achieve a perfect covalently bonded monolayer of APTES maybe even a rapidly formed SAM of APTES, the optimum deposition temperature could be around 330 K. This optimum temperature of  $\sim 330$  K for SAM formation has actually reported by M. Glass [126] for GLYMO. Therefore, the SAW sensor can not only monitor the deposition process, but also facilitate the understanding and help modify the deposition process.

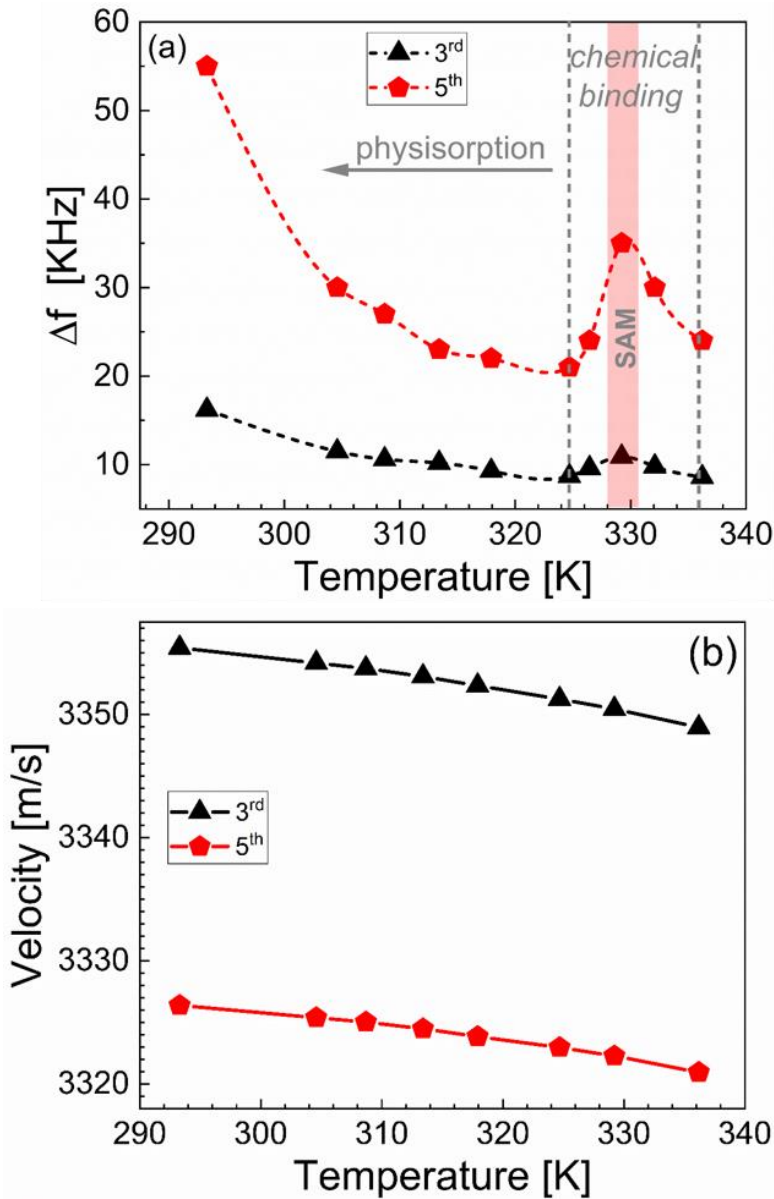


Figure 7.10. Temperature dependence of (a) the shift of center frequency at 3<sup>rd</sup> and 5<sup>th</sup> harmonics as a result of the APTES deposition at given temperature and (b) SAW velocity of the 3<sup>rd</sup> and 5<sup>th</sup> harmonic without mass load. The SAW velocity and therefore the operation frequency at both 3<sup>rd</sup> and 5<sup>th</sup> harmonics decrease as temperature increase, which shows a same trend as discussed in [chapter 5](#) for T-dependence of SAW velocity on 47\_008 GSO along different orientations. The frequency shift in (a) seems to verify the different temperature regimes of physisorption and chemical binding of APTES.

Taking the operation frequency and the  $\Delta f$  at each temperature point, together with the sensing system constant,  $c_s$ , evaluated in the last subchapter, the effective thickness of the deposited APTES layer can be evaluated from Eq. (7.4),

$$\Delta h = -\frac{\Delta f}{k\rho f_0^2} \quad (7.5)$$

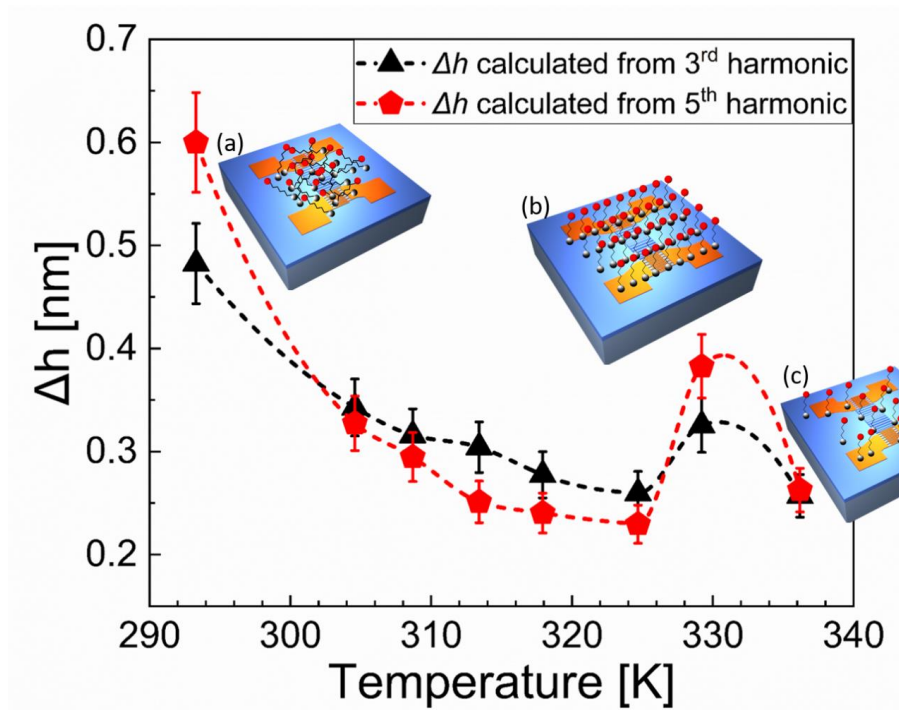


Figure 7.11. Thickness  $\Delta h$  of the APTES layers deposited at various temperatures on SAW sensor. The values are calculated from eq. (7.5) using the parameters of operation frequency,  $f_0$ , shift of center frequency  $\Delta f$ , density of APTES  $\rho$ , and sensing system constant  $c_s$ . Parameters collected at the 3<sup>rd</sup> and 5<sup>th</sup> harmonics and applied to evaluate  $\Delta h$ . The error of  $\Delta h$  is calculated from the error of  $c_s$  (error bars). The insets schematically illustrate (a) physically absorbed molecules at low temperatures, (b) covalently bonded molecules at elevated temperature, and (c) partially covalently bonded molecules at even higher temperatures.

The calculated thickness is shown in Fig. 7.11. Parameters at 3<sup>rd</sup> and 5<sup>th</sup> harmonics are used to evaluate  $\Delta h$  for both harmonics, plotted as black triangle and red pentagon, respectively. The APTES layer thickness first decreases from  $\sim 0.6$  nm at RT to  $\sim 0.2$  nm at 326 K, and then reaches a peak of  $\sim 0.4$  nm at around 330 K. Finally, the thickness starts to decrease again as the temperature further increased. The thickness values evaluated for both harmonics coincide quite well. The insets in Fig. 7.11 schematically illustrate the states of the deposited molecular layer on the surface. Inset (a) indicates that the molecules deposited on the surface

of SAW sensor are most likely physically absorbed, yielding a large thickness but will be desorbed in time. As temperature increases, the density of the physisorbed molecules decreases, whereas the density of covalently bonded molecules increases. An ideal completely covalently bonded case is shown in inset (b), corresponding maybe to the peak of  $\Delta h$  at  $\sim 330$  K. At even higher temperatures, the surface of the SAW sensor can only partially be bonded, as shown in inset (c) or molecules are even destroyed.

### 7.3 Summary

In this chapter, a thin film SAW sensor system has been developed based on the MOCVD KNN thin films. The operation mechanism, sensitivity, application at elevated temperature are illustrated and discussed. The major results are:

- (i) A gas-phase SAW sensor is developed based on KNN films. It has been successfully applied for in situ monitoring of molecular layer deposition.
- (ii) The sensitivity of the SAW sensor increases with the order of the SAW signal. A sensitivity of  $S_3 \approx -22.3$  KHz/nm and  $S_5 \approx -78.6$  KHz/nm is estimated for APTES deposition at 3<sup>rd</sup> and 5<sup>th</sup> harmonic, respectively. Analogously, a sensitivity of  $S_3 \approx -32$  KHz/nm and  $S_5 \approx -116.7$  KHz/nm is obtained for GLYMO deposition at 3<sup>rd</sup> and 5<sup>th</sup> harmonic, respectively.
- (iii) In comparison to SAW sensors, our KNN thin film sensor possesses an at least one order of magnitude higher sensitivity. This is most likely caused by the thinness of the thin film, the acoustic energy is more concentrated on the surface, which makes it more sensitive to surface perturbations.
- (iv) Furthermore, the in situ detection of APTES deposition via SAW sensor at elevated temperatures help understand, optimize and control the MLD process. For example, an optimum deposition temperature of  $\sim 330$  K for covalent binding of organic films was observed.

The demonstrated high sensitivity of our system compared to bulk SAW systems supports our idea of developing thin film SAW sensor systems for various applications ranging from monolayer deposition detection to highly selective and sensitive sensing of biological markers for e.g. disease diagnosis.

## 8 Conclusion

In this work, we demonstrated the potential of a SAW sensor system based on strained and extremely thin epitaxial KNN films. The basic ideas behind this novel concept are:

- (i) Due to the thinness of the piezoelectric layer (we used 30 nm thin films) the energy of the SAW is more concentrated at the surface of the device. According to our assumption this leads to a much higher sensitivity to any mass loading. Moreover, we noticed that this way higher harmonics are accessible which also enhance the sensitivity of the device.
- (ii) We used epitaxial strain to tailor the ferroelectric properties in a way that the SAW signal is highest at operation temperature (in our case RT to  $\sim 120^\circ\text{C}$ ). In the ideal case the strain shifts the phase transition towards the operation temperature.
- (iii) Finally we identified KNN an ideal candidate for the envisioned SAW sensor system.

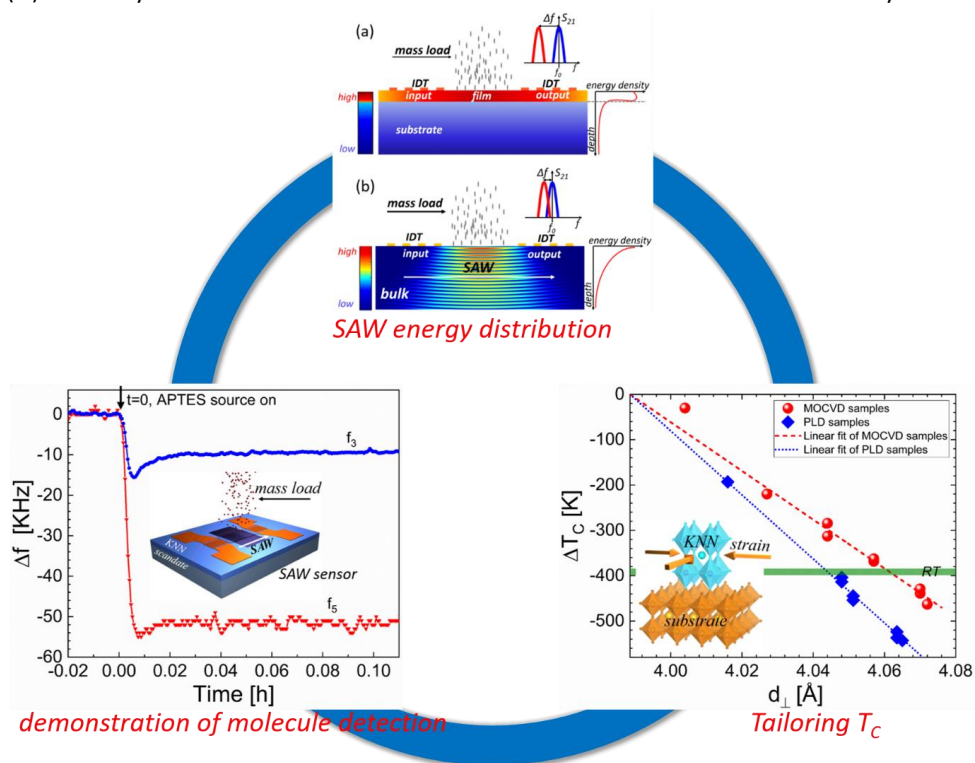


Figure 8.1. Schematics illustrate the novel concept and main achievements in this thesis. The schematic on the top illustrates the basic idea to develop SAW sensor based on thin film system. The SAW is more concentrated in the thin film system, this leads to a much higher sensitivity to any surface perturbation. Schematic bottom right illustrates the strain engineering of the ferroelectric properties in order to optimize the SAW signal at operation temperature and the schematic on the left shows the successful demonstration of gas-phase SAW sensor with extremely high sensitivity.

In detail, in order to develop the thin film SAW sensor systems, piezoelectric and ferroelectric properties of lead-free KNN films are tailored via epitaxial strain. Two deposition methods—MOCVD and PLD—are applied to deposit KNN on different scandate substrates (DSO, TSO, GSO, SSO) which introduce different amount of compressive strain. The MOCVD and PLD samples are characterized among others by XRD, AFM, and ToF-SIMS to analyze their structure, epitaxy, surface morphology, and composition. Lithography, metallization, and lift-off techniques are applied to prepare micro electrodes on the KNN films for the analysis of electric properties and the SAW device fabrication. In various cryoelectronic experiments, the electric properties of the KNN films, including the dielectric constants, phase transition temperature, SAW intensity, and SAW velocity are investigated. A first demonstrator gas-phase SAW sensor system based on the strain-tailored KNN films was built and tested. The major results are:

- (i) *Comparison of MOCVD and PLD samples.* The MOCVD-prepared KNN samples show perfect epitaxial growth with hardly any structural relaxation, as reported in Dr. Yang Dai's thesis [25]. In contrast, the PLD-prepared samples also show epitaxy, however, an onset of plastic relaxation is observed. The MOCVD samples exhibit typical conventional ferroelectric behaviors with hardly any frequency dispersion of the ferroelectric phase transition, whereas the PLD samples show textbook-like relaxor behavior with a broad and frequency dispersive ferroelectric phase transition. We believe that this is caused by the high particle energy during deposition which makes it more likely to create microscopic composition inhomogeneities which lead to the formation of polar nanoregions.
- (ii) *Effect of strain on the phase transition temperature.* The phase transition temperatures of MOCVD and PLD samples are all shifted to lower temperatures by the compressive strain. A "square model" is first used to investigate the strain dependence of the shift of the phase transition temperature. The MOCVD samples show a perfect linearity dependence of  $\Delta T_C$  vs strain, similar to the interpretation of Dr. Yang Dai [25]. However, the PLD samples show no clear dependence. In order to improve the model, a "normal lattice model" is proposed to evaluate the strain dependence of  $T_C$ . In the new model, the strain is represented by the vertical lattice parameter  $d_L$  of the KNN film. In this model,  $\Delta T_C$  of MOCVD and PLD samples show a perfect linear dependence of  $d_L$  (see Fig. 8.1). This supports our new model for description of the strain dependence of the phase transition temperature.
- (iii) *Dielectric properties.* The dielectric properties of strained KNN films are highly improved, e.g. a maximum permittivity of  $\epsilon'_{max} \approx 13695$  at  $\sim 330$  K and a RT permittivity of  $\epsilon'_{RT} \approx 5166$  are achieved for a 27 nm-thick  $K_{0.7}Na_{0.3}NbO_3$  film on TSO prepared by MOCVD compared to  $\epsilon'_{max} \approx 6400$  and  $\epsilon'_{RT} \approx 600$  for unstrained KNN, as reported in Dr. Yang Dai's thesis [25] and our common publication [111]. Moreover, an anisotropic behavior of the dielectric properties is observed, e.g. a ratio of the

permittivity measured along  $[1\bar{1}0]$  and  $[001]$  directions of the substrate  $\varepsilon'_{[1\bar{1}0]}/\varepsilon'_{[001]}=1.33$  and  $1.25$  are obtained for KNN films on TSO and GSO, respectively.

- (iv) *SAW properties.* The MOCVD samples show strong SAW at RT ( $\Delta S_{2f}$  up to  $\sim 4$  dB) which is even comparable to bulk  $\text{LiNbO}_3$  samples. Considering the thinness ( $\sim 30$  nm) of our film system and the fact that the electromechanical coupling coefficient  $K^2$  decreases significantly with the ratio  $h/\lambda$ , our KNN system is promising for tin film SAW applications. Moreover, high orders of odd harmonics can be generated with the 3<sup>rd</sup> harmonic showing the largest intensity. In contrast, the SAW signal in PLD samples is hardly visible. However, this situation changes significantly with the application of a DC bias. The SAW intensity increases from  $\sim 0.2$  dB for zero-bias to  $\sim 4$  dB at a DC bias of  $40$  V/mm. This strong SAW signal can be preserved and is even enhanced during release of the electronically fixed PNRs if the bias is removed. A model based on PNRs is proposed to explain the relaxor behavior of SAW in PLD samples.
- (v) *Thin film SAW sensor.* Finally, a gas-phase SAW sensor is developed based on KNN films. It has been successfully applied for in situ monitoring of molecular layer deposition (MLD). The sensitivity of the SAW sensor increases with the order of the SAW. A sensitivity of  $S_3 \approx -22.3$  KHz/nm and  $S_5 \approx -78.6$  KHz/nm is estimated for APTES deposition at 3<sup>rd</sup> and 5<sup>th</sup> harmonic, respectively. Analogously, a sensitivity of  $S_3 \approx -32$  KHz/nm and  $S_5 \approx -116.7$  KHz/nm is obtained for GLYMO deposition. In comparison, the SAW sensor based on KNN films seems to possess a sensitivity which is at least one order of magnitude higher than that of a comparable bulk  $\text{LiNbO}_3$  SAW sensor. This is believed to be caused by the thinness of the SAW system and the resulting concentration of the acoustic energy at the surface, which makes the sensor more sensitive to surface perturbation (see Fig. 8.1). Furthermore, we demonstrated that the in situ detection of APTES deposition via SAW sensor at elevated temperatures help understand the MLD mechanism and optimize deposition parameters.

In conclusion, the strain-engineered extremely thin KNN films showed very promising SAW sensor properties which implies potential applications ranging from in situ detection of monolayer deposition to environmental, biological or even medical applications like highly selective and sensitive sensing of bacteria, viruses, pathogens, or biological markers for disease diagnosis (e.g. point-of-care-testing (POCT)).

## References

- [1] C. C. W. Ruppel, IEEE Transactions on Ultrasonics, Ferroelectrics, and Frequency Control **64**, 1390 (2017).
- [2] Campbell C. (2012). *Surface Acoustic Wave Devices and Their Signal Processing Applications*. San Diego: Elsevier.
- [3] Hashimoto K. (2000). *Surface Acoustic Wave Devices in Telecommunications*. New York: Springer.
- [4] A. Winkler, R. Brünig, C. Faust, R. Weser, H. Schmidt, Sensors and Actuators A: Physical **247**, 259 (2016).
- [5] Y. Pan, N. Mu, B. Liu, B. Cao, W. Wang, L. Yang, Sensors **18**, 2977 (2018).
- [6] G. Lindner, Journal of Physics D: Applied Physics **41**, 123002 (2008).
- [7] X. G. Tian, H. Liu, L. Q. Tao, Y. Yang, H. Jiang, T. L. Ren, AIP Advances **6**, 095317 (2016).
- [8] Y. Li, M. Shao, B. Jiang, Measurement and Control **52**, 947 (2019).
- [9] D. B. Go, M. Z. Atashbar, Z. Ramshani, H. C. Chang, Anal. Methods **9**, 4112 (2017).
- [10] S. Okuda, T. Ono, Y. Kanai, T. Ikuta, M. Shimatani, S. Ogawa, K. Maehashi, K. Inoue, K. Matsumoto, ACS Sens. **3**, 200 (2018).
- [11] Ballantine D. S., White R. M., Martin S. I., Ricco A. J., Zellers E. T., Frye G. C., Wohltjen H. (1997). *Acoustic Wave Sensors Theory, Design, and Physico-Chemical Applications*. San Diego: Academic Press.
- [12] N. A. Pertsev, A. G. Zembilgotov, and A. K. Tagantsev, Phys. Rev. Lett. **80**, 1988 (1998).
- [13] N. A. Pertsev, A. K. Tagantsev, and N. Setter, Phys. Rev. B **61**, R825 (2000).
- [14] Y. Saito, H. Takao, T. Tani, T. Nonoyama, T. Takatori, T. Homma, T. Nagaya, and M. Nakamura, Nature **432**, 84 (2004).
- [15] J. Valasek, Phys. Rev. **17**, 475 (1921).
- [16] S. C. Chang, U. E. Avci, D. E. Nikonov, S. Manipatruni, I. A. Yong, Phys. Rev. Applied **9**, 014010 (2018).
- [17] Y. Lee, J. Park, S. Cho, Y. E. Shin, H. Lee, J. Kim, J. Myoung, S. Cho, S. Kang, C. Baig, H. Ko, ACS Nano **12**, 4045 (2018).
- [18] K. G Webber, M. Vögler, N. H khansur, B. Kaeswurm, J. E Daniels, F. H Schader, Smart Mater. Struct. **26**, 063001 (2017).
- [19] P. C. Yeh, H. Duan, T. K. Chung, Micromachines **10**, 710 (2019).

- [20] T. Mikolajick, S. Slesazeck, M. H. Park, U. Schroeder, MRS Bulletin **43**, 340 (2018).
- [21] L. Seixas, A. S. Rodin, A. Carvalho, A. H. Castro Neto, Phys. Rev. Lett. **116**, 206803 (2016).
- [22] Fujii S., Saitoh M. (2019). *Ferroelectricity in Doped Hafnium Oxide*. Tokyo: Elsevier, 437-444.
- [23] C. R. Bowen, H. A. Kim, P. M. Weaver, S. Dunn, Energy Environ. Sci. **7**, 25 (2014).
- [24] W. Känzig, Ferroelectrics **74**, 285 (1987).
- [25] Y. Dai, "Tailoring the Electronic Properties of Epitaxial Oxide Films via Strain for SAW and Neuromorphic Applications" Ph.D. dissertation, D **38** (Diss., Köln, Univ., 2017).
- [26] W. J. Merz, Phys. Rev. **76**, 1221 (1949).
- [27] G. Shirane, R. Newnham, and R. Pepinsky, Phys. Rev. **96**, 581 (1954).
- [28] Jaffe B., Cook W. R., and Jaffe H. L. (1971). *Piezoelectric Ceramics*. London and New York: Academic Press.
- [29] J. F. Li, K. Wang, F. Y. Zhu, L. Q. Cheng, F. Z. Yao, J. Am. Soc. **96**, 3677(2013).
- [30] Wanlin Zhu, Ichiro Fujii, Wei Ren, and Susan Trolier-McKinstry, J. Appl. Phys. **109**, 064105 (2011).
- [31] G. H. Haertling, J. Am. Ceram. Soc. **82**, 797 (1999).
- [32] M. W. Lufaso, and P. M. Woodward, Acta Cryst. B **57**, 725 (2001).
- [33] J. G. Bednorz and K. A. Muller, Phys. Rev. Lett. **52**, 2289 (1984).
- [34] C. Ang, Z. Yu, P. M. Vilarinho, and J. L. Baptista, Phys. Rev. B **57**, 7403 (1998).
- [35] H. Liu. "Growth and characterization of lead-free (K,Na)NbO<sub>3</sub>-based piezoelectric single Crystals", Ph.D dissertation, Material chemistry. University of Bordeaux, 2016.
- [36] Y. Guo, K. Kakimoto, H. Ohsato, Applied Physics Letters **85**, 4121 (2004).
- [37] D. Lin, Journal of Applied Physics **102**, 034102 (2007).
- [38] Z. Feng, S. W. Or, Journal of Alloys and Compounds **480**, 15 (2009).
- [39] Y. Chang, Z. Yang, Y. Hou, Z. Liu, Z. Wang, Applied Physics Letters **90**, 232905 (2007).
- [40] J. Wu, H. Tao, Y. Yuan, X. Lv, X. Wang, X. Lou, RSC Adv. **5**, 14575 (2015).
- [41] Y. S. Sung, J. H. Lee, S. W. Kim, T. H. Lee, J. M. Kim, J. H. Cho, T. K. Song, M. H. Kim, T. G. Park, Ceramics International **38S**, S301 (2012).
- [42] J. Schiemer, Y. Liu, M. Caroenter, R. Withers, Ferroelectrics **429-1**, 95 (2012).

- [43] Y. G. Lv, C. L. Wang, J. L. Zhang, L. Wu, M. L. Zhao, J. P. Xu, *Materials Research Bulletin* **44**, 284 (2009).
- [44] D. Lin, K. W. Kwok, H. L. W. Chan, *Journal of Alloys and Compounds* **461**, 273 (2008).
- [45] Wördenweber R. (2011). *Ferroelectric Thin Layers, Comprehensive Semiconductor Science and Technology*. Amsterdam: Elsevier.
- [46] J. H. Haeni, P. Irvin, W. Chang, R. Uecker, P. Reiche, Y. L. Li, S. Choudhury, W. Tian, M. E. Hawley, B. Craigo, A. K. Tagantsev, X. Q. Pan, S. K. Streiffer, L. Q. Chen, S. W. Kirchoefer, J. Levy, and D. G. Schlom, *Nature* **430**, 758 (2004).
- [47] B. Cai, J. Schwarzkopf, E. Hollmann, M. Schmidbauer, M. O. Abdel-Hamed, R. Wördenweber, *Journal of Applied Physics* **115**, 224103 (2014).
- [48] B. Cai, J. Schwarzkopf, E. Hollmann, D. Braun, M. Schmidbauer, T. Grellmann, R. Wördenweber, *Physical Review B* **93**, 224107 (2016).
- [49] B. Cai, J. Schwarzkopf, C. Feldt, J. Sellmann, T. Matkurt, R. Wördenweber, *Physical Review B* **95**, 184108 (2017).
- [50] B. Cai, "Manipulation the Structural and Electronic Properties of Epitaxial  $\text{NaNbO}_3$  Films via Strain and Stoichiometry" Ph.D dissertation, D 38 (Diss., Köln, Univ., 2016).
- [51] G. A. Smolenskii, V. A. Isupov, *Zh. Tekh. Fiz.* **24**, 1375 (1954).
- [52] R. Wördenweber and Y. Dai, in '*Strontium Titanate: Synthesis, Properties and Uses*', New York: Nova Science Publishers, Inc., *Materials Science and Technologies* (2019) 101-155.
- [53] G. A. Smolenskii, V. A. Isupov, A. I. Agranovskaya, and S. N. Popov, *Sov. Phys. Solid State*, **2**, 2906 (1960).
- [54] L. E. Cross, *Ferroelectrics* **76**, 241 (1987).
- [55] L. E. Cross, *Ferroelectrics*, **151**, 305 (1994).
- [56] V. Bobnar, Z. Kutnjak, R. Pirc, R. Blinc, and A. Levstik, *Phys. Rev. Lett.* **84**, 5892 (2000).
- [57] A. E. Glazounov and A. K. Tagansev, *Ferroelectrics* **221**, 57 (1999).
- [58] V. Westphal, W. Kleemann, and M. D. Glinchuk, *Phys. Rev. Lett.* **68**, 847 (1992).
- [59] R. Fisch, *Phys. Rev. B* **67**, 094110 (2003).
- [60] L. Rayleigh, 1885. On waves propagated along the plane surface of an elastic solid. *P. Lond. Math. Soc.* **1**, 4–11.
- [61] Y. Q. Fu, J. K. Luo, N. T. Nguyen, A. J. Walton, A. J. Flewitt, X. T. Zu, Y. Li, G. McHale, A. Matthews, E. Iborra, H. Du, W. I. Milne, *Progress in Material Science* **89**, 31 (2017).

- [62] Zhang S. Y., Cheng L. P. (2010). *Surface Acoustic wave Motors and Actuators: Mechanism, Structure, Characteristic and Application*. In: Dissanayake D. W. (editor). *Acoustic Waves*. Croatia: Sciyo.
- [63] K. Sezawa, K. Kanai, Bull. Earthq. Res. Inst. **3**, 13 (1927).
- [64] G. S. Chung, D. T. Phan, Journal of the Korean Physical Society **57**, 446 (2010).
- [65] M. Z. Aslam, V. Jeoti, S. Karuppanan, A. F. Malik, A. Iqbal, Sensors **18**, 1687 (2018).
- [66] Maugin G.A. (1988) *Shear Horizontal Surface Acoustic Waves on Solids*. In: Parker D.F., Maugin G.A. (eds) *Recent Developments in Surface Acoustic Waves*. Springer Series on Wave Phenomena, vol 7. Berlin, Heidelberg: Springer.
- [67] F. Josse, F. Bender, R. W. Gernosek, Anal. Chem. **73**, 5937 (2001).
- [68] R. M. White, F. W. Voltmer, Applied Physics Letters **7**, 314 (1965).
- [69] W. Soluch, S. Member, M. Lusakowska, IEEE Transactions on Ultrasonics, Ferroelectrics, and Frequency Control **52**, 145 (2005).
- [70] J. Devkota, P. R. Ohodnicki, D. W. Greve, Sensors **17**, 1 (2017)
- [71] N. Naumenko, IEEE Transactions on Ultrasonics, Ferroelectrics, and Frequency Control **48**, 530 (2001).
- [72] S. Y. Chu, T. Y. Chen, I. T. Tsai, W. Water, Sensors and Actuators A **113**, 198 (2004).
- [73] R. C. Chang, S. Y. Chu, Y. P. Wong, Y. F. Lin, C. S. Hong, Sensors and Actuators A **136**, 267 (2007).
- [74] Morgan D. (2007). *Surface Acoustic Wave Filters*. Oxford: Elsevier.
- [75] C. K. Campbell, IEEE Ultrasonic Symposium **23**, 169 (1998).
- [76] H. Egan, IEEE Transactions on Ultrasonics, Ferroelectrics, and Frequency Control **ED-16**, 1014 (1969).
- [77] M. Perry, I. Mckeeman, M. Saafi, P. Niewczas, Smart Materials and Structures **25**, 035035 (2016).
- [78] C. K. Ho, E. R. Lindgren, K. S. Rawlinson, Lucas K. McGrath, J. L. Wright, Sensors **3**, 236 (2003).
- [79] E. T. Zellers, N. Hassold, R. M. White, S. M. Rappaport, Anal. Chem. **62**, 1227 (1990).
- [80] T. T. Wu, Y. Y. Chen, T. H. Chou, J. Phys. D: Appl. Phys. **41**, 085101 (2008).
- [81] A. Afzal, N. Iqbal, A. Mujahid, R. Schirhagl, Analytica Chimica Acta **787**, 36(2013).
- [82] X. Chen, D. Liu, Materials Science and Engineering C **30**, 1175 (2010).

- [83] A. J. Ricco, S. J. Martin, T. E. Zipperin, *Sensors and Actuators* **8**, 319 (1985).
- [84] K. Länge, B. E. Rapp, *Anal Bioanal Chem* **391**, 1509 (2008).
- [85] O. Onen, A. Sisman, N. D. Gallant, P. Kruk, R. Guldiken, *Sensors* **12**, 7423 (2012).
- [86] E. R. Gray, V. Turbe, V. E. Lawson, R. H. Page, Z. C. Cook, R. B. Ferns, E. Nastouli, D. Pillay, H. Yatsuda, D. Athey, D. Athey, R. A. Mckendry, *Digital Medicine* **23**, 1 (2018).
- [87] S. Lee, K. B. Kim, Y. Kim, *Food Sci. Biotechnol.* **20**, 1413 (2011).
- [88] G. Sauerbrey, *Zeitschrift* **155**, 206 (1959).
- [89] B. Noheda, D. E. Cox, *Phase Transitions* **79**, 5 (2006).
- [90] H. X. Fu, R. E. Cohen, *Nature* **403**, 281(2000).
- [91] R. Guo, L. E. Cross, S. E. Park, B. Noheda, D. E. Cox, G. Shirane, *Physical Review Letters* **84**, 5423 (2000).
- [92] European Union, "Directive 2002/95/EC of the European Parliament and of the Council of 27 January 2003 on the restriction of the use of certain hazardous substance in electrical and electronic equipment," *Off. J. Eur. Union* **L37**, 19 (2003).
- [93] D. G. Schlom, L. Q. Chen, C. B. Eom, K. M. Rabe, S. K. Streier, J. M. Triscone, *Annual Review of Material Research* **37**, 589 (2007).
- [94] A. Vailionis, H. Boschker, W. Siemons, E.P. Houwman, D. H. A. Blank, G. Rijnders, G. Koster, *Phys. Rev. B* **83**, 064101 (2011).
- [95] K. Wang, J. F. Li, *Applied Physics Letters* **91**, 262902(2007).
- [96] C. N. W. Darlington, H. D. Megaw, *Acta Crystallographica Section B Structural Crystallography and Crystal Chemistry* **29**, 2171(1973).
- [97] *J. Sellmann, Impact of strain and composition on structural and piezo-/ferroelectric properties of epitaxial NaNbO<sub>3</sub> and K<sub>x</sub>Na<sub>1-x</sub>NbO<sub>3</sub> thin films and superlattices grown by PLD, in Technische Universität Berlin. 2015, Technische Universität Berlin.*
- [98] A. Hewat, *Journal of Physics C: Solid State Physics* **6**, 1074 (1973).
- [99] L. Y. Liang, Y. L. Li, L. Q. Chen, S. Y. Hu, G. H. Lu, *Journal of Applied Physics* **106**, 104118 (2009).
- [100] L. Wu, J. L. Zhang, C. L. Wang, J. C. Li, *Journal of Applied Physics* **103**, 084116 (2008).
- [101] J. Koruza, H. Liu, M. Höfling, M. H. Zhang, P. Veber, *Journal of Materials Research* **35**, 990 (2020).
- [102] J. Schwarzkopf, D. Braun, M. Hanke, A. Kwasniewski, J. Sellmann, M. Schmidbauer, J. *Appl. Cryst.* **49**, 375 (2016).

- [103] A. Duk, "Relationships between strain, ferro- and piezoelectric properties in functional oxide thin films" Ph.D. dissertation, Humboldt University of Berlin, 2013.
- [104] A. Markov, K. Greben, D. Mayer, A. Offenhäusser, R. Wördenweber, *ACS Applied Materials and Interfaces* **8**, 16451 (2016).
- [105] Wikipedia contributors. Diffraction — Wikipedia, the free encyclopedia, 2019. [Online; accessed 25-April-2019].
- [106] M. Schmidbauer, P. Schäfer, S. Besedin, D. Grigoriev, R. Köhlerb and M. Hanke, *J. Synchrotron Rad.* **15**, 549 (2008).
- [107] O. G. Vendik, S. P. Zubko, and M. A. Nikol'skii, *Technical Physics* **44**, 349 (1999); O. G. Vendik, and M. A. Nikol'skii, *Technical Physics* **46**, 112 (2001).
- [108] S. S. Gevorgian, T. Martinsson, P. L. Linner, and E. L. Kollberg, *IEEE Trans. Microwave Theory Tech.* **44**, 896 (1996).
- [109] E. Chen and S. Y. Chou, *IEEE Trans. Microwave Theory Tech.* **45**, 939 (1997).
- [110] D. Finck, "Development of a Surface Acoustic Wave Sensor for In situ Detection of Molecules", Master thesis, D 38 (Master Köln, Univ., 2020).
- [111] S. Liang, Y. Dai, L. von Helden, J. Schwarzkopf, R. Wördenweber, *Appl. Phys. Lett.* **113**, 052901 (2018).
- [112] H. Vogel, *Phys. Z.* **22**, 645 (1921)
- [113] G. S. Fulcher, *J. Am. Ceram. Soc.* **8**, 339 (1925)
- [114] A. A. Bokov and Z.-G. Ye, *Solid State Commun.* **116**, 105 (2000).
- [115] C. C. Tseng, *IEEE Trans. Electron Devices* **ED-15**, 586 (1968).
- [116] R. M. White, *Proc. IEEE* **58**, 1238 (1970).
- [117] W. R. Smith, H. M. Gerard, J. H. Collins, T. M. Reeder, and H. J. Shaw, *IEEE Trans. Microwave Theory Tech.* **17**, 856 (1969).
- [118] Y. Sakshita and H. Segawa, *J. Appl. Phys.* **77**, 5995 (1995).
- [119] C. R. Gorla, N. W. Emanetoglu, S. Liang, W. E. Mayo, Y. Lu, M. Wraback, and H. Shen, *J. Appl. Phys.* **85**, 2595 (1999).
- [120] X. Y. Du, Y. Q. Fu, S. C. Tan, J. K. Luo, A. J. Flewitt, W. I. Milne, D. S. Lee, N. M. Park, J. Park, Y. J. Choi, S. H. Kim, and S. Maeng, *Appl. Phys. Lett.* **93**, 094105 (2008).
- [121] X. Y. Du, Y. Q. Fu, S. C. Tan, J. K. Luo, A. J. S. Maeng, S. H. Kim, Y. J. Choi, D. S. Lee, and N. M. Park, *J. Phys.: Conf. Ser.* **76**, 012035 (2007).

- [122] Y. Takagaki, P. V. Santos, E. Wiebicke, O. Brandt, H. P. Schönherr, and K. H. Ploog, *Appl. Phys. Lett.* **81**, 2538 (2002).
- [123] L. von Helden, M. Schmidbauer, S. Liang, M. Hanke, R. Wördenweber, J. Schwarzkopf, *Nanotechnology* **29**, 415704 (2018).
- [124] Q. J. Wang, C. Pflügl, W. F. Andress, D. Ham, F. Capasso, *J. Vac. Sci. Technol. B* **26**, 1848 (2008).
- [125] S. Liang, D. Pfützenreuter, D. Finck, L. von Helden, J. Schwarzkopf, R. Wördenweber, *Appl. Phys. Lett.* **116**, 052902 (2020).
- [126] M. Glass, "Molecular Layer Deposition and Protein Interface Patterning for Guided Cell Growth", Master thesis, D 38 (Master Köln, Univ., 2020).
- [127] C. Hirschle, J. Schreuer, S. Ganschow, I. Schulze-Jonack, *J. Appl. Phys.* **126**, 165103 (2019).

## Appendix

### Sample list

Table A-1: list of sample discussed in this dissertation.

Sample name	Film	Thickness [nm]	Substrate	Preparation method	Roughness Ra [nm]	Vertical lattice parameter [Å]	T <sub>c</sub> [K]	
							[110] <sub>sub</sub>	[001] <sub>sub</sub>
47_008_DSO	K <sub>0.7</sub> Na <sub>0.3</sub> NbO <sub>3</sub>	27	DyScO <sub>3</sub>	MOCVD	0.34	4.072	230	
47_008_TSO	K <sub>0.7</sub> Na <sub>0.3</sub> NbO <sub>3</sub>	27	TbScO <sub>3</sub>	MOCVD	0.68	4.057	330	324
47_008_GSO	K <sub>0.7</sub> Na <sub>0.3</sub> NbO <sub>3</sub>	27	GdScO <sub>3</sub>	MOCVD	0.24	4.044	409	380
47_008_SSO	K <sub>0.7</sub> Na <sub>0.3</sub> NbO <sub>3</sub>	31	SmScO <sub>3</sub>	MOCVD	0.35	4.017		
47_009_DSO	K <sub>0.7</sub> Na <sub>0.3</sub> NbO <sub>3</sub>	43	DyScO <sub>3</sub>	MOCVD	0.81	4.07	264	254
41_013_TSO	K <sub>0.7</sub> Na <sub>0.3</sub> NbO <sub>3</sub>	47	TbScO <sub>3</sub>	MOCVD				
47_016_DSO	K <sub>0.7</sub> Na <sub>0.3</sub> NbO <sub>3</sub>		DyScO <sub>3</sub>	MOCVD				
DP_1303	K <sub>0.7</sub> Na <sub>0.3</sub> NbO <sub>3</sub>	25	TbScO <sub>3</sub>	PLD			289	279
DP_1345	K <sub>0.7</sub> Na <sub>0.3</sub> NbO <sub>3</sub>			PLD				150

Sample name	Film	Thickness [nm]	Substrate	Preparation method	Roughness Ra [nm]	Vertical lattice parameter [Å]	T <sub>c</sub> [K]	
							[110] <sub>sub</sub>	[001] <sub>sub</sub>
DP_1353	K <sub>0.1</sub> Na <sub>0.9</sub> NbO <sub>3</sub>	30	PLD					
DP_1762	K <sub>0.7</sub> Na <sub>0.3</sub> NbO <sub>3</sub>	29	GdScO <sub>3</sub>	PLD	0.2	4.0512	248	239
DP_1757	K <sub>0.7</sub> Na <sub>0.3</sub> NbO <sub>3</sub>	30	TbScO <sub>3</sub>	PLD	0.2	4.0635	169	156
DP_1304	K <sub>0.7</sub> Na <sub>0.3</sub> NbO <sub>3</sub>		GdScO <sub>3</sub>	PLD				
DP_1305	K <sub>0.7</sub> Na <sub>0.3</sub> NbO <sub>3</sub>		GdScO <sub>3</sub>	PLD				
DP_1345	K <sub>0.7</sub> Na <sub>0.3</sub> NbO <sub>3</sub>	22	DyScO <sub>3</sub>	PLD		4.065		150
DP_1347	K <sub>0.9</sub> Na <sub>0.1</sub> NbO <sub>3</sub>	30	TbScO <sub>3</sub>	PLD				500

## E-beam lithography and lift-off recipe

The detailed E-beam lithography and lift-off recipe is described as follows:

1. **Cleaning:** To remove surface pollutions, the sample is rinsed successively in a solvent of acetone and isopropanol for 5 min in an ultrasonic bath (UB) (320 W, 37 kHz) at room temperature and then dried by nitrogen gun.
2. **PMMA Coating:** Photoresist, poly(methyl-methacrylate) (PMMA), is spin-coated onto the sample at 4000 r / min for 1 minute. PMMA 649.04 950K from company Allresist is used in this thesis.
3. **Baking:** After spin coating, the sample is baked on a hot plate at 140 °C for 30 minutes. Baking temperature and time are adjusted according to the quality of the structure and the thickness of the PMMA layer.
4. **Cr deposition:** A 10 nm thick Cr is deposited onto the PMMA layer via evaporation deposition to enable the surface conductivity of PMMA, which is essential for the electron-beam lithography.
5. **E-beam lithography:** The patterns of the structures were designed via AutoCAD, and then written into the electron-sensitive photoresist via e-beam (Vistec EBPG 5200, 100 keV, resolution > 10 nm, overlay  $0.5 \pm 2.5$  nm). The incident focused electron beam traverses the PMMA and cracks the major polymer chains of the PMMA. Therefore, the PMMA can be selectively removed at the exposed area afterward exposure using a developer solution.
6. **Cr etching:** Subsequently, the 10 nm thick Cr layer is removed by an etchant, typically a mixture of ceric ammonium nitrate  $((\text{NH}_4)_2[\text{Ce}(\text{NO}_3)_6])$ , perchloric acid ( $\text{HClO}_4$ ) and deionized water with a ratio of 10.9% : 4.25% : 84.85% (MicroChemicals). The Cr etching rate is 80 nm / min, which will not change the properties of the PMMA. Afterwards, the sample is rinsed in deionized water for 1 min and then dried using a nitrogen gun.
7. **Development:** The exposed PMMA is removed by a developing solvent (developer). The sample is rinsed in the developer AR-600-55 (Allresist) with the main component of methyl-isobutyl-ketone (MIBK) for 120 s. Then it is rinsed in isopropanol for 1 min to wash away the developer. Finally the sample is dried using a nitrogen gun.
8. **Plasma cleaning:** Before electrode deposition, the remnant PMMA is removed by  $\text{O}_2$  plasma to improve the quality (adhesion, morphology) of the deposited electrodes. The plasma cleaning is done with Gigabatch 310 for 5 min using parameters of 300 W and 200 sccm  $\text{O}_2$  flow.
9. **Electrodes deposition:** The metallic electrodes and components are deposited on the sample via evaporation techniques. First a 5 nm thick Ti layer is deposited in order to enhance the adhesion. Subsequently a 45 nm thick Pt layer is deposited onto the Ti layer.

10. **Lift-off:** The Ti/Pt layer on top of the PMMA is removed with the PMMA (lift-off), whereas the layer directly on top of the sample remains. For this purpose, the PMMA is dissolved in acetone, the metallic layer on top of the PMMA is removed at the same time. The sample is rinsed in acetone for 5 min, and the designed pattern appears. If PMMA remains on the sample, a 60 s ultrasonic bath treatment with moderated power can be applied to finalize the lift-off process. Subsequently the sample is rinsed in isopropanol for 1 min to remove the acetone. Afterwards, the sample is dried using the nitrogen gun.

## Acknowledgement

I would like to first thank my supervisor Prof. Dr. Roger Wördenweber. He is definitely the kind of supervisor that every PhD student dreams to work with. He guided me to the fascinating field of surface acoustic wave sensors and we had a lot of fun along the way. For all the problems I met during the study, he would discuss carefully with me with a lot of patience. I learnt a lot from him, not only academically, but also in life. He taught us to always see the positive part, and this concept helped a lot in the study as well as in the life, especially when I was experiencing lows and failures. The working experience with Roger would be a treasure for the rest of my life.

I would also like to thank Prof. Dr. Andreas Offenhäusser for providing us a harmonious international working environment. Many thanks to Rolf Kutzner for giving me the safety instructions and helping me solve technical problems. My sincere thanks to Dr. Stefan Trellenkamp and Dr. Florian Lentz for E-beam writing, without your help I can't achieve so many microelectrodes with beautiful structures. Thanks to Dr. Uwe Breuer in ZEA-3 of FZJ for perfect ToF-SIMS measurements.

I am very thankful to our collaborating group at IKZ, Berlin for providing perfect MOCVD and PLD samples. My sincere thanks to Dr. Jutta Schwarzkopf for your valuable suggestions and discussions. Thanks to Leonard von Helden for discussions and PFM measurements. I appreciate Daniel Pfützenreuter for preparation of PLD samples. The meetings with you guys are always interesting and fruitful. Thanks to Dr. Martin Schmidbauer for XRD measurements.

My special thanks to my lovely colleagues, we have the best working atmosphere in the world. Thanks to Yang Dai for helping me get used to the life in Jülich and a lot valuable guidance for my work (e.g. how to make a helium balloon). Thank you Xiaobo Yuan for sharing the office with me and I will not forget the experience that we rod in the midnight in the middle of nowhere for hours. Thank you Nikolaus Wolf for always bringing us joy. Thanks to Dennis Finck and Manuel Glass for showing me the most delicious Schnitzel in Köln.

I want to show the greatest appreciation to my family. My parents always give me unconditional supports, encouraging me to pursue whatever I think is right and don't leave regrets. My sincerest love to my girlfriend Xuan He, you means everything to me, we have been through a lot together along the way and I am sure there will be more in the future.

Last but not the least, I want to thank China Scholarship Council (CSC) for the final support during my whole PhD career, especially during the COVID-19 pandemic your care makes me warm.



Band / Volume 231

**Interface Functionalization of Magnetic Oxide Fe<sub>3</sub>O<sub>4</sub>/SrTiO<sub>3</sub>  
Heterostructures**

M. H. A. Hamed (2021), xvii, 151 pp

ISBN: 978-3-95806-535-2

Band / Volume 232

**Optically induced magnetization reversal in Co/Pt multilayers**

Role of domain wall dynamics

U. Parlak (2021), ix, 162, XII pp

ISBN: 978-3-95806-536-9

Band / Volume 233

**Application of Silicon Photomultipliers in Neutron Detectors**

S. Kumar (2021), xxvi, 157 pp

ISBN: 978-3-95806-537-6

Band / Volume 234

**Towards Magneto-Elastomeric Nanocomposites with Supramolecular  
Activity**

L. S. Fruhner (2021), XVI, 213 pp

ISBN: 978-3-95806-538-3

Band / Volume 235

**Geometric and Electronic Properties of Heteromolecular Organic  
Monolayers on Noble Metal Substrates Studied by Photoemission  
Spectroscopy and X-ray Standing Waves**

G. van Straaten (2021), vii, 115 pp

ISBN: 978-3-95806-539-0

Band / Volume 236

**Nanoparticle assemblies: Order by self-organization and collective  
magnetism**

A. Qdemat (2021), xix, 282 pp

ISBN: 978-3-95806-542-0

Band / Volume 237

**$\gamma$ -Aminobutyrate as carbon and nitrogen source for *Corynebacterium  
glutamicum* and regulation of the catabolic genes by GabR**

L. Zhu (2021), 111 pp

ISBN: 978-3-95806-543-7

Band / Volume 238

**Single-Trap Phenomena in Nanowire Biosensors**

Y. Kutovyi (2021), 171 pp

ISBN: 978-3-95806-544-4

Band / Volume 239

**Single crystal growth and neutron scattering studies of novel quantum materials**

X. Wang (2021), VI, 145 pp

ISBN: 978-3-95806-546-8

Band / Volume 240

**Structure and Dynamics of Magnetocaloric Materials**

N. A. Maraytta (2021), vii, 146 pp

ISBN: 978-3-95806-557-4

Band / Volume 241

**Novel insights into the transcriptional regulation of cell division in *Corynebacterium glutamicum***

K. J. Kraxner (2021), V, 83 pp

ISBN: 978-3-95806-560-4

Band / Volume 242

**Interplay of proximity effects in superconductor/ferromagnet heterostructures**

A. Stellhorn (2021), ix, 219 pp

ISBN: 978-3-95806-562-8

Band / Volume 243

**Silencing and counter-silencing of the Lsr2-like protein CgpS in *Corynebacterium glutamicum***

J. Wiechert (2021), IV, 265 pp

ISBN: 978-3-95806-569-7

Band / Volume 244

**Molecular Layer Functionalized Neuroelectronic Interfaces:**

From Sub-Nanometer Molecular Surface Functionalization to Improved Mechanical and Electronic Cell-Chip Coupling

N. R. Wolf (2021), IV, 101, xx pp

ISBN: 978-3-95806-570-3

Band / Volume 245

**Surface Acoustic Waves in Strain-Engineered Thin (K,Na)NbO<sub>3</sub> Films:**

From Basic Research to Application in Molecular Sensing

S. Liang (2021), VI, 125 pp

ISBN: 978-3-95806-571-0

Weitere **Schriften des Verlags im Forschungszentrum Jülich** unter  
<http://www.zb1.fz-juelich.de/verlagextern1/index.asp>



Schlüsseltechnologien / Key Technologies

Band / Volume 245

ISBN 978-3-95806-571-0

Mitglied der Helmholtz-Gemeinschaft

